MARCO BARBETTA

OPTICAL CHARACTERIZATION OF MULTILAYER COATING SAMPLES

TESI DI LAUREA

Relatore: Prof.sa Maria Guglielmina Pelizzo

Universitá degli Studi di Padova
Facoltá di Ingegneria
Dipartimento di Ingegneria dell'Informazione
Corso di Laurea in Ingegneria Elettronica
Settembre 2010

An idea that is not dangerous is unworthy
of being called an idea at all.

— Oscar Wilde

ABSTRACT

This paper aims to describe a measurement process studied and applied by the author at CNR IFN - LUXOR laboratories in Padova. The main purpose was to establish the reflectivity performance of some optical mirrors realized with different multilayer technologies. For such devices applications are foreseen in the *Metis* coronagraph for the ESA *Solar Orbiter* mission, and in the *Free Electron Laser* facility in Trieste.
After having studied the bands in which precise reflectance values were needed for the application, measures were took for each sample in the EUV, VIS and NIR range using the facilities available at LUXOR laboratories. The principle of operation of these devices, the structure of the facilities used and the measurement process are going to be described in this paper, then the results will be presented and discussed.
This work was inserted in a more wide sample characterization project which was developed by the LUXOR team. It included reflectance measurements in different spectra, such as Soft-X, and AFM surface analysis, whose data will be presented for completeness.
The aim of these measurements was not only to establish whether some of the samples satisfy the specifications imposed by their application or not, but also to understand which of the multilayer technologies used should possibly be improved and tested for the application. The results, finally, state a performance baseline for the samples, which are going to be exposed to the conditions of their applications (e.g. solar wind in space) in order to establish their performance loose with aging.

SOMMARIO

Questo scritto intende descrivere un processo di misura studiato ed applicato dall'autore ai laboratori LUXOR del CNR IFN. Lo scopo principale era di stabilire le prestazioni in riflettività di specchi ottici realizzati in differenti tecnologie multilayer, e progettati per l'utilizzo nel coronografo *Metis*, della missione ESA *Solar Orbiter*, e nella facility *Laser ad Elettroni Liberi* a Trieste.
Dopo aver studiato le bande nelle quali erano richiesti dall'applicazione precisi valori di riflettività, sono state effettuate misure per ogni campione nelle bande EUV, VIS e NIR utilizzando le facility a disposizione nei laboratori LUXOR. Saranno quindi presentati i principio di funzionamento dei dispositivi, quello delle facility utilizzate nonché il processo di misura, del quale saranno infine presentati e discussi i risultati.
Il lavoro era inserito in un più ampio progetto di caratterizzazione dei campioni, sviluppato dal team LUXOR. Includeva misure di riflettività in differenti bande spettrali, come i Soft-X, e analisi di superficie AFM, i cui dati saranno presentati per completezza.

Il fine di queste misure non era solo di stabilire se alcuni dei campioni soddisfacessero o meno le specifiche imposte dall'applicazione, ma anche di capire quale delle tecnologie usate dovesse eventualmente essere migliorata e testata per l'applicazione. I risultati, infine, stabiliscono una linea di base delle prestazioni dei campioni, che saranno esposti alle condizioni della loro applicazione (per.es. vento solare nello spazio) allo scopo di stabilire la loro perdita in prestazioni dovuta all'invecchiamento.

The most exciting phrase to hear in science,
the one that heralds new discoveries,
is not 'Eureka!' (I've found it!), but "That's funny..."

— Isaac Asimov

ACKNOWLEDGEMENTS

Special thanks are due to Prof. Maria Pelizzo, which competence, enthusiasm and passion gave to the author the needed knowledge, advice and inspiration to carry on the work with severity and precision, but also with implication and fascination. The guide and teaching by Ph. D. Paola Zuppella for the use of instrumentation and the measurement process were indispensable to achieve the scientific approach and rigor of which the author is really proud. Also the technical advice of Ph. D. Gianni Monaco and Ph. D. Michele Suman was indispensable to understand the working mechanism of devices and instrumentation. Thanks must also go to Dr. Alain J. Corso, whose collaboration and help, together with the possibility to access part of his work, were an honor for the author.

Padova, settembre 2010 Marco Barbetta

CONTENTS

LIST OF FIGURES

LIST OF TABLES

INTRODUCTION

METIS Space observation is probably one of the most diffused applications of precision mirrors. The main part of the characteristics they need to perform well are clearly intuitive: very low aberration, roughness and high reflectivity, in order not to destroy the few luminous information coming from stars and, generally, space matter.

UV space observation

When working with Extreme UltraViolet wavelengths, normal single-coating mirrors can't reach the reflectivity performance needed. Instead multilayer coated mirrors can perform much better, basically because optical rays are reflected multiple times, reducing the losses.

Multilayers

Unfortunately, multilayer mirrors have strong bandwidth limitations, and so must be specifically designed to work on the narrow bands of interest. Their band limitation can also be an advantage, because it brings a first stage of selection and filtering of the desired wavelengths. In fact, space observation often deals with precise spectral intervals or lines, that reveal the presence of specific phenomena.
For those reasons often astronomical imaging instruments have separated channels for the different spectral bands.
The recent research about multilayer optics pointed out that it is possible to design mirrors that are tuned for a precise wavelength, but perform well also in other bands of interest. The proposal of INAF (National Institute for Astrophysics) to use these *multiband multilayer mirrors* in space imaging instruments brings the possibility to perform multiple types of measurements with the same instrument, a big worth for applications where mass and volume of the instrument is a limitation.

FEL The spectral selectivity of multilayer mirrors can be exploited also for the making of bandpass filters, working at wavelengths where normal absorption filters don't work because of excessive losses. The application of these narrowband devices has been proposed to selectively split and transport a laser beam, originated from the FERMI@Elettra Free Electron Laser facility. In this case, multilayer optics are thought to be the best solution to design an efficient spectral filter for FEL radiation.

Filtering FEL radiation

1 (E)UV CORONA IMAGING WITH METIS

CONTENTS

The first application of the multilayer mirror samples analyzed in this document is multiband space observation. The operating conditions and the specifications that these devices must comply with can be explained looking at the kind of phenomena to observe and at the instrumentation designed for that.

1.1 CORONAL HYDROGEN AND HELIUM

Hydrogen and Helium are the two most diffused elements in the heliosphere. Helium, with his mass four times larger than Hydrogen, can cause an energy and mass flux in the heliosphere even greater than his abundance [FAG+01]. The distribution and the kinematics of these elements in the different zones of the sun is fundamental for the investigation of the processes happening on the star of our system.

H and He investigation

The presence of Hydrogen and ionized Helium can be detected through their absorbance on the Lyman-α line, which corresponds to the wavelength emitted or absorbed when an electron jumps between the m=2→n=1 orbital energy levels. These lines are:

$$\begin{aligned} H^{0*} &\rightarrow H^{0} &:&\quad \text{HI line } \lambda^{\alpha} = 121.6\text{nm (UV)} \\ He^{+*} &\rightarrow He^{+} &:&\quad \text{HeII line } \lambda^{\alpha} = 30.4\text{nm (EUV)} \end{aligned}$$

RYDBERG FORMULA These values can easily be derived from the Rydberg formula [BJ03]:

$$\frac{hc}{\lambda} = \frac{Z^2 m_e e^4}{8\epsilon_0^2 h^2}\left(\frac{1}{n^2} - \frac{1}{m^2}\right) \tag{1.1}$$

calculating the constant part and adapting the units, it becomes:

$$\lambda^{\alpha}_{[nm]} = \frac{1243}{Z^2\left(1-\frac{1}{4}\right)\cdot 13.6\text{ eV}} = \frac{1243}{Z^2 \cdot 10.2\text{ eV}} \tag{1.2}$$

Known data

In particular the distribution of Helium is nowadays a challenging aspect of the discovery of the sun. At the distance of 1 A.U., an abundance of Helium of 4% has ben measured on solar winds. Also the abundance on the photosphere is well-known to be around 10%.

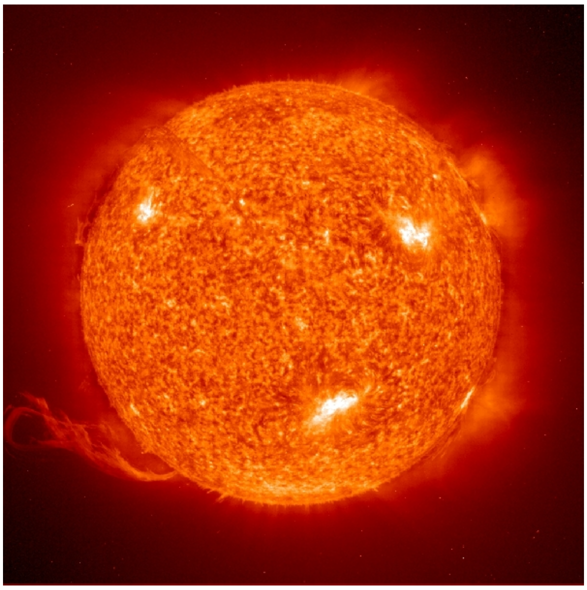

Figure 1: SOHO-EIT image of the sun @ 30.4nm (source: NASA).

Distribution hypothesis

Less information is available about the intermediate distances, such as the lower corona, and the extended corona, and actually for the latter no observation data is available. The prevision of many theoretical models [FAG+01] is that, instead of slowly decrease in percentage with distance in order to match the two abundance measurements, the presence of Helium could strongly increase near the extended corona ($1.1R_\odot$) up to values of 20 or even 150%, even more than Hydrogen.

This hypothesis is as strong as interesting for astronomy, and has to be proven with observations. The only measurements performed until now come from CHASE on board of NASA *Spacelab2* mission, which yelded values of 87.9% @ $1.15R_\odot$; and 8.9% $1.5R_\odot$ from SUMER on board of *SOHO*. These results were affected by a large uncertainty due to stray-light, collisional components and other interfering lines.
There partial results led to the project of an instrument specifically designed for extended corona observation ($R>1.2R_\odot$): the Multi Element Telescope for Imaging and Spectroscopy (Metis).

1.2 METIS ON THE SOLAR ORBITER

SOLO mission

Metis UVC will be part of the payload of the ESA *Solar Orbiter* (SOLO) mission, which is planned for launch on January 2017. Its travel around the Sun will last about 7.5 years and will bring it as down as 0.23 A.U. from the star center, with increasing inclination up to more than 30° with respect to the solar equator, being able to view the solar atmosphere with high spatial resolution, covering the poles and the side not visible from earth.

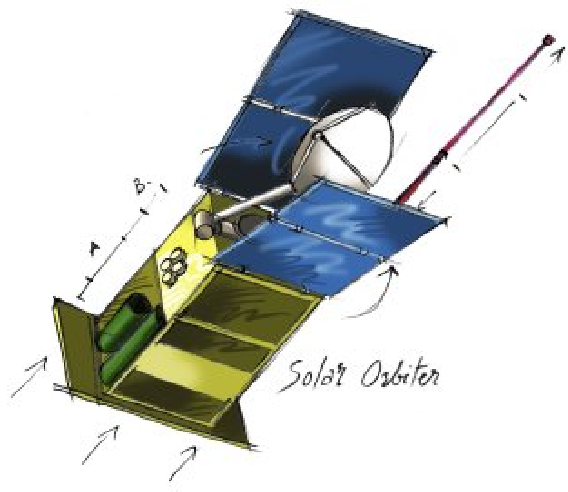

Figure 2: SOLO structure drawing (source: [Abt06]).

The main goal of the SOLO mission is to explore the Sun-Heliosphere connection, investigating the properties of the higher zones of the corona and in the near-Sun Heliosphere. The principal aspect of the investigation will be the properties, dynamics and interaction of plasma, fields and particles, mapping even the highest latitudes and the fine distribution of atmospheric magnetic fields.
That will yield a lot of data about the links between the solar surface, corona and inner heliosphere phenomena.

The SOLO payload [Ren07] can be grouped into four packages:

- **Solar Wind Plasma**: solar wind plasmas and electrons measurements;
- **Fields**: electromagnetic fields measurements;
- **Particles**: energetic particles, neutrons, γ-rays, and dust measurements;
- **Remote-Sensing**: Solar images and Doppler velocity and magnetic field; solar disk and corona images; spectroscopy, plasma diagnostics; imaging of acceleration sites, solar flare timing; coronal imaging and diagnostics. This package will carry the **Metis UVC**.

Metis in SOLO payload

1.3 METIS INSTRUMENT DESIGN

Metis is a externally occulted coronagraph designed for working in the VIS 500-650nm band and in the HI and HeII lines [ZGP+06]. The

Multiband coronagraph

occultation is a fundamental concept for a coronagraph and consists of a screen designed to reject the light coming from the solar disk, in order to avoid the saturation of the detectors and the presence of unwanted stray light inside the optical channel.
The instrument design [NAA+10] consists of an *inverted coronagraph* (ICOR), that is an inverted external-occulted coronagraph, implemented as an on-axis Gregorian telescope.

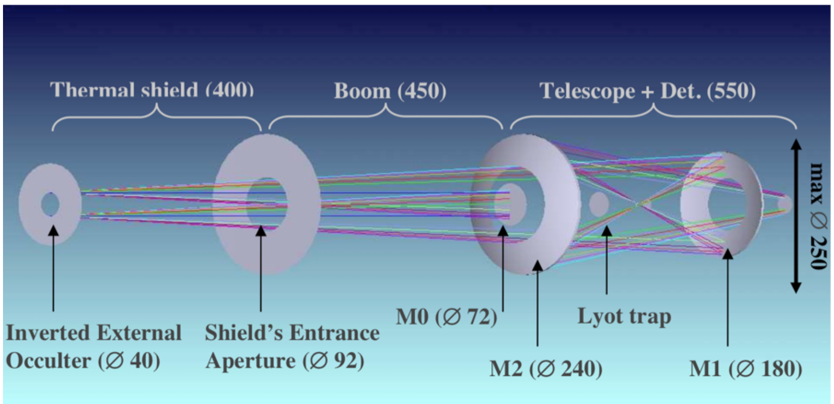

Figure 3: METIS optical design.

EXTERNAL INVERTED OCCULTER (IEO) As the function suggests, a normal external occulter is a circular screen which, inserted at the right distance from the input of the optical channel, is able to shadow the image of the solar disk. Combined with the circular aperture at the input of the instrument (*thermal shield*), the overall structure is a ring, if the occulter is at the same distance of the shield. An inverted occulter is constituted of a simple pupil entrance on the shield. In this way, at the input of the optical channel, a ring-shaped region is illuminated only by the light coming from the corona, because the incoming rays cross at the pupil. With this occulter, only a telescope with a ring-shaped input channel can correctly work, but has the advantage of reducing the aperture size and therefore the thermal effect on the optical components.

Reducing aperture with IEO

ON-AXIS GREGORIAN TELESCOPE This telescope design consists of two concave mirrors, one of which has a ring shape. The light is firstly reflected by the main ring-shaped mirror, and then by the minor mirror that conveys the beam through the center of the main mirror, towards the detector. This implementation is really compact and avoids aberration problems that could came from an off-axis setup.

Overall design of Metis

The design, as shown in figure 3, consists firstly of the *occulting system*, made up by the IEO, the Shield Entrance Aperture (an aperture on the spacecraft body), the rejection mirror `M0` and the Lyot trap (these last two components are used to suppress the light diffracted by the

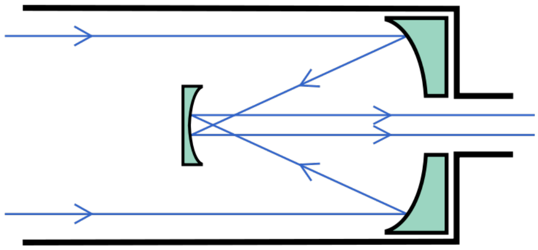

Figure 4: Gregorian telescope lightpath (source: WIKI).

apertures). The main component is the *telescope*, which is made up by mirrors `M1` and `M2`, and has a Gregorian structure except for the fact that both mirrors are ring-shaped. The last components are the *detectors*, placed after the mirror `M1` in a complex configurable setup that allows to have different *optical channels* for various measurement types.

1.4 METIS MIRRORS

Mirrors `M1` and `M2` must grant high reflectivity and low diffusion on the multiple lines and bands of interest, with optimization for the EUV HeII line, thus allowing multiband observations with the same instrument [ZGP+06] (possibly, they should also reject unwanted wavelengths). This is the problem focused by this work: the analysis of different multilayer technologies to make this mirrors maximizing efficiency and filtering. For imaging applications like this, nearly-normal incidence angles must be used, because the aberration would dramatically increase at high incidence angles, reducing available resolution.

Multilayer mirrors for Metis

Finally, it is also important to investigate the long-term stability of the measured characteristics, in order to grant the compliance of the devices trough all (and possibly over) the 7.5 years of the space mission, during which they will be exposed not only to normal aging, but also to solar wind particles and thermal stresses.

1.5 INSTRUMENT CHANNELS

The different observation bands are analyzed by dedicated channels: three imaging channels are available on Metis, plus a spectroscopic channel. Their configuration is made at the output of the telescope assembly, in the detector side.

UV+VIS CHANNELS When a multilayer Al/MgF_2 filter with 45° of incidence is placed after `M1`, these two channels are simultaneously active. UV HI line (121.6nm) is transmitted, whereas VIS light is reflected. UV is directed towards a photomultiplier followed by a CMOS Active Pixel

UV+VIS polarized imaging

Figure 5: 3D representation of Metis telescope mirrors.

Sensor (APS), and VIS light goes through a liquid crystal polarimeter, allowing to select the desired polarization for imaging, and is then captured by another APS sensor.

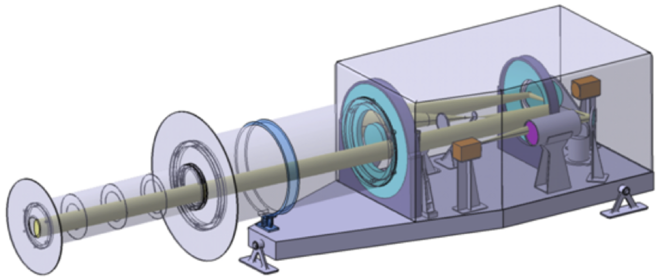

Figure 6: METIS VIS channel lightpath. The UV channel (not shown) is right trough the mirror filter.

EUV CHANNEL When a servo-mechanism exchanges the UV filter with an Aluminium filter, only EUV He II line (30.4nm) is allowed towards the UV detector, disabling the VIS channel.

CMOS sensor used as spectroscope

SPECTROSCOPIC CHANNEL Part of the UV CMOS sensor is not used for coronal imaging, it is instead dedicated to implement the last component of the Spectroscopic channel. A spherical reflective diffraction grating designed to work on both UV and EUV lines replaces a sector of the `M2` mirror and is illuminated by mirror `M1`. The diffraction pattern is selected by a multi-slit and then projected onto the dedicated part of the UV sensor.

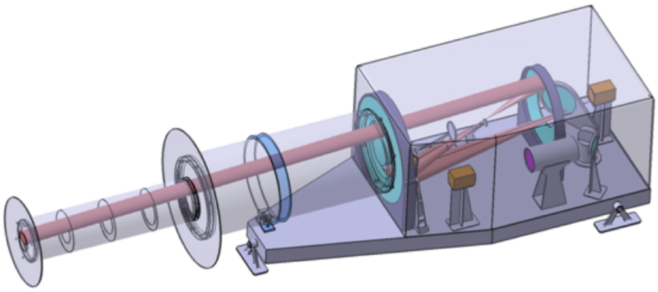

Figure 7: METIS EUV channel lightpath.

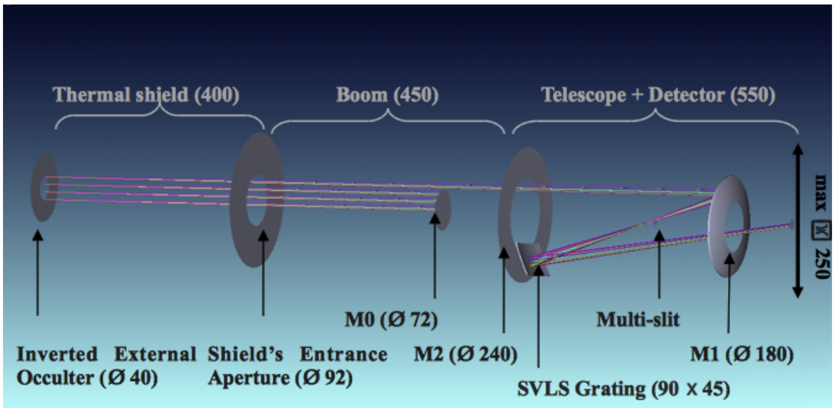

Figure 8: METIS Spectroscopic channel layout and lightpath.

2 FERMI FEL BEAM TRANSPORT

CONTENTS

The *Free Electron Laser* (FEL) is a laser light source that uses the emission of accelerated electrons, rather than spontaneous or stimulated emission from energy transitions of atoms or molecules. This makes the FEL a *free electron* device. It is one of the most coherent radiation sources available. Many other free electron devices are used nowadays in scientific, military and consumer applications; among then we can find Klystron, Magnetron and Travelling Wave Tube.

Free electron devices

The high peak intensity and particular shape of a FEL pulse must be considered when a transport system is designed. This makes multilayer coatings the most effective solution for such applications.

2.1 WORKING PRINCIPLE

It is well known that a charge emits radiation when accelerated (*free electron emission*). So a device being able to accelerate linearly (like Klystrons) or circularly (like Synchrotrons) an electron beam can produce light thanks to their emission. A device able to produce light emission with this principle and to resonate inside with amplification will emit a laser radiation.

LIGHT AMPLIFICATION Klystron tubes are non-relativistic free electron devices. A linearly accelerated electron beam is directed into a *buncher* cavity irradiated with an EM wave. The effect of the interaction between the particles and the wave is to produce a sinusoidal acceleration, with a consequent local periodic charge density modulation. This happens in a drift region, in which the charge flow modulation produces an EM wave, much stronger than the one that excited the process. When the beam reaches the *catcher* cavity, the EM wave is taken out thanks to a wave guide.
If this amplified wave, at the same frequency of the exciting one, is partially redirected to the first cavity, the device will oscillate on its own without the stimulus.

The main limitation [Gi002] of these free electron devices is the fact

Limitation of FE devices

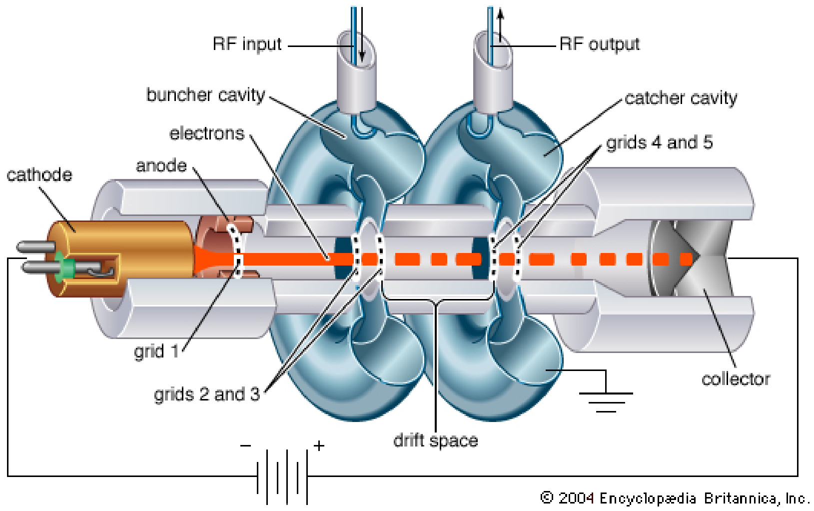

Figure 9: Klystron tube structure (source: Enciclopedia Britannica).

that the mechanical dimensions of the cavities must be of the same order of the emitted radiation wavelength, and so the most energetic radiation achievable is in the millimetric band, like *microwaves*.

Relativistic effects compress wavefronts

RELATIVISTIC EMISSION To overcome this limitation, it is necessary to accelerate the incoming electron beam up to relativistic speeds $v_e \approx c$. In these conditions, the electron emission is subject to the Lorentz transformations, and the wavefronts suffer of the *relativistic Doppler effect*. The emission, that is normally spherical centered on the particle, becomes a conical lobe θ pointing on the motion direction of the electron:

$$\theta \approx \frac{m_e c^2}{E} = \frac{1}{\gamma} \tag{2.1}$$

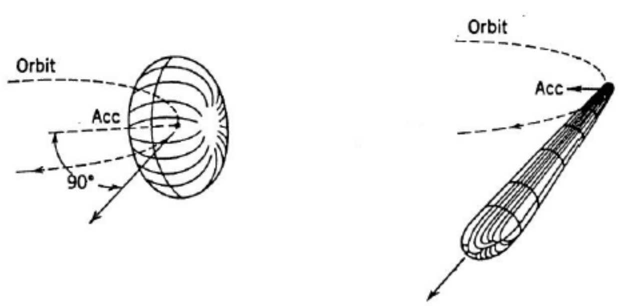

Figure 10: Comparison between the low speed accelerated electron emission (left) and the relativistic one (right).

Moreover, the wavefronts are compressed and the wavelength is shorter, thanks to the Lorentz time transformation:

$$\omega_l = \frac{\omega_e}{\sqrt{1-\beta^2}} \qquad \beta = \frac{v_e}{c} \tag{2.2}$$

and the Doppler effect:

$$\omega_o = \omega_l \frac{\sqrt{1+\beta}}{\sqrt{1-\beta}} \tag{2.3}$$

This effect, usually present in Synchrotron light sources, allows to free device dimensions from emitted radiation.

Overcome FE device limitation

A FEL is made up by the following components [Gi002]:

- **electron source**: a source to produce a relativistic electron beam to inject in the device;
- **undulator**: a periodic disposition of magnets (*Motz scheme*) to produce a sinusoidal magnetic field;
- **resonator**: a couple of mirrors aligned with the undulator axis, one of which is semi-reflective.

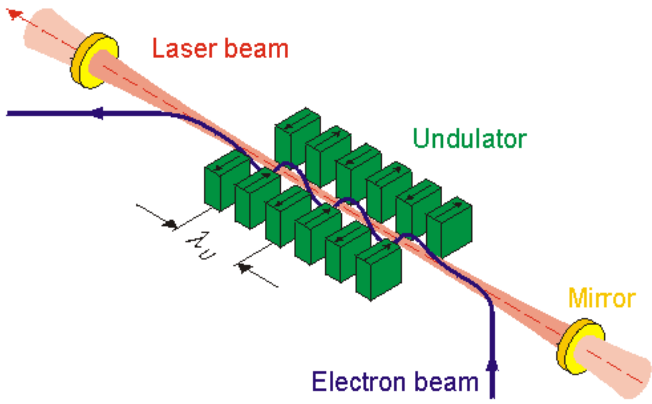

Figure 11: FEL structure (source: [Tec10]).

Let the period of the undulator magnetic field be λ_u, much longer than the desired emission wavelength. When a relativistic electron beam is injected in the undulator, the electrons will be accelerated by the field and will run through a sinusoidal path until they are dumped from the device. If the deviation from the undulator axis is less than the emission lobe angle θ, a coherent radiation along that axis will be emitted by the electrons in the rest frame:

Electron emission in rest frame

$$\omega_e = \frac{2\pi}{\lambda_u} c \tag{2.4}$$

This emission, for the relativistic effect previously described, propagates in the device reference frame with a frequency $\omega_o \gg \omega_e$ for

(2.2) and (2.3).
It could also be proven that, in presence of an EM wave, the behaviour of the electron beam inside the undulator is to amplify that wave, with a gain that depends on the beam current and on the parameters of the undulator. The resonator is then able to feed back the device with part of the emitted radiation, becoming a Laser oscillator.

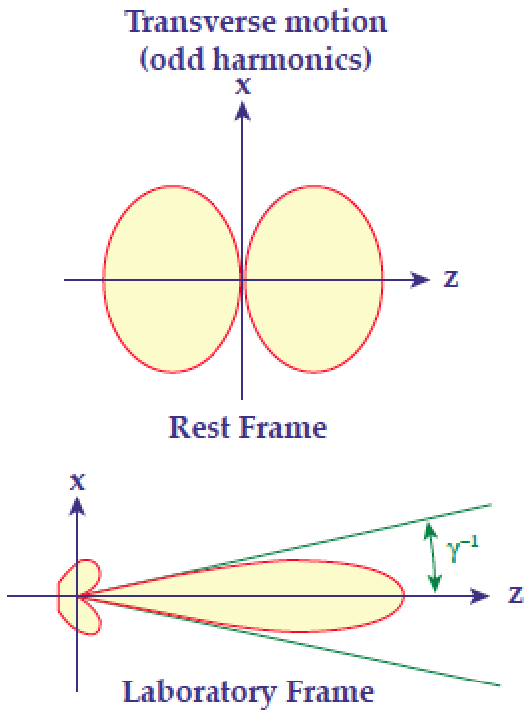

Figure 12: FEL emission due to the trasversal motion of electrons. It could be shown that it contains most only odd harmonics (source: [WBHH81]).

FEL equation

The wavelength emitted by the undulator is linked to the operative parameters in the formula [Att99]:

$$\lambda_o = \frac{\lambda_u}{2\gamma^2}\left(1 + \frac{K^2}{2} + \gamma^2\theta^2\right) \qquad \gamma = \frac{1}{\sqrt{1-\beta^2}} \tag{2.5}$$

where K is the undulator parameter and depends on λ_u and on the magnetic field intensity B.

New generation Synchrotron light source

The FEL is considered as a new generation Synchrotron light source [DR01]. In fact it has similar tunability over a wide spectrum, but the main features are that it can provide ultrashort, brilliant, highly-coherent, narrowband polarized pulses. In fact normal bending magnet Synchrotron radiation has a fairly plane spectrum, but low energy per unit frequency. This energy is strongly bigger in FEL radiation, because it contains only the fundamental for which the undulator is designed, and the odd harmonics, caused by the modes of resonance of the EM field into the amplifier.

2.2 FERMI FEL

Brief history

FEL was invented and implemented for the first time at Stanford university in 1977. Nowadays many FELs are available at facilities worldwide, and one the current challenges is to obtain the shortest wavelength lasing.
A *Storage Ring FEL* was implemented at Elettra facility in Trieste [Sin01] and in 2001 it reached the shortest wavelength lasing (190nm) ever obtained with a FEL until then. That implementation consisted on the insertion of the undulator into the Synchrotron ring, so that the accelerated electron beam passing through it seeded the laser.

The FERMI@Elettra project is expected to deliver the first light in the current year. It is realized with an *High Gain Harmonic Generation* (HGHG) scheme [Mil08], which is a chain of single-pass undulators (i.e. without resonator mirrors) seeded by a conventional laser source, and compared to other technologies, will deliver a more bright and fully temporally coherent radiation. The seed laser wavelength will be up-shifted by the undulators thanks to the interaction between EM wave and electron beam into magnetic field previously described; and the characteristics of the seed radiation will determine duration, bandwidth and wavelength of the output pulse, making it widely tunable.

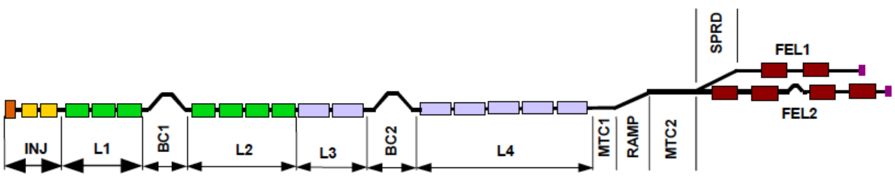

Figure 13: FERMI FEL structure (source: [BBC+10]).

FERMI FEL structure

Actually, two FELs are going to be built, one delivering radiation in 100-40nm (EUV) range and the other in the shorter 40-10nm Soft-X (SXR) range. The two lasers are fed by an electron beam provided by a *linear accelerator* (LINAC) , already present at Elettra and improved for the application. The system, displayed in figure 13 can be divided in the following components [BBC+10]:

Feeding system

INJECTOR A Ti:sapphire photocathode laser together with a photocathode RF gun injects UV laser light and SHF radiofrequency in a 100MeV LINAC, when another 10MW laser pulse increase the beam energy. 13 (INJ)

LINAC 14 linear accelerator sections, partially obtained from the existing Elettra structure, increase the electron beam energy up to 1.2GeV with up to 800A current. *Magnetic chicanes* between the sections compress the beam length up to an 11 factor. A beam spreader delivers the exiting beam to both FELs. 13 (L1, BC1, L2, L3, BC2, L4, SPRD)

Laser undulators

FEL1 The electron beam enters a first undulator (*modulator*) together with a high power seed laser, at a wavelength about 5 times the desired output λ_0. The interaction modulates the energy of the electron bunch. A second *dispersive section* converts the energy modulation into spatial charge distribution (*microbunching*) like in a Klystron tube, with many odd harmonics of the $5\lambda_0$ input. The last undulator (*radiator*) is the main FEL component, and as described before, makes the electron beam to radiate at the desired λ_0, selecting mainly this desired harmonic. This laser is designed to produce a 100-40nm tunable pulse with a 100-800ps duration and a 2+GW power. 13 (FEL1)

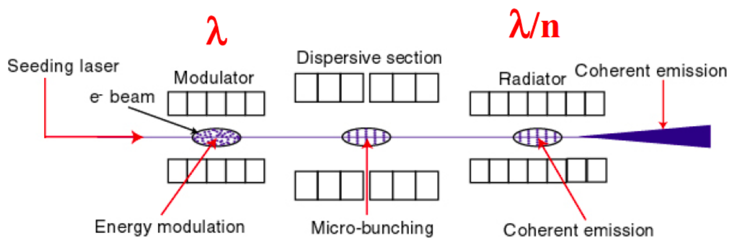

Figure 14: HGHG FEL structure (source: [BBC+10]).

FEL2 The second FEL is a two-stage device whose second stage modulator uses radiation from the first stage radiator, and so lets to reach shorter wavelengths of 40-10nm, but with half the power of FEL1. The use of particular radiator undulators (*APPLE II*) delivers a full polarization control over the emitted beam. 13 (FEL2).

An important characteristic of FERMI FEL is the highly gaussian shape of the pulses.

Beam dump and delivery

The beam is finally dumped and delivered to the transport system.

2.3 PHOTON TRANSPORT SYSTEM

The *photon transport system* delivers the laser beam to the experimental facilities, measuring the beam in many of its stages. The two laser outputs are aligned at the distace of 1m. The elements that compose the system are [CAB+09]:

Spatial filtering and attenuation

- *Shutters and aperture*: a safety shutter is the first element of the system. It will be able to absorb the very high peak power preserving the vacuum valves. It is followed by a beam-defining aperture, used to spatially filter the output beam.

- *Gas attenuator*: Passing through a gas-filled chamber, the pulse magnitude can be attenuated up to 4 times.

- *Intensity monitors*: Before and after the attenuator, photo-ionization intensity monitors are placed to tune the laser power, the attenuation and correct experimental data.

- *Switching and recombining mirror*: A three-mirror assembly allows to select the needed FEL output, the rest of the chain is now symmetrically repeated.

Beam selection

- *On line spectrometer*: A grating followed by a CCD sensor will acquire the full spectral density profile for each laser shot for the same purposes of the intensity monitors.

- *Wavelenght selectors*: Some of the experiments to be performed on beamlines need wavelengths shorter than 4nm. Due to limitations imposed by the undulator geometry (i.e. λ_u), the gain of the system drops when attempting to obtain a fundamental radiation below $\approx$ 4nm. For this reason shorter wavelengths will be obtained as third harmonic of the FEL2 emission, using wavelength selectors based on grating monochromators or multilayer technology.

Spectral filtering and pulse delaying

- *Delay lines*: In order to perform *pump and probe* experiments, some setup need wavelength-selective delay lines capable to impose a delay only to the third harmonic and leave the fundamental unchanged.

- *Beamlines*: Until now, three beamlines have been approved to perform experiments in the EUV and X range: DIPROI, dedicated to diffraction and projection imaging, LDM, dedicated to the study of the diluted system, and EIS, dedicated to elastic and inelastic scattering.

Experiment beamlines

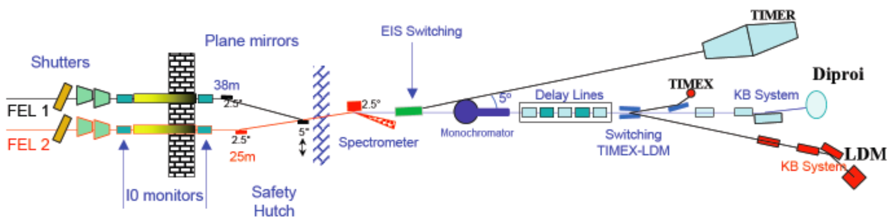

Figure 15: FERMI photon transport system structure (source: [CAB+09]).

PUMP AND PROBE A *pump and probe* experiment is a modern way to investigate the energetic states of matter. The procedure consists in exciting a material with a strong ultrafast pulse on a desired wavelength, and use a second wavelength to probe the changes induced in the matter, few femto or pico-seconds later. Usually the measures performed through the second pulse involve reflectivity, absorption, luminescence or scattering. Expressing the change in characteristics

Resonant mode analysis

measured as function of pump-probe delay time, makes possible to know (trough Fourier analysis) the resonant modes of the material [Uni10].

One of the most used setups is to use the first harmonic of an ultrafast laser to pump and the third delayed harmonic to probe. Up to now, such type of measure is performed for example at Deutsches Elektronen-Synchrotron DESY [Deu10].

2.4 MULTILAYER OPTICS PROJECT

Multilayer mirrors can be optimized to have the maximum efficiency at their design wavelength, while having minimum efficiency at its third harmonic, as will be clear from the following chapter.

Fundamental suppression to use 3rd harmonic

WAVELENGTH SELECTOR When using 1st harmonic FEL radiation in experiments, the laser pulse can be delivered as-is to the beamlines. In fact emission at 3rd and other odd harmonics has power levels approaching about 0.1-0.5% that of the fundamental. Instead, when 3rd harmonic is needed for measures, the wavelength selector must filter the beam spectrum suppressing the fundamental in order to have the main part of the power on the 3rd harmonic. Using diffraction gratings to build an EUV or SXR monochromator would result in a strong wavefront deformation, unless complex time-compensated setups are used. More effectively, the wavelength selector can be implemented with a multilayer mirror designed to reflect efficiently only the desired harmonic. For example, two cascaded Co/C multilayer mirrors optimized for 3rd-6.66nm can reach an attenuation factor on the 20nm fundamental of over $3{\cdot}10^3$ [ACC+10].

Selective delay line

DELAY LINE Pump and probe pulses can be obtained thanks to a delay line. The idea is to use a wavelength selector to filter the 1st and 3rd harmonic of the laser pulse and impose the desired delay to the 3rd, used for probing. Such a device has been proposed for implementation in DESY facility [FMS+03], and has been implemented with a beamsplitter which created two different beam paths with variable length, then filtered and recombined, as described in figure 16.

Such a system is designed to work with 150nm fundamental, and for the following reasons would have low efficiency at shorter wavelengths:

- for geometrical reasons, grazing incidence optics does not permit to achieve long optical path differences (OPD) between the two arms, so normal incidence optics must be used;
- the design uses thin film filters to select the harmonic (Al, Si, Zr, Nb) than won't work due to absorption problems at shorter wavelengths.

Beam filters based on monochromators have also been proposed, but the use of multilayer coating optics would make the system work with

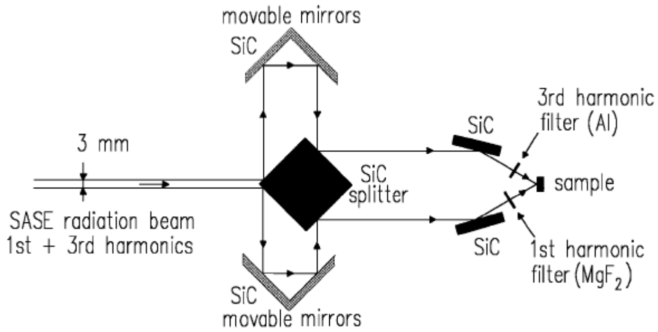

Figure 16: DESY pump-probe delay line schematic setup (source: [FMS+03]).

good efficiency also at shorter wavelengths, e.g. 30÷7nm. In fact the two arms of the device could be implemented with a cascade of two of four mirrors optimized for the respective harmonic, and will suppress the other without the need for a transmission filter.

Suppressive delay line with multilayers

FLATNESS TOLERANCE An important issue for the optical mirrors to be used is the mirror flatness [CAB+09]. In fact the strongly plane wavefronts of FEL pulse must not be altered by the cascaded mirrors in the transport lines. Having the beam reflected on the mirror, the phase perturbation φ on the wavefront depends on the Peak-to-Valley (PV) error of the surface δh according to the formula:

Phase perturbation equation

$$\varphi = \frac{2\delta h \sin\theta}{\lambda} \tag{2.6}$$

To evaluate the requirements for the mirrors we can impose a maximum phase perturbation of $\varphi = 0.1$ at an angle of incidence of $\theta = \frac{\pi}{4}$. The following table summarizes the evaluation for different wavelengths:

$\lambda[nm]$	max. $\delta h[nm]$
30.0	2.1
20.0	1.4
16.0	1.1
13.0	0.92
7.0	0.49

Table 1: Requirements to ensure wavefront preservation.

A project for the research and development upon the application of multilayer optics with FEL radiation sources has been conceived by the collaboration of LUXOR laboratories with FERMI@Elettra team in Trieste. The development at LUXOR laboratories is included in the ADvanced Optics for next generation RAdiation sources (ADORA) project funded by CARIPARO (Cassa di Risparmio di Padova e Rovigo) excellence grants.

LUXOR project for FEL multilayers

The experimental analysis of the first developed samples is presented in this work.

3 MULTILAYER SAMPLES

CONTENTS

Multilayer coating optics is born to overcome the typical limitations of optical components in EUV and SXR range. The analysis of their working principle and the knowledge of the materials available for that technology can lead to an optimization and performance evaluation.

3.1 UV LIGHT INTERACTION WITH MATERIALS

Common optical glasses have quite different characteristics when used in the UV band. In fact the normal electromagnetic description of light interaction with dielectric materials in the visible range doesn't take care of absorption. In general the intensity of a light beam traveling into a material decays according to the Beer-Lambert exponential law:

Beer-Lambert law

$$1 - \mathcal{A} = \frac{I_o}{I_i} = e^{-\alpha l} \tag{3.1}$$

Actually, the *absorption coefficient* α depends on the wavelength and is negligible for pure glasses as for air in the VIS band. In the EUV and SXR band, the extinction coefficient of glasses becomes so high that the thickness of normal optical components would completely block the incoming beam. Normal optical glasses, like Borosilicate (BK7), can work down to 300nm 17, and Quartz lenses can be made to work in the NUV range down to 200nm 18. Unfortunately, for shorter wavelengths there is lack of materials with sufficient transmission to make lenses. For that reason, in that range often mirrors are used to handle optical beams.

No transmissive materials for UV wavelengths

The *reflectance* of an interface is defined by the ratio between the incident intensity and the reflected one:

$$\mathcal{R} = \frac{I_r}{I_i} \tag{3.2}$$

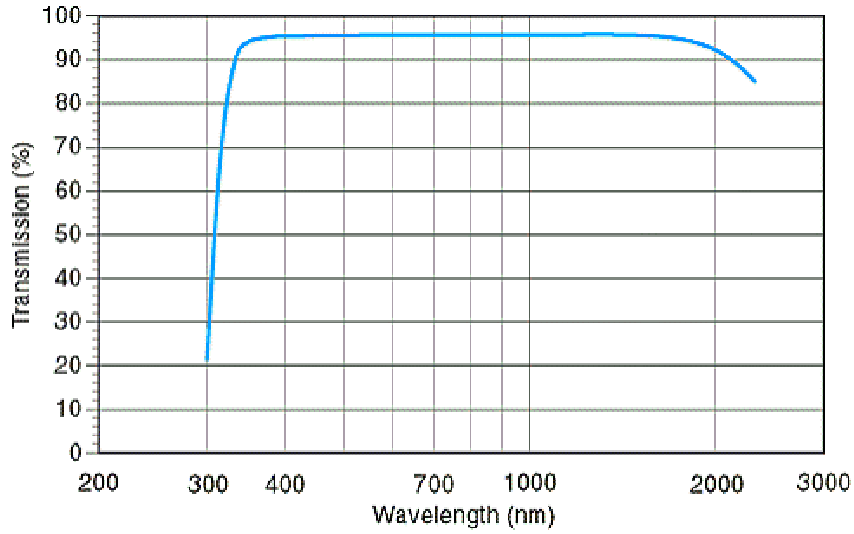

Figure 17: Spectral transmission of typical BK7 glass (source: Esco Products Inc.)

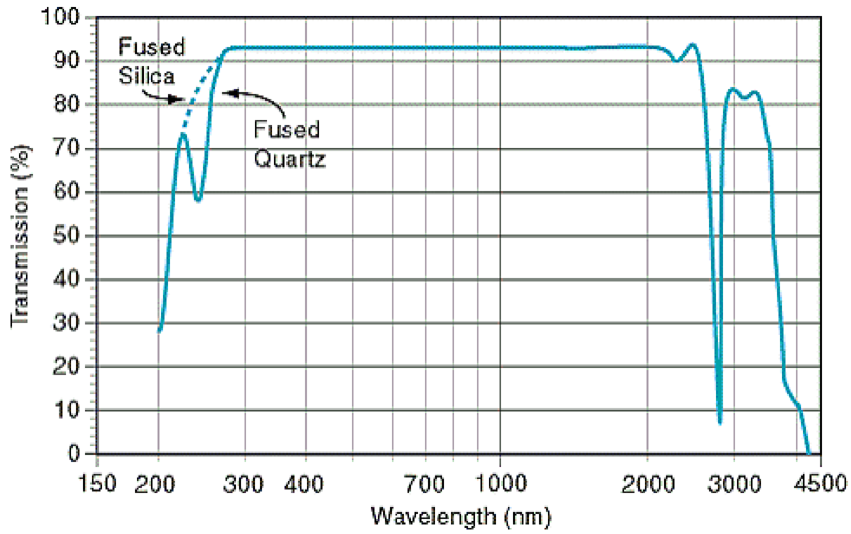

Figure 18: Spectral transmission of G1 fused Quartz/Silica (source: Esco Products Inc.)

REFLECTION IN EUV RANGE Often mirrors are realized with a metallic coating over a dielectric substrate. An example [Gul10] can be given simulating a nearly-normal (5°) incident beam reflected by an Gold coating. The reflectance value is $\mathcal{R} = 0.93$ @ 632nm but heavily decreases to $\mathcal{R} = 0.17$ @ 121.6nm, and $\mathcal{R} = 0.04$ @ 30.4nm. Aluminium coatings are known to perform well even in the UV range ($\mathcal{R} = 0.77$ @ 121.6nm), together with Silicon-Carbide (SiC), but are even less efficient than gold in EUV.

Bad reflective performance in EUV range

The solution, excluding the possibility of using grazing incidence for the reasons previously discussed, has been found not in new materials but on the coating technique.

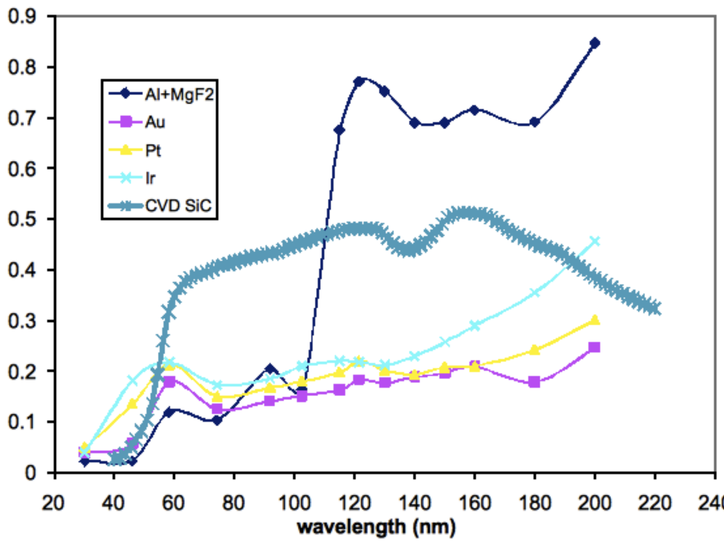

Figure 19: Spectral reflectivity of some widely used coating materials.

GRAZING INCIDENCE OPTICS Reflectance generally increases with incidence angle, as will become clear in the following and is shown on figure 20. Performance of reflective optics can be increased with setups that use *grazing incidence*. Incidence angle θ_i is defined referring to the surface normal, whereas *grazing* angle ϕ_i is defined from surface plane.

Grazing incidence has been widely used in EUV and SXR range for space and laboratory instrumentation, overcoming hard alignment problems. However, for the reasons previously discussed, new technologies require high performances also at nearly-normal incidence angles. The best technology known capable to meet these requirements is *multilayer optics*.

Disadvantages of grazing optics

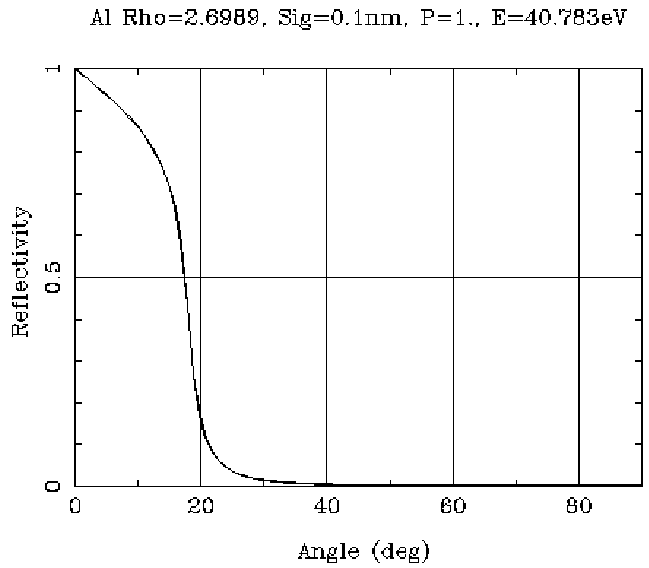

Figure 20: Reflectivity of Aluminium @ 30.4nm for increasing grazing angle ϕ_i. Over 30° reflectance is null (source: [Gul10]).

3.2 MULTILAYER STRUCTURE AND WORKING PRINCIPLE

Absorption, Reflection and Transmission

The absorbed $\mathcal{A}$, reflected $\mathcal{R}$ and transmitted $\mathcal{T}$ fraction of radiation intensity by a layer must, for thermodinamics, respect the following condition:

$$\mathcal{A} + \mathcal{R} + \mathcal{T} = 1 \tag{3.3}$$

this means that if the reflectivity is low, there has to be lot of transmitted and absorbed radiation.

But if the (less absorbing) inferior layer was coated even on the other face, there would be another reflective interface that would increase the overall reflectivity. Basically it would rescue part of the radiation that is transmitted by the first interface. A repetition of such a structure (*multilayer stack*) can lead to optimum performances, and is called a *multilayer coating mirror*.

Structure of a multilayer mirror and parameters

This structure is an alternate superposition of N thin films, one with high absorbance (*absorber*) and one more trasmissive (*spacer*). In general the selection of the two materials aims to differentiate as more as possible the difference between the indexes of refraction, keeping the absorbance under certain values. The respective thicknesses, $d_{absorber}$ and d_{spacer}, if summed, give the multilayer period:

$$p = d_{adsorber} + d_{spacer} \tag{3.4}$$

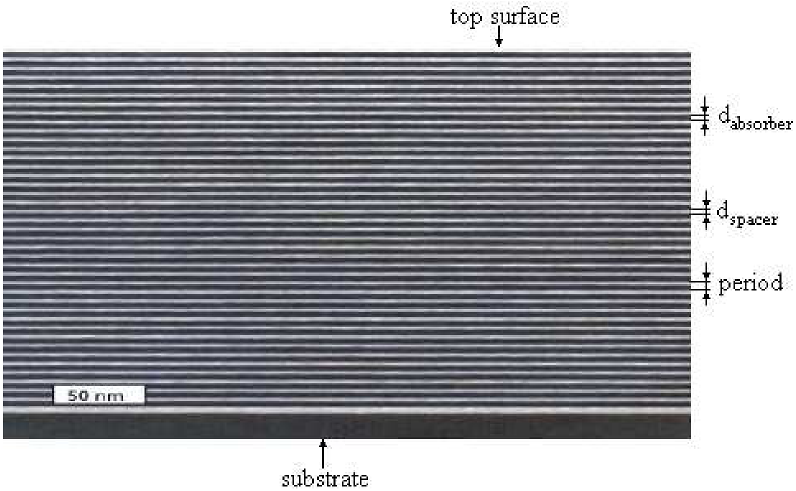

Figure 21: An image of a multilayer coating obtained by Transmission Electron Microscopy (TEM), with its physical parameters quoted (source: [Sum09]).

The multilayer ratio is instead defined as:

$$\gamma = \frac{d_{spacer}}{p} \tag{3.5}$$

Also a-periodic structure are possible, and their description parameters are more than these two, for the need to specify the thickness of each layer d_i.

3.3 FRESNEL LAWS IN ABSORBING MEDIA

An electromagnetic plane wave travelling along the direction $\hat{x}$ can be described by the equation:

Wave propagation equation

$$\vec{\mathcal{E}}(x,t) = \vec{\mathcal{E}}_0 e^{j(Kx-\omega t)} \tag{3.6}$$

where $K = \frac{2\pi}{\lambda_0} n$ is the wavenumber, comprehensive of the real index of refraction n. The *time-independent* amplitude vector notation can be used to simplify:

$$\vec{E}(x,t) = \vec{E}_0 e^{jKx} \tag{3.7}$$

This representation is valid in dielectric media, where no absorption is present. To take into account absorption, the exponential decay term from the (3.1) must be added:

$$\vec{E} = \vec{E}_0 e^{jKx} e^{-\frac{\alpha}{2}x} \tag{3.8}$$

the absorption coefficient can be incorporated into the refraction index as follows:

$$\vec{E} = \vec{E}_0 e^{j(K+j\frac{\alpha}{2})x} = \vec{E}_0 e^{j\left(\frac{2\pi}{\lambda_0}n+j\frac{\alpha}{2}\right)x} \tag{3.9}$$

$$= \vec{E}_0 e^{j\frac{2\pi}{\lambda_0}(n+j\beta)x} = \vec{E}_0 e^{jK_0\dot{n}x} \tag{3.10}$$

where has been defined the *extinction coefficient*:

$$\beta = \frac{\lambda_0 \alpha}{4\pi} \tag{3.11}$$

Complex refraction index

and the *complex index of refraction*[1]:

$$\dot{n} = n + j\beta \tag{3.12}$$

which is generally a nonlinear complex function of the wavelength.

At the interface between two absorptive materials, the complex-domain Fresnel laws[2] describe the reflected and transmitted fraction of both the s-polarized (normal to the incidence plane) and the p-polarized components of the incident amplitude vector $\vec{E}_i = \vec{E}_i^s + \vec{E}_i^p$:

Complex Fresnel laws

$$\frac{\vec{E}_i'^s}{\vec{E}_i^s} = \frac{\dot{n}_i \cos\theta_i - \dot{n}_j \cos\theta_j}{\dot{n}_i \cos\theta_i + \dot{n}_j \cos\theta_j} = r_{ij}^s \tag{3.13}$$

$$\frac{\vec{E}_j^s}{\vec{E}_i^s} = \frac{2\dot{n}_i \cos\theta_i}{\dot{n}_i \cos\theta_i + \dot{n}_j \cos\theta_j} = t_{ij}^s \tag{3.14}$$

$$\frac{\vec{E}_i'^p}{\vec{E}_i^p} = \frac{\dot{n}_i \cos\theta_j - \dot{n}_j \cos\theta_i}{\dot{n}_i \cos\theta_j + \dot{n}_j \cos\theta_i} = r_{ij}^p \tag{3.15}$$

$$\frac{\vec{E}_j^p}{\vec{E}_i^p} = \frac{2\dot{n}_i \cos\theta_i}{\dot{n}_i \cos\theta_j + \dot{n}_j \cos\theta_i} = t_{ij}^p \tag{3.16}$$

where the refraction angles are linked by the Snell's law:

$$\dot{n}_i \sin\theta_i = \dot{n}_j \sin\theta_j \tag{3.17}$$

The overall reflectance is defined upon the mean of intensities and goes with the squares:

$$\mathcal{R} = \frac{\mathcal{R}_s + \mathcal{R}_p}{2} = \frac{\|r^s\|^2 + \|r^p\|^2}{2} \tag{3.18}$$

The Fresnel's coefficients can be easily calculated for any incidence angle.
It's easy to see that, when $\dot{n}_i \to \dot{n}_j$, it is $r_{ij} \to 0$ and $t_{ij} \to 1$, so that there is no reflection. This means that when the complex refraction indexes are not much different, the reflection performance drops; this problem, called *lack of optical contrast*, is typical of materials in the EUV and SXR range, and is the reason of the poor performance of single interface mirrors. Anyway, trying to maximize it with specific couples of materials is a base line for the amplification given by the stack.

1 The sign of the imaginary part can be defined positive or negative for convention. Both results can be obtained changing the arbitrary sign of propagation term $(jKx - \omega t)$.

2 Being $\cos\theta$ a possibly complex number from these equations, its physical meaning is different, as it contains also information on reflection phase. The analytical definition is $\cos(\theta) = \cosh(j\theta),\ \theta \in \mathbb{C}$.

SPECULAR REFLECTANCE LOSS In an ideally abrupt interface, the reflection is completely specular, meaning that every ray is reflected with the same incidence angle from the surface plane. This does not happen when the surface is not ideal, i.e. has a punctual distance offset $e_S(x, y)$ (profile function) from the ideal plane, producing scattering. For imaging and, in general, precision optical applications, only the specular reflectance is of interest, that is the total reflectance minus the scattered light. To take into account the problem, defining the *rms roughness* of the surface as the standard deviation:

$$\sigma^2 = \frac{1}{S} \int\int_S \|e_S^2(x, y)\| dx dy \tag{3.19}$$

the Fresnel's coefficients from (3.13) and (3.15) can be corrected to describe only specular reflectance with the *Debye-Waller factor* [Spi94]:

Debye-waller corrective factor

$$r' = r \cdot e^{-2\left(\frac{2\pi\sigma\cos\theta_i}{\lambda}\right)} \tag{3.20}$$

This parameter can alternatively be used to describe the *diffusion* of the interface (that is the progressive change of refraction index due to non ideal discontinuity of materials), or, eventually, a combination of the two non-idealities.

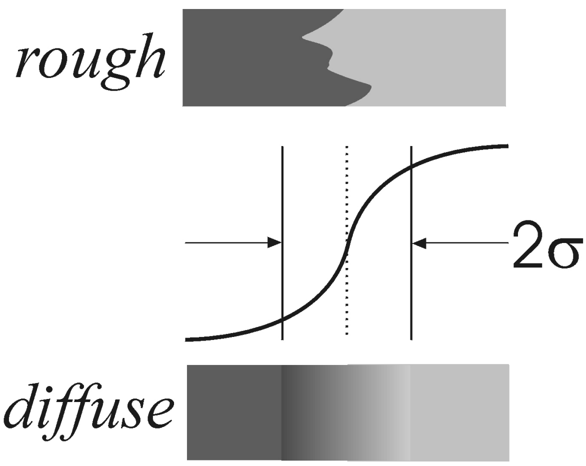

Figure 22: Standard deviation of profile function, quantifying roughness or diffusion (source: [Win98]).

3.4 OPTICAL FUNCTION OF A MULTILAYER STACK

Having the corrected reflection and transmission Fresnel's coefficients for two interfaces (i, j), (j, k) is possible to calculate the overall reflectivity coefficient of the stack.

Reflection contributes inside a coating layer

From the scheme 23 the reflection contributes are clear:

- r_{ij} the light part directly reflected by the (i, j) interface,

- $t_{ij} r_{jk} t_{ji}$ the light part transmitted by the (i, j) interface, reflected by (j, k) and lastly retransmitted by (j, i);
- $t_{ij} r_{jk} (r_{ji} r_{jk})^n t_{ji}$ the light part transmitted by the (i, j) interface, reflected by (j, k), bouncing n times between (i, j) and (j, k), and lastly retransmitted by (j, i);

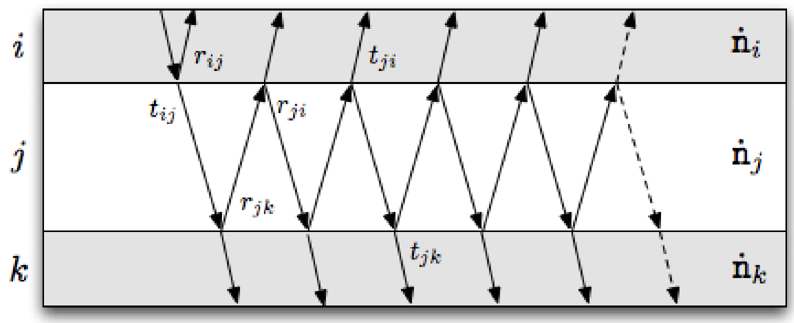

Figure 23: Multilayer reflection and transmission envelope.

Optical path difference inside the layer

Propagating between the (i, j) and (j, k) interfaces through the j material, the wave accumulates a phase delay with respect to the (i, j) direct reflection path. The scheme 24 illustrates the *Optical Path Difference* (OPD).

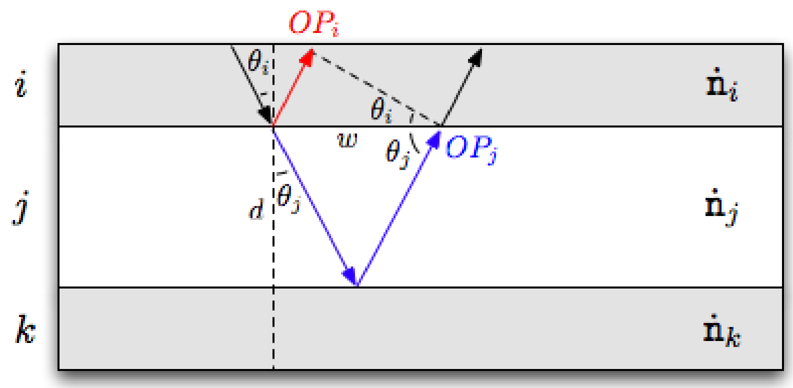

Figure 24: OPD geometrical description.

The ray reflected by the (i, j) interface has the optical path:

$$OP_i = \dot{n}_i w \sin\theta_i = 2d\dot{n}_i \tan\theta_j \sin\theta_i \tag{3.21}$$

being $w = 2d \tan\theta_j$, whereas the ray reflected by the (j, k) interface:

$$OP_j = \frac{2d\dot{n}_j}{\cos\theta_j} \tag{3.22}$$

computing the difference between (3.22) and (3.21) and applying the (3.17):

$$\mathrm{OPD} = \frac{2d}{\cos\theta_j}(\dot{n}_j \sin^2\theta_j - \dot{n}_j) = 2d\dot{n}_j\cos\theta_j \tag{3.23}$$

so the phase delay is:

$$\varphi = \frac{4\pi d}{\lambda_0}\dot{n}_j\cos\theta_j \tag{3.24}$$

Finally, this is the sum of the *superposition principle* modulating each contribute with its own phase difference:

Single-layer optical function from Fresnel coefficients

$$r = r_{ij} + t_{ij}r_{jk}e^{j\varphi}\sum_{n=0}^{\infty}(r_{ji}r_{jk}e^{j\varphi})^n t_{ji} = r_{ij} + \frac{t_{ij}t_{ji}r_{jk}e^{j\varphi}}{1 - r_{ji}r_{jk}e^{j\varphi}} \tag{3.25}$$

where the geometric series is also calculated, leading to what is called the Airy's formula. Substituting the following two relationships coming from Fresnel's equations:

$$t_{ij}t_{ji} + r_{ij}^2 = 1 \tag{3.26}$$

$$r_{ij} = -r_{ji} \tag{3.27}$$

the optical functions for the transmission and reflection coefficients for the (i, j, k)-stack are obtained [Spi94].

$$r = \frac{r_{ij} + r_{jk}e^{j\varphi}}{1 + r_{ij}r_{jk}e^{j\varphi}} \tag{3.28}$$

$$t = \frac{t_{ij}t_{jk}e^{j\varphi}}{1 + r_{ij}r_{jk}e^{j\varphi}} \tag{3.29}$$

This approximation takes no care of the specular loss issue, but allows to understand the advantages of this technology: let the three-layer sample be composed of[3]:

Three-layer reflection example

- i: vacuum, $\dot{n}_i = 1$
- j: molibdenum, $d = 10\mu m$, $\dot{n}_j = 0.9080 + j0.4302$
- k: a-silicon, $\dot{n}_k = 0.9337 + j0.0084$

Using for instance an incidence angle $\theta = 45°$, equations (3.13) and (3.15) give the complex Fresnel coefficients:

$$r_{ij}^s = -0.1299 - j0.3579 \qquad r_{ij}^p = +0.1112 - j0.0930 \tag{3.30}$$

$$r_{jk}^s = +0.2093 + j0.3375 \qquad r_{jk}^s = -0.1165 + j0.0945 \tag{3.31}$$

and (3.28) gives the three-layer reflectivity coefficient:

$$r_{ijk}^s = -0.1645 - j0.3816 \qquad r_{ijk}^p = 0.1191 - j0.1047 \tag{3.32}$$

The reflectance values calculated with (3.18) can then be compared.

$$\mathcal{R}_{ij} = 0.0830 \qquad \mathcal{R}_{ijk} = 0.0989 \tag{3.33}$$

3 Refractive indexes were taken from database supplied by IMD software [Win98].

This means that the light reflected by the second interface enhances the performance of the system of more that 16%. Adding layers to the system will then lead to widely better results.

The preceding calculus is valid for a two-interface mirror. In case of a multilayer constituted by n interfaces, the computation can be done by software [Win98], iterating recursively the equation (3.25) for s/p-polarizations, corrected with the Debye-Waller factor, from the top to the bottom of the stack. Then the overall reflectance can be obtained from (3.18).

BRAGG'S LAW The reflectivity modulation by the phase delay calculated in (3.24) causes a variation on the overall reflectance values. This means that when wavefront are subject to constructive interference, reflective performance is better than in other conditions, i.e.:

$$\mathrm{OPD} = m\lambda \;\Rightarrow\; \varphi = 2\pi m\,, \; m \in \mathbb{R} \tag{3.34}$$

The Bragg's law, born to describe reflection from crystal atom scattering, can be modified [Spi94] to describe the condition in which the OPD between a periodic structure composed by two materials i, j is multiple of the wavelength (with the assumption $\beta \ll \delta \ll 1$ and $\phi_i = \frac{\pi}{2} - \theta_i$[4]):

Bragg's law on wavelength

$$m\lambda_0 = 2p\sin\phi_i\sqrt{1 - \frac{2\delta}{\sin^2\phi_i}} \qquad \delta = 1 - \frac{n_i d_i + n_j d_j}{p} \tag{3.35}$$

It's clear that the choose of a precise period and ratio optimizes the stack for a precise λ_0 (and its harmonics). The equation, through some mathematical approximation, can explicit the grazing angle [YZ08]:

Bragg's law on grazing angle

$$\sin^2\phi_i = \left(\frac{\lambda_0}{2p}\right)^2 m^2 + 2\delta \tag{3.36}$$

This shows that the reflective performance is also better at certain angles determined by the integer values of m.

Actually, the relations (3.35) and (3.36) are valid under the assumption that the wave completely penetrates the stack (which is true for X-rays but may not for longer wavelengths). In many bands (especially with longer wavelengths) the penetration depth is lower and involves only the first layers. In this cases these effects are less present and the spectral reflectivity is less dynamic.
This law is widely used for multilayer optimization, and even more for analysis (X-Ray Reflectometry), as it leads to know the ML structure from periodicity of spectral and angular response.

OPTICAL CONSTANTS It becomes clear that the precise knowledge of *optical constants* (i.e. the complex refraction index, in function of the wavelength) of the materials constituting the stack is necessary to design and simulate correctly the optical device. These constants can

4 Often in SXR range that ϕ_i grazing angle is used instead of incidence angle.

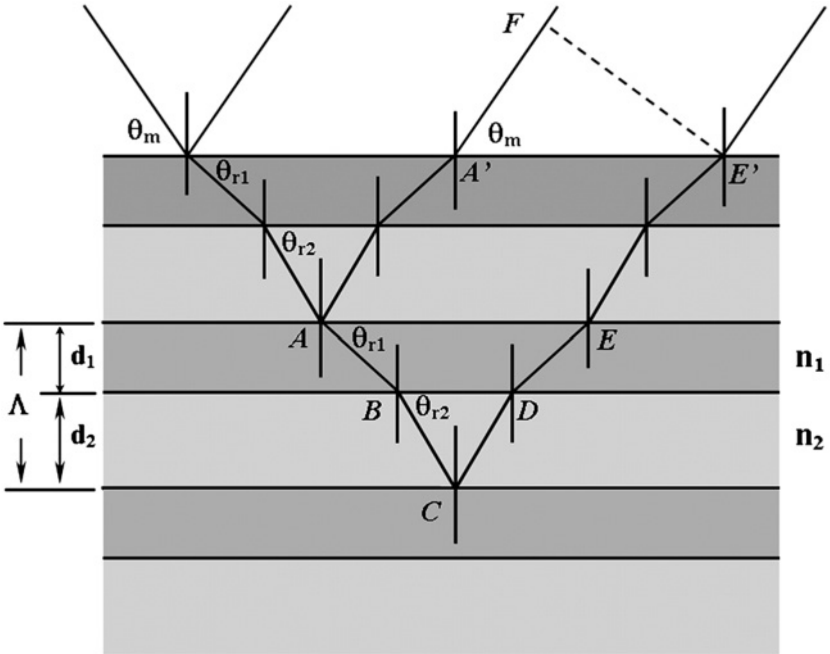

Figure 25: Multiple reflection lightpaths inside multilayer stack that should add in phase (source: [YZ08]).

be in first analysis computed from the microscopic property of matter (*atomic scattering factors*) and are often available on handbooks and online databases [Pol10, Gul10]. Unfortunately, the influence of many factors especially at SXR wavelengths and the dependence from the coating and deposition technique make these data somewhat unreliable.

Need for further optical constants investigation

Directly measured optical constants should grant more accuracy, but often such data is not available at the needed wavelengths. In order to improve design and simulation efficiency, the possibility to perform these measurements directly on the materials used is being evaluated.

3.5 DESIGN METHOD

The optimization process used for the design of the following multilayer samples starts from determining the ML period p and ratio γ with the chosen materials. This is generally done with considerations upon constructive interference, based on Bragg's law.

In case of periodic multilayers, often $p \approx \lambda/2$ is used. This tunes the ML response for best performance on a precise wavelength λ_{peak}, that will be the main operating point. Further optimization is generally done by software simulation, using the optical functions previously presented.

CAPPING LAYER A *capping layer* is a small-N multilayer stack designed to be superimposed to the multilayer. It is composed by materials chemically compatible with the ones composing the stack below, in order not to alter their composition. Its main task is to preserve the multilayer structure from aging, shielding it to deteriorating agents, such as atmospheric gases or high energy particles to which the device could be exposed in space applications.

Capping layer as shield and enhancer

The CL structure can also be optimized to enhance the spectral performance of the multilayer. For instance, in case of solar physics applications 1, the ML is wished to work also in wavelengths $\lambda_{\mathtt{sec}}$ different from the principal one. This is done by optimizing the CL structure to have high reflectance on this secondary wavelength. Usually, that is longer than the principal one, allowing to rely on lower penetration depth.
Instead, for FEL pulse filtering, the CL can be designed to reject a specific harmonic of $\lambda_{\mathtt{peak}}$, thus suppressing the overall reflectance of the mirror in the near band.

In general, no matter what capping layer is used, the VIS performance tends to be constantly high, as only the uppermost layer is actually involved in reflection at these wavelengths, and so no interference issues can alter reflectivity.

3.6 MULTILAYER SAMPLES

Many multilayer samples have been designed at LUXOR laboratories for the METIS UVC main mirrors [CSM+10]. The samples were then deposited by *Reflective X-ray Optics LLC, NY* (RXO) over a 16x16mm polished Silicon substrate [Cor10]. Because of their good time stability, Si/Mo multilayers have been widely used for all the EUV wavelengths, even if their performance at longest wavelengths is not optimal. For this reason also other types of materials have been tried in the design.

Optimization applied on produced ML samples

An innovative optimization process has been used [Sum09] to design these samples, based on *standing wave optmization*. Actually, the "trapping" of radiation between the stacked layers generates standing waves between the interfaces. The standing-wave intensity across the ML structure can be simulated, and if the nodes of $\lambda_{\mathtt{peak}}$ are located in correspondence of absorber material, the attenuation of that wavelength is minimized.
Similarly, the nodes of a near $\lambda_{\mathtt{noise}}$ can be located on the spacer material, leading to a strong suppression of this line. For space observation, in which often unwanted noise lines are present near the principal one, this technique should let to narrow the observation band, and so to improve the overall SNR of the instrument.

The produced samples have been tested and the results will be presented and discussed in the following chapters. Their design parameters are reported in table 2.

Figure 26: METIS samples ready for testing.

Sample ID	ML materials	ML p	ML γ	ML N	CL materials
ML0	a-Si/Mo	16.40 nm	0.82	35	None
ML0/CL0	a-Si/Mo	16.40 nm	0.82	35	1 nm a-SiO_2 1 nm a-Si
ML0/CL1	a-Si/Mo	16.40 nm	0.82	35	2 nm Ir 2.2 nm Mo
ML0/CL2	a-Si/Mo	16.40 nm	0.82	35	2 nm Ir 15.4 nm a-Si 2.95 nm Mo
ML0/CL3	a-Si/Mo	16.40 nm	0.82	35	2 nm Ru 2 nm Mo 14 nm a-Si 3 nm Mo[5]
ML0/CL4	a-Si/Mo	16.40 nm	0.82	35	2 nm W
ML1	Ir/a-Si	16.84 nm	0.28	30	None
ML1/CL0	Ir/a-Si	16.84 nm	0.28	30	2.2 nm Ir 13.5 nm a-Si
ML2	Zr/Al	16.2 nm	0.19	30	None
ML2/CL0	Zr/Al	16.2 nm	0.19	30	4.6 nm a-Si
ML2/CL1	Zr/Al	16.2 nm	0.19	30	2 nm a-SiC 16.4 nm Al
ML2/CL2	Zr/Al	16.2 nm	0.19	30	2 nm B_4C 3.2 nm Al

Table 2: METIS samples parameters.

SAMPLES FOR FEL Among the produced samples, only the ones with Si/Mo coatings are expected to have low reflectance values on the 60.8nm line, that is a possible fundamental line in the emission of FEL experiments (having its third harmonic at 20.3nm). They could then act as reflection suppressors for the delay line described in chapter 2. Their reflectance will then be tested to verify if it is sufficiently low at 60.8nm.

Test for FEL application of Si/Mo sample

SAMPLES FOR SCORE Some samples are available from the HERSCHEL project. This joint NASA-ASI mission [Age10] consisted a sounding rocket[6] named *Sounding-rocket Coronagraphic Experiment* (SCORE), whose payload included a first version of the METIS coronagraph. The aim was to test the device in those that will be its operating conditions in the space. On 28 Set 2009, the SCORE instruments delivered the first EUV image of the solar corona.

SCORE Mg/SiC samples

SCORE used an off-axis gregorian telescope, which optical components were Mg/Sic multilayers (with different capping layers) designed at LUXOR laboratories and deposited at RXO. Mg/SiC was known to have good thermal and mechanical properties. The reflectivity performances were measured in VIS, UV, EUV bands in 2006. New measurements were took and will be discussed in this work. They will be useful to estimate the aging of the samples and the data comparison will allow to detect any anomaly in the measurement process used.

Available Mg/SiC stored samples

Sample IDs were A06011 until A06017, and A06021until A06024. Unfortunately, no precise information was available about the capping-layers deposited on these samples.

3.7 COATING TECHNIQUE

The realization of such a device implies being able to coat a material with a layer of another one of precise thickness. In general, coating techniques are the methods to atomize the coating material, called the *target*, and drive the free atoms towards the *substrate*, in a way that grants an uniform distribution of the atomized material. The repetition of this procedure leads to the desired stacked structure.

DC magnetron sputtering technique

The multilayer samples for METIS and SCORE have been deposited through *DC magnetron sputtering*. Sputtering consists [PVD10] in removing superficial atoms from the target through ion bombardment. The substrate is located in front of the target into a chamber filled with low-pressure Argon gas. When the target is given a ~300V negative bias, the naturally (due to cosmic radiation) ionized Ar^+ ions are accelerated towards it, and the collision has the double effect of freeing superficial atoms (that will be randomly directed at the substrate) and secondary electrons, whose presence will cause further gas ionization. The bias current is DC as the target material is a conductive metal, oth-

5 Not yet deposited, so it was not available in the period of the measurement campaign.

6 A *sounding rocket* is an instrument-carrying rocket designed to take measurements and perform scientific experiments during its sub-orbital flight.

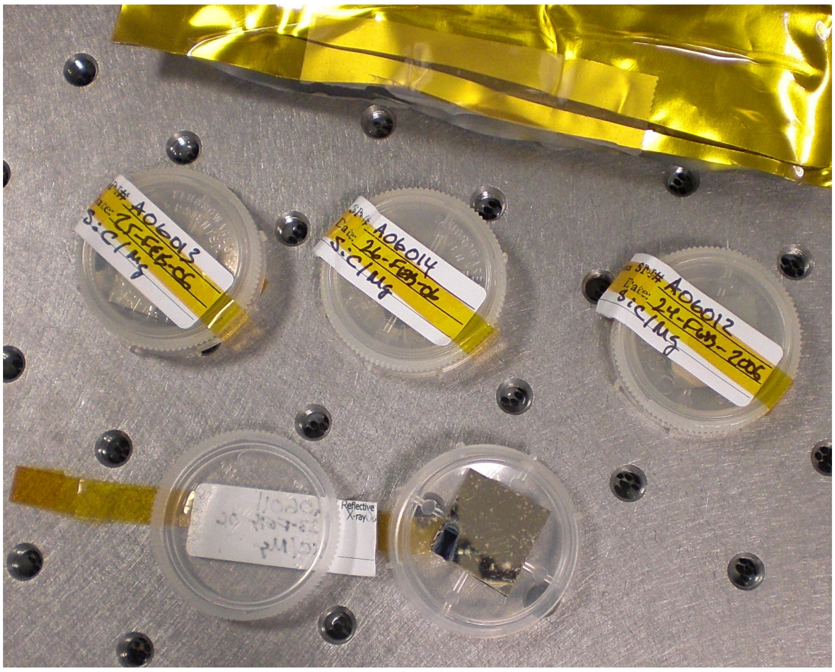

Figure 27: SCORE samples ready for testing.

erwise an AC voltage is used to avoid surface charging.
In magnetron sputtering, the presence of a strong magnetic field near the target surface forces secondary electrons to follow longer helical paths, increasing the ionization probability and allowing plasma formation at pressures even hundred times lower. These pressures reduce the collision probability of the sputtered atoms, that will reach the substrate with higher kinetic energy. Otherwise, the formation of more ionized atoms at the same pressure, will strongly increase the sputtering rate. Finally, the magnetic confinement prevents electrons from hitting the substrate target causing overheating and structural damage.

Strong magnetic field to catalyze the process

The main advantage of this technique over older methods like *Thermal Evaporation* is first of all very stable deposition rate, that allows the thickness control by timing with errors down to 0.1Å (thickness tolerance imposed by (2.6) at EUV wavelengths is about 100 times smaller than that for VIS band coatings). Moreover, the substrate holder can be set to rotate past many targets, allowing alternate sequential depositions. Finally, the kinetic energy of sputtered atoms can be tuned with the electric field to optimize the process.

DC sputtering advantages

PERFORMANCE FACTORS The performance of the produced sample can be influenced by the process parameters, causing many types of deviations from the ideal design specifications [Sum09]:

- *boundary quality* of the interfaces;
- *optical constants* uncertainty;

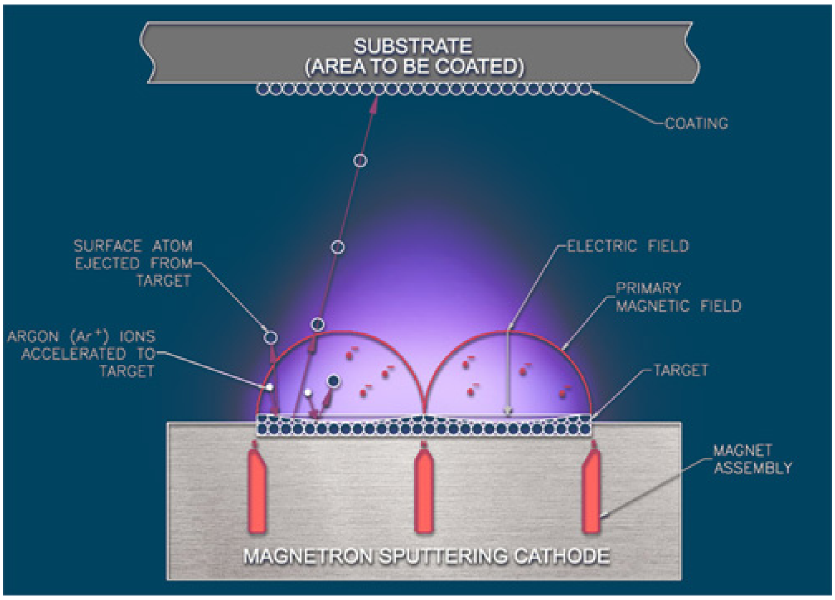

Figure 28: Magnetron DC sputtering working diagram (source: [PVD10]).

- *contamination* especially of the spacer layer;
- *mixing* of the coating materials;
- *thickness error* of the layers (small thanks to deposition technique itself);
- *flatness* of the overall coating.

Roughness and flatness are strongly process-dependent

The surface roughness of the polished substrate can also influence the deposited coatings, and should be kept 10 times lower than period p. Flatness of the multilayer structure is also important to minimize wavefront deformation and should be kept under certain values, as discussed in section 2.4. The coating technique can dramatically influence the flatness, as the thickness of the layers often tends to reduce near the boundaries.

These factors have to be considered during the evaluation of the test results, as poor efficiency could not exclude that a possibly good design was wasted by an imprecise implementation.

AGING AND DETERIORATION Many agents are responsible for the deterioration of the samples, that can occur for external agents or for internal interaction between the layer materials, causing loss of reflective performance:

- *interdiffusion* the chemical compatibility of the materials is so high to allow them to diffuse at the interface, causing the degradation of specular reflectance as described by (3.20)[7];

7 Often an inter-layer material is used to minimize this phenomenon.

- *oxidation*: the exposure to air can oxidate the topmost layers of the stack, altering the optical constants;
- *particle collisions*: especially in case of space applications, the collision of high energy particles (alpha particles, protons) can damage the crystalline structure of the layers;
- *thermal irradiation*: thermal cycles can damage the structure causing internal strains, whereas high energy flux can increase the multilayer temperature until causing annealing of crystalline layers, with formation of other compounds;
- *corrosion*: corrosive gases can attack the topmost layers, altering the optical constants or damaging the structure.

Thermal irradiation and particle collisions are mainly involved in space applications

4 MEASUREMENT FACILITIES

CONTENTS

To measure the reflective performance of the samples two different types of instrumentation have been used: a commercial UV-VIS-NIR spectrophotometer for the measures in VIS and near-UV band, and a spectrophotometric facility available at LUXOR for the UV band, because for that high vacuum conditions were needed.
In addition, the mirror flatness has been tested against requirements discussed in chapter 2 with a laser interferometer available at LUXOR-DEI clean room facility.

4.1 DIFFRACTION GRATINGS AND MONOCHROMATORS

A *diffraction grating* is a device used to deflect light radiation with different angles dependent on the wavelength. The first types of diffraction gratings were transmission based. The behaviour of such a device [HZ03] can already be seen from well-known Young double-slit experiment: the period of the diffraction pattern is known to be equal to $\frac{\lambda d}{a}$, so it is dependent from the wavelength. The components of a polychromatic incident beam would then be separated into different diffraction patterns.

Transmission diffraction gratings

A *transmission diffraction grating* is made by increasing the number of slits N. Let P be a point chosen on a screen at distance d and angle θ_m from the multi-slit grating whose period is $a \ll d$. P is interested by the interference of N waves with equal amplitudes E_0 and constant phase delays [ST07]:

$$\varphi_n = (n-1)ka\sin\theta \tag{4.1}$$

The sum is easily calculated through the series:

$$\vec{E}_P = \sum_{n=0}^{N} E_0 e^{j\phi_n} = E_0 \frac{1-e^{jNka\sin\theta_m}}{1-e^{jka\sin\theta_m}} \tag{4.2}$$

$$I_P = I_0 \frac{\sin^2\left(N\frac{\pi}{\lambda}a\sin\theta\right)}{\sin^2\left(\frac{\pi}{\lambda}a\sin\theta_m\right)} \tag{4.3}$$

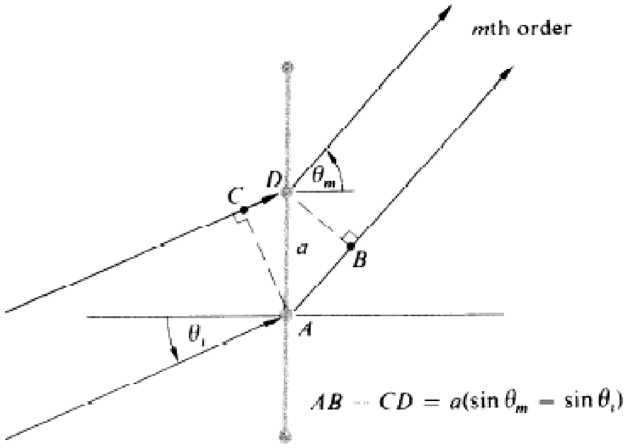

Figure 29: OPD between adjacent slits in a transmission grating (source: [HZ03]).

The intensity profile is a periodic function that has intense peaks when the constructive interference condition is satisfied, i.e.:

$$\frac{\pi}{\lambda} a \sin\theta_m = m\pi \qquad m \in \mathbb{Z} \tag{4.4}$$

Grating equation for transmission

giving the *grating equation*:

$$a \sin\theta_m = m\lambda \qquad m \in \mathbb{Z} \tag{4.5}$$

where m is called the *order*. This means that each wavelength is projected multiple times on the screen with an angular period proportional to its λ. In case that the incident light is polychromatic, it is decomposed into its spectrum, as all spectral lines will have different periods, except for *order zero* ($m = 0 \Rightarrow \theta_0 = 0 \ \forall \ \lambda$) where there is no wavelength distinction.

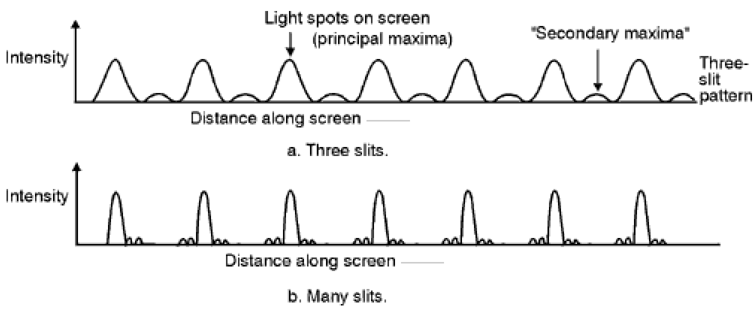

Figure 30: Grating single-wavelength diffraction pattern, increasing with the number of slits (source: [Cen88]).

Reflective diffraction gratings

Other types of diffraction gratings exist, each one dealing with a different way to introduce a spatial phase modulation. *Reflective gratings* are widely used, especially for the EUV transmission issues discussed. A periodically modulated surface is coated with a reflective layer. The most used among them is the *blazed grating*, where the surface has a toothsaw profile of period a and *blaze angle* ϕ.

Blazed gratings

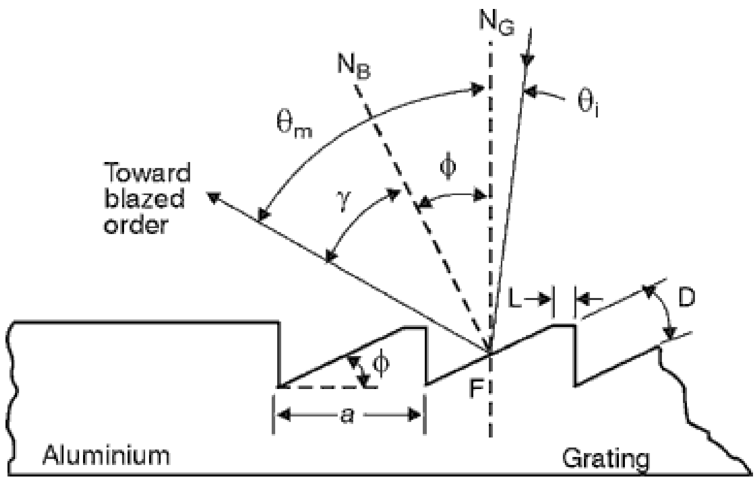

Figure 31: Blazed grating layout (source: [Cen88]).

Starting from figure 31, considered a point P on the screen as before, the phase delay can be calculated:

$$\varphi_n = (n-1)ka(\sin\theta_m - \sin\theta_i) \tag{4.6}$$

and so the grating equation, similarly to (4.5), is:

Grating equation for reflection

$$a(\sin\theta_m - \sin\theta_i) = m\lambda \qquad m \in \mathbb{Z} \tag{4.7}$$

The main advantage of these gratings is to shift energy out of useless zero order to higher order spectra. In fact, when the incident wave is normal to the reflecting elements ($\theta_i = 2\phi$), diffraction and specular reflection occur at the same time. In this way the main part of intensity is directed normal to the surface ($\theta_m = \theta_i - 2\phi = 0$) and the grating equation becomes:

$$a\sin(-2\phi) = m\lambda \qquad m \in \mathbb{Z} \tag{4.8}$$

this means that, given ϕ, this condition verifies only for each wavelength at a certain order (different from zero), so the spectral peak of other wavelengths won't be so intense. A blazed grating can be designed to work in this setup (called Littrow configuration) and be tuned for a specified λ, called *Blaze wavelength at m-th order*.

The emission of a diffraction grating is characterized by the following parameters:

Grating performance parameters

- *maximum order*: given a wavelength λ, the maximum visible order is when θ_m approaches to $\frac{\pi}{2}$:

$$m = \left\lfloor \frac{a(\sin\frac{\pi}{2} - \sin\theta_i)}{\lambda} \right\rfloor \qquad 0 < \theta_i < \frac{\pi}{2} \tag{4.9}$$

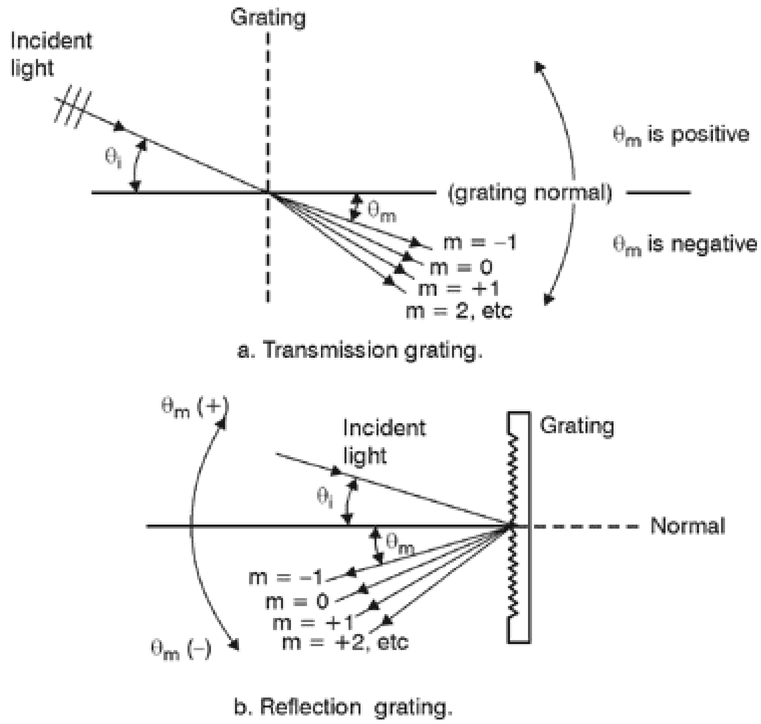

Figure 32: Diffractions gratings and order disposition (source: [Cen88]).

- *angular line width*: the peaks of law (4.3) have zeros on either size at distance $\Delta\varphi = \frac{2\pi}{N}$. This phase difference can be expressed, at constant incidence angle, as:

$$\Delta\varphi = \frac{2\pi}{N} = \frac{ka}{2}\Delta\theta_m \cos\theta_m = \frac{2\pi}{N} \tag{4.10}$$

so the width of a single line is dependent on wavelength and grating period:

$$\Delta\theta_m = \frac{2\lambda}{Na\cos\theta_m} \tag{4.11}$$

Dispersion determines angular bandwidth

- *angular dispersion*: differentiation of (4.7) allows to determine the difference in position corresponding to a difference in wavelength:

$$\mathcal{D} = \frac{\partial\theta}{\partial\lambda} = \frac{m}{a\cos\theta_m} \tag{4.12}$$

meaning that the dispersion is larger with higher orders. Large dispersion is useful to select a precise wavelength with a slit in a monochromator.

- *resolving power*: two wavelengths with small difference often overlap on the screen. We define the minimum separation between two wavelengths when the principal maximum of the first coincides with the first minimum of the second (Lord Rayleigh's criterion). So angular separation is at minimum the half of a line from (4.11):

$$\Delta\theta_{min} = \frac{\lambda}{Na\cos\theta_m} \tag{4.13}$$

The angular dispersion of two lines is:

$$\Delta\theta_{min} = \frac{m\Delta\lambda_{min}}{a\cos\theta_m} \tag{4.14}$$

The resolving power is obtained combining (4.13) and (4.14), and is defined as follows:

Equation for resolving power, most important parameter

$$\mathcal{R} = \frac{\lambda}{\Delta\lambda_{min}} = mN \tag{4.15}$$

$$= \frac{Na(\sin\theta_m - \sin\theta_i)}{\lambda} \tag{4.16}$$

- *free spectral range*: this is the spectral range within which wavelengths of different orders are guaranteed not to overlap:

$$(m+1)\lambda = m(\lambda_{fsr} + \Delta\lambda) \Rightarrow \Delta\lambda_{fsr} = \frac{\lambda}{m} \tag{4.17}$$

A functional grating for a certain application is a compromise between these design factors, to provide high dispersion (to select a single line) but also high resolution (to reject unwanted lines).
Many other reflection grating types are available like *grooved* or *holographic* ones; anyway they are all based on the same principle and they share much part of the mathematization.

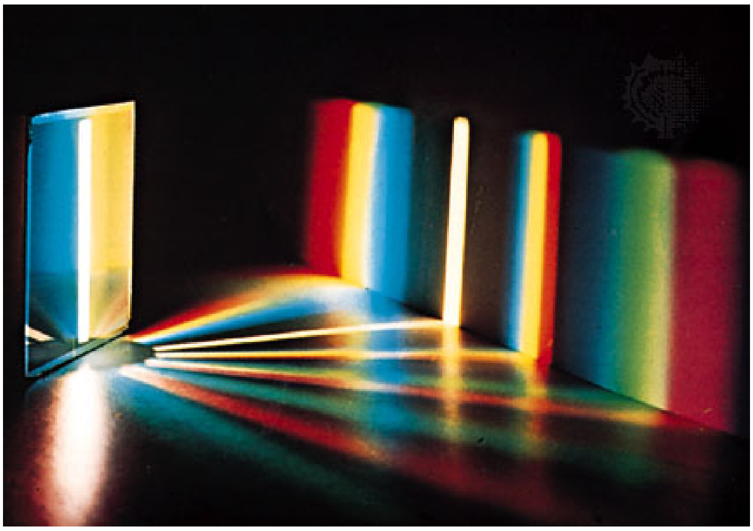

Figure 33: Diffraction pattern projected by a reflection grating.

MONOCHROMATORS A monochromator is a device used to mechanically select a narrow band of radiation. Its main component is a diffraction grating. To satisfy the conditions for the grating equations, a light beam is first of all collimated onto the grating. With various methods, a diffracted order is directed towards a slit and spatially filtered. *Stray light* and *wavelength range* are important functional parameters that lead to different setups, but the most important is the *spectral bandwidth*, which is the FWHM[1] spectrum allowed through the slit, dependent on its angular aperture $\Delta\theta_s$:

Monochromator spectral bandwidth

$$\mathcal{B} = \frac{\Delta\theta_s}{\mathcal{D}} \tag{4.18}$$

4.2 CARY 5000 UV-VIS-NIR SPECTROPHOTOMETER

A *spectrophotometer* is a device used to measure the energy density of an electromagnetic absorption or emission spectrum. A typical absorption spectrometer uses a monochromator to produce a precise wavelength emission that is let through the sample (in transmission or reflection) and is then measured in intensity with a photometer. The "frequency sweep" produced by the monochromator allows to investigate the full spectral response of a linear optical system.

Absorption spectrophotometer

CZERNY-TURNER MONOCHROMATOR In a *Czerny-Turner monochromator*, reflective gratings are used in Littrow configuration, with incidence angles very near to the blaze angle. In this setup, as shown by figure 34 the entrance slit (**B**) determines the amount of light energy (**A**) directed to a collimation mirror (**C**) that focuses the beam at infinity. A rotating monochromator (**C**) produces a diffraction spectrum at its main order, and the diffracted beam is refocused onto an output slit (**F**) by a refocusing mirror (**E**). The images of the different wavelengths are located on different points on the output slit plane. The rotation of the grating determines which wavelength range passes through the slit, and the slit aperture determines the output bandwidth (**G**). The output wavelength has spurious components due to the non-punctuality of the entrance slit, that affect the resolving power.

Grating rotation determines center of bandpass

DOUBLE LITTROW MONOCHROMATOR The *Cary 5000 spectrophotometer* is manufactured by Varian, Inc. [Var04]. Its main component is a *Double Littrow monochromator*. The Littrow monochromator used is similar to the Czerny-Turner setup except that collimation (**C**) and focusing (**E**) mirrors are merged in a single paraboloidal mirror. The double Littrow monochromator inserted into this instrument is a cascade of two such devices. In this way, the band selected by the slit in the first monochromator, is further diffracted and selected. This strongly in-

Cascade of two Littrow monochromators

1 Full Width Half Maximum, that is the bandwidth calculated where intensity decays to half the maximum value.

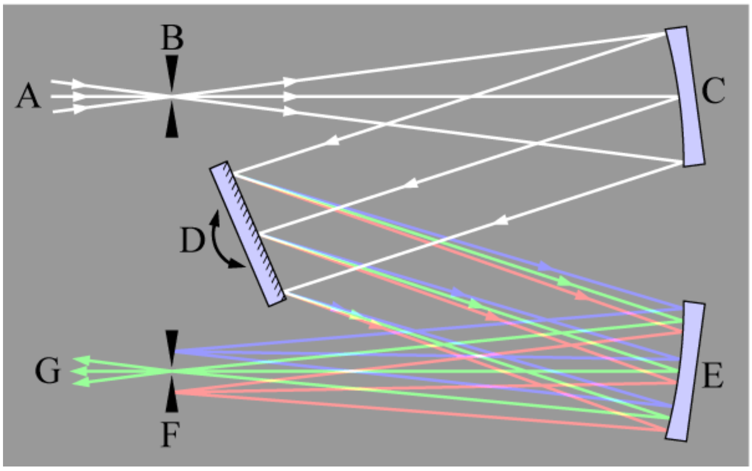

Figure 34: Czerny-Turner monochromator working scheme (source: WIKI).

creases the resolving power $\mathcal{R}$ of the instrument.
The use of blazed gratings implies that they are optimized for a specific wavelength range. As this instrument is designed to work is a wide spectral band, two gratings on each side of the same substrate are interchangeable, to cover the full band.

The Cary 5000 is designed as a *double-beam, zeroing spectrophotometer*. This means that the beam after the sample is alternatively (with 30Hz frequency) directed to the photometric sensor, passing through the sampling accessory or through the reference lightpath. In this way the reflectance R is continuously calculated from the ratio between the sampled intensity and the reference intensity, and the sensor response in not influent. Moreover, the *zeroing* feature consists on the fact that the data postprocessing is done by normalizing the raw data from the instrument to the *baseline intensity*, which corresponds to the raw measure of a white reference sample. In this way the response of the components constituting the sampling lightpath (through the sampling accessory) is also rejected.
The wavelength range of the Cary 5000 is 175-3300nm.

Double-beam ratio and baseline correction

The internal components, numbered in figure 35, are the following [Var04]:

Cary 5000 internal components

1. *light source*: as the monochromator filters an input light, this light must have sufficient energy on the passband of the monochromator, otherwise the whole input power would be wasted and no output would be produced (this issue will be specifically addressed in section 4.3). A flat-spectrum lamp for the whole instrument range is not available, so the light source is made up by a rotating drum containing many spectral lamps. A Deuterium lamp (for UV band) and a Halogen tungsten lamp (for VIS band) are installed for these measurements.

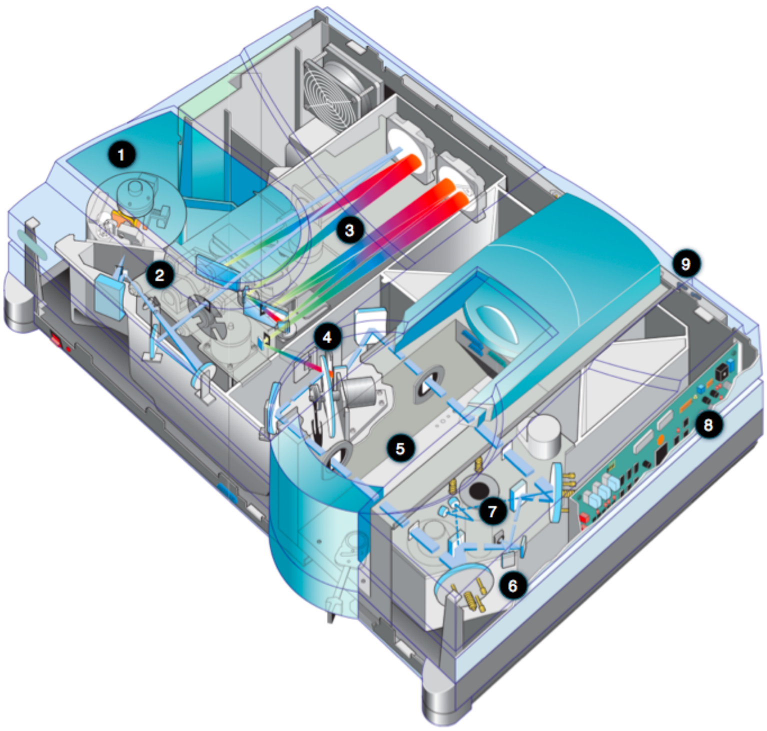

Figure 35: Cary 5000 internal components (source: [Var04]).

2. *coupling optics* are used to drive the source beam to the monochromator;

3. *monochromator*: the double Littrow monochromator occupies the centre of the instrument, and is moved by electric servo-motors. The two selectable gratings are 1200 lines/mm ($a = 0.83\mu m$), blazed for 250nm (UV+VIS), and 300 lines/mm ($a = 3.33\mu m$) blazed for 1192nm. The output slit is aperture-controlled to adjust output bandwidth.

4. *beam splitting system*: the splitting system is made of a spinning chopper that, with 30Hz frequency, reflects the beam to the sample path of the reference path.

5. *sample compartment*: through this compartment pass both the sample and reference beam (usually the latter is left unmodified). It can hold many types of accessories, to make reflectance or trasmittance measurements.

Sample compartment can hold DRA accessory

6. *refocusing optics*: two triplets of mirrors refocus both beams onto the sensor array, but only one beam is allowed at a time by the splitter.

7. *sensor array*: the photometric measure is taken by an array of sensors, to ensure good response in different spectra. For this measurements a *PhotoMultiplier Tube* is used to sense the UV+VIS. A lead-sulfide PbS photocell is available for NIR band.

8. *control electronics* interfaces the instrument with its PC application (Cary WinUV) through a GPIB (IEEE 488) connection and controls the moving parts (gratings, drum, chopper) and data acquisition from the sensors.

9. *gas purge lines*: the instrument chassis and the sample compartment can be filled with various gases to avoid contamination or light absorption by ambient air.

PHOTOMULTIPLIER TUBE The UV+VIS sensing element of Cary 5000 is a R928 photomultiplier tube manifactured by Hamamatsu Photonics K.K. [Ham06]. Its spectral sensitivity extends from 185 to 900nm. This sensor is made of a *photocathode* followed by an *electron multiplier*.

When even few photons strike the photocathode, thanks to photoelectric effect on the photocathode coating, secondary electron emission occurs. Electrons are then accelerated by a strong electric field towards an electrode and when they strike it, further emission occurs and kinetic energy causes the emission of more secondary electrons than the incident ones. A cascade of these electrodes, called *dynodes*, allows the multiplication of incoming electrons with a gain of $1.0 \cdot 10^7$ in 9 stages. Between each dynode the voltage increases of about 100 V. The last electrode is the cathode, where the accumulation of charge causes a signal current. Often this electrode is connected to a negative high-voltage power supply and the measure is done in the photocathode terminal thanks to its low voltage.

Dynode cascade provide high amplification

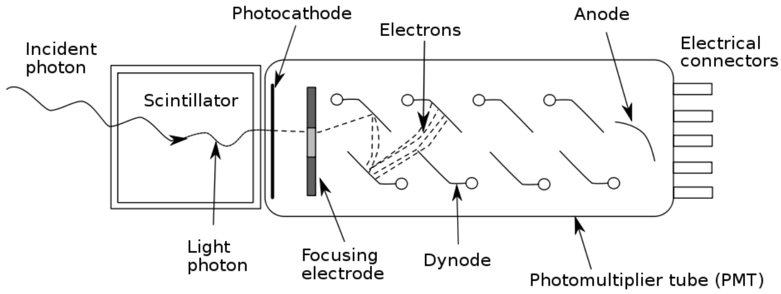

Figure 36: Photomultiplier internal structure (source: WIKI).

The very high gain, combined with low dark current (3nA and no thermal noise) allows the use of this device to perform measures in a high dynamic range.

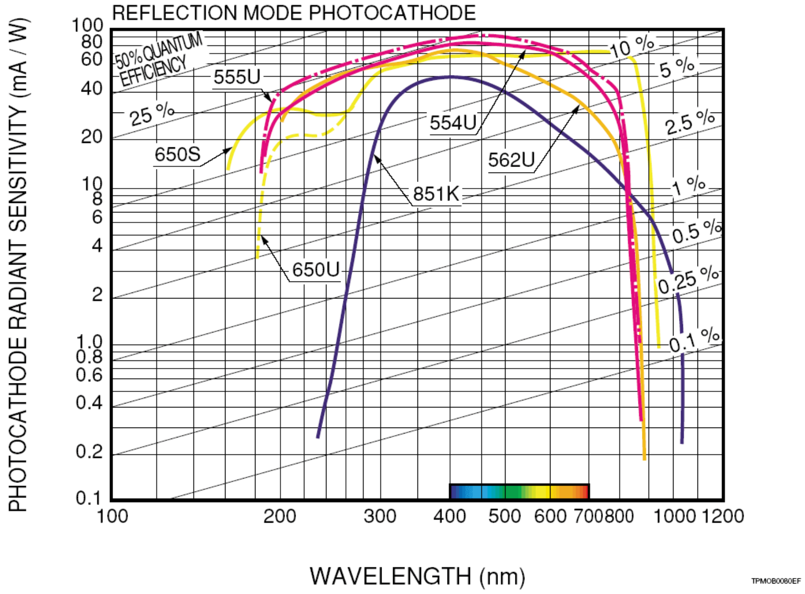

Figure 37: Spectral quantum efficiency and sensitivity of R928 PMT, see 650S (source: Hamamatsu Photonics K.K.).

DIFFUSE REFLECTANCE ACCESSORY (DRA) This accessory is made to measure the *diffuse reflectance*, that is the amount of energy not directed towards the reflection angle. This energy is captured with an *integrating* sphere. This is a 110mm hollow sphere [Var10] internally coated with Polytetrafluoroethylene (PTFE), that exhibits NIR diffuse reflectance that is superior to traditional coatings, whilst maintaining UV-Vis performance. Light beams entering in the sphere are, by multiple scattering reflections, distributed equally to all surface points and

Light integration by multiple reflection effects of the original direction of light are minimized. In this way, if the instrument beam is reflected by a sample, the whole reflected light is collected by the sphere and cannot exit from it but through the output hole directed to the sensor.

Total/Diffuse reflectance measurement

In this way *total reflectance* would be measured. But if the incident beam is let out of the sphere through the same hole it entered (normal incidence) the specular reflection amount is rejected and only the diffused light is captured.

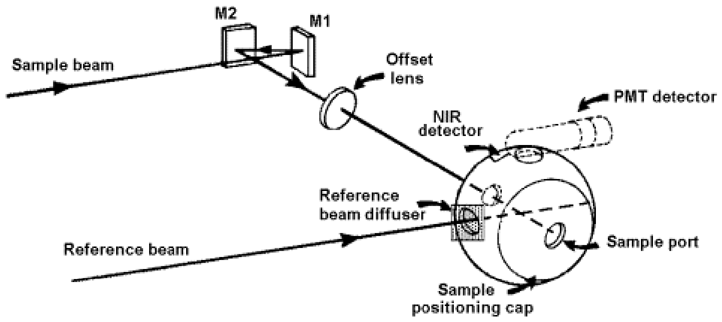

Figure 38: DRA layout (source: [Var10]).

DRA working principle

With reference to figure 38, the DRA accessory lightpath [Var10] is here described:

1. The sample beam hits mirror `M1` and is then reflected to `M2`.

2. The beam travels through the lens and is focused into the transmission port (the entrance point of the sphere), and onto the reflectance port (where the sample is positioned).

3. The reflected beam is diffused throughout the sphere before being measured by the detector.

4. The reference beam enters the sphere directly through the reference port and is dispersed (so even the attenuation induced by the integrating sphere is accounted in reference correction).

"D" and "S" positions

The sample can be mounted on the reflectance port in two positions: in "D" position the sample beam is at normal incidence, so any specular component of the reflection is reflected back through the transmission port and is deflected by the angled lens, preventing re-entry into the sphere; in 'S' position, the angle is 3° 20 min. The specular component will hit the sphere wall and be diffused within the sphere. The total reflectance will then be measured.

A polarizer can also be placed before mirror `M1` in order to take measures only with s/p-polarized incident light.

With this accessory, the cary internal sensor array is not used. Instead, PMT and PbS photocell sensors are located on the top of integrating sphere and receive light from it through two dedicated ports.

INSTRUMENT SPECIFICATIONS The following table 3 summarizes the instrument specifications (Abs = absorbance units):

Wavelength range	$175 - 3300\mathrm{nm}$
Light source	UV (190 to 380nm): D_2 lamp, VIS-NIR (380 to 3300nm): *W* halogen with quartz window
Monochromator	Double out-of-plane Littrow monochromator
Grating	Dual-sided, 70 x 45 mm, UV-VIS: 1200 lines/mm blazed at 250nm, NIR: 300 lines/mm blazed at 1192nm
Beam splitting system	Chopper 30Hz
Detectors	UV-VIS: R928 PMT, NIR: Cooled PbS photocell
Resolution ($\Delta\lambda$)	UV-VIS: $< 0.05\mathrm{nm}$, NIR: $< 0.2\mathrm{nm}$
Wavelength reproducibility	UV-VIS: $< 0.025\mathrm{nm}$, NIR: $< 0.1\mathrm{nm}$
Wavelength accuracy	UV-VIS: $\pm 0.1\mathrm{nm}$, NIR: $< 0.4\mathrm{nm}$
Photometric accuracy	$3 \cdot 10^{-4}$Abs at 0.3Abs
Photometric reproducibility	$< 8 \cdot 10^{-4}$Abs at 1Abs
Photometric noise	$5 \cdot 10^{-5}$Abs at 1Abs
Baseline flatness	$\pm 1 \cdot 10^{-3}$Abs
Beam separation	190.5mm
Compartment size	160(*W*) x 433(D) x 221(H)mm
DRA sample port	16mm diameter
Spectral bandwidth	UV-VIS: 0.01nm to 5.00nm, 0.01nm steps, NIR: 0.04nm to 20nm
Maximum scan rate	UV-VIS: 2000 nm/min, NIR: 8000 nm/min

Table 3: Cary 5000 technical specifications (extract from [Var02]).

AUTOMATIC INSTRUMENT RECONFIGURATION At certain wavelengths, the instrument configuration (gratings, lamps) is automatically changed by software, in order to guarantee the best configuration for the current working spectra. The following wavelengths determine a change in instrument configuration:

First lamp change (350nm) can be software edited

- $\sim$ 350nm-up: the D_2 light source is replaced by the Halogen lamp.
- 800nm-up: the PMT tube is replaced by the PbS detector and the 250nm-blazed grating changes to the 1192nm-blazed one. In addition, a filter is inserted to reduce NIR stray light.

4.3 EUV SPECTROPHOTOMETRIC FACILITY

The EUV normal incidence facility built at LUXOR laboratories is designed to perform reflectivity measurements in the 30-500nm wavelength range. In the lower part of this range, called Vacuum-UltraViolet

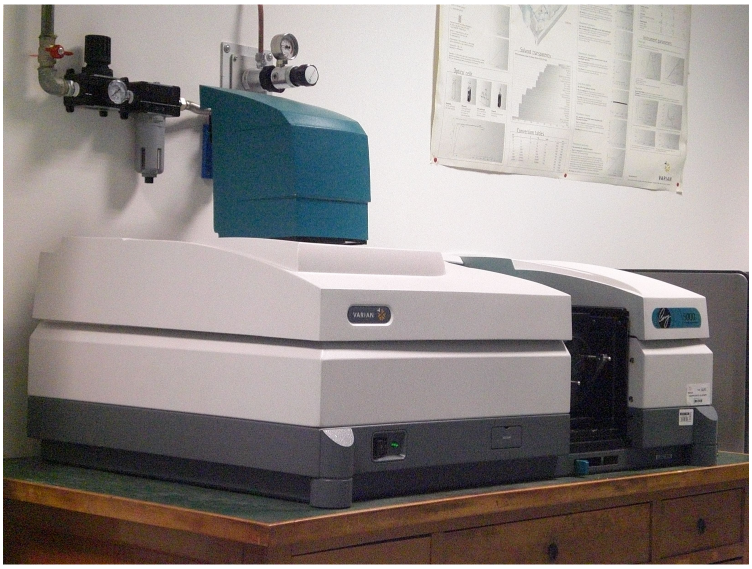

Figure 39: Cary 5000 available at Luxor, with opened compartment.

(VUV), light absorption is so high to impose the generation of high vacuum ($\sim 10^{-6}$mbar) through the lightpath.
The overall structure of the facility is similar to a spectrophotometer: a beam coming from a chosen light source is spectrally filtered by a monochromator and directed to the sample. The reflected intensity is then measured with a channel electronmultiplier.
In this application, the needed performance of the optical components allowed their use in nearly-normal incidence configuration.

Vacuum needed for far-UV measurements

Plane grating monochromators (PGMs) have often a large scanning range and good resolutions. However, the cascade of three reflective components as in Czerny-Turner configurations, leads to high losses at low wavelengths. Instead, toroidal gratings directly focuses the image of the input slit onto the output slit, with no need for collimation and refocusing mirrors. A single reflection is present, and thus the efficiency of the monochromator strongly increases. Moreover, toroidal (even holographic) gratings can be used to minimize aberrations like astigmatism [Pal05], that critically affect resolution and efficiency of the device.

Advantages of toroidal gratings

JOHNSON-ONAKA MONOCHROMATOR The main component of the EUV facility is a *Johnson-Onaka* monochromator [Mon09]. The grating used is toroidal, with $R = 0.5\text{m}$ curvature radius, ruled with 600 lines/mm and coated with a Platinum layer. This grating has the property that an input image is diffracted and refocused on the output slit if both lie on a precise circle, whose diameter is on the grating axis and radius $R_c = \frac{R}{2}$. Fulfilling this condition, called *Rowland's condition*, means maximizing the resolving power of the system.

Rowland's circle is the locus of Rowland's condition

As both the source and the sample compartment can't be moved, the grating will be used in a *fixed-deviation* monochromator [Pal05], as the deviation angle between the input and output beams is fixed $2\kappa = 25°$. A widely used fixed-deviation setup is the *Seya-Namioka* configuration, in which the only moving part is the grating, placed on a rotating mount and scanning the light spectrum. Resolution may be quite good in part of the spectrum, though it degrades (defocus) farther from the optimal wavelength, as long as the slits move from the Rowland's circle that rolls jointly with the grating.

Johnson-Onaka working principle

A more complex rotating mechanism can overcome this problem, allowing the grating to be not only rotated, but also translated on a circumference centered in a point C external to the Rowland's circle, thus maintaining the centre of grating surface on the bisector of the deviation angle while moving. This is the previously called Johnson-Onaka configuration, and minimizes the issues of a rotated only mirror.

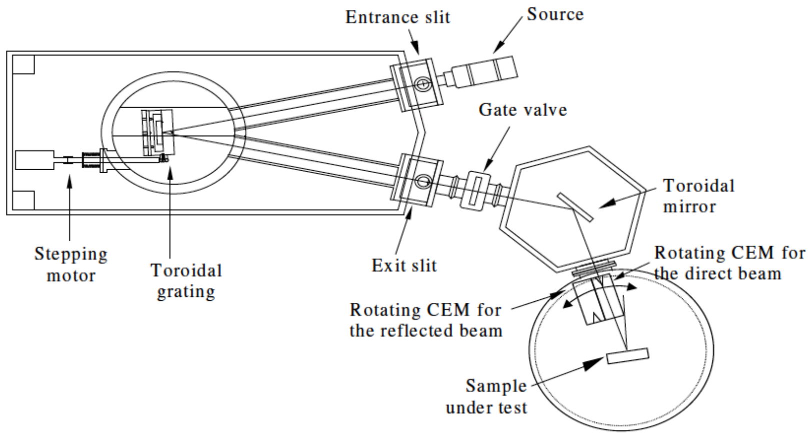

Figure 40: EUV facility design structure (source: [Mon09]).

EUV facility components

The components of the EUV facility, with reference to figure 40, are:

- *light source*: several types of light sources can be connected to an aluminium flange that contains also the entrance slit. For these measurements, a Deuterium and a Hollow Cathode lamps were used.

- *entrance slit*: the width of this slit controls the size of input image (and so the extended source effects) and the input power. The slit width can be adjusted between $0 \div 650\mu m$ whereas its height is fixed to $3mm$. It is located at the right distance on the Rowland circle:

$$r = R \sin\gamma \approx 48.8cm \tag{4.19}$$

- *grating*: the toroidal grating in the Johnson-Onaka configuration is enclosed in a circular steel chamber connected with the entrance end exit slit with two steel pipes. A stepping servo mechanism moves the grating on the right trajectory. The first order diffraction ($m = 1$) is used.

- *exit slit*: a slit identical to the one at the entrance is located at the same distance onto the rowland circle.
- *mirror*: a Pt-coated toroidal mirror, located in a hexagonal chamber, is used to refocus the diffracted beam exiting from the slit in the centre of the successive sampling chamber.
- *sampling chamber*: another circular steel chamber is designed to contain the measuring sample. A sample holder maintains it in vertical position, and allows it to move in polar cohordinates. The tilt angle θ is controlled manually by a rotating graduated mechanism, whereas an endless-screw motorized guide alters the distance from the chamber centre ρ. On the cover, a rotating arm can hold a detector that can be aligned with the reflected beam. The flange connecting this chamber to the previous one can be untightened to reconnect the chamber tilted at 90° to take measurements with different orientation.

The cascade of optical components induce a certain degree of polarization on the output radiation, which is normally absent in the source light. A method based on up/down-orientation measurements will be used to eliminate the influence of this factor. This is a *single beam* instrument, as only the reflected beam is measured. Zero correction is done measuring direct light twice for each measure. Variable angle measurements can be taken, differently from the Cary 5000 equipped with DRA.

Single-beam measurement

VACUUM SYSTEM The whole system is vacuum-proof. O-rings are inserted in every juncture and rotating shaft. The exit slit can cause a differential pressure between the monochromator chamber and the sampling section, for that reason two independent vacuum systems are connected to them, through the bottom of the circular chambers. This allows also to minimize contamination while using unsealed lamps. The two-stage vacuum system is made up of the following components:

Vacuum system components

- *gate valve* `G1`: this valve insulates the monochromator side from the sampling side of the machine, allowing to employ two independent vacuum systems.
- *choke vacuum valves* (`V3, V4, V5, V6`): these valves insulate various stages of the pumping system from the chambers. The valve couple `V3, V4` insulates a scroll pump from the chambers, whereas the couple `V5, V6` insulates the same scroll and a diaphragm pump from the back of two turbo pumps. This switching system allows to use the pumps firstly to create low-vacuum in the system, and then as backing pumps for the turbos.
- *slide valves* (`V1, V2`): the slide valves insulate the turbo pumps from the respective chambers, to allow inserting them in the system only when low-vacuum condition is reached.

- *turbomolecular pumps* (`P1, P2`): these pumps allow to reach high-vacuum ($\sim 10^{-6}$mbar), but must be started only when low-vacuum ($\sim 10^{-3\div 1}$mbar) condition has been reached, and must be back-pumped to mantain low differential pressure through them. Basically, they are made of many high-precision turbine stages on a shaft suspended by low friction bearings, which is made to spin up to 90000rpm by a air/water-cooled brushless motor.
- *scroll pump* (`P3`): This pump is used to pump from the monochromator and sample chamber and to back-pump from its turbo pump. Inside it, two eccentric spiral rotors create a moving chamber that continuously draw air from its input to the atmosphere.
- *diaphragm pump* (`P4`): This pump is used as the prior one, but for for the sampling chamber, except that it is slower. Like the previous one, it has no limitations on differential pressure, but it can decrease pressure only down to low-vacuum.
- *choke reentry valves* (`V7, V8`): These valves are used to inject Nitrogen (N_2) gas into the chambers in order to return to ambient pressure to open the instrument compartments.

Many components (above all the turbo pumps) are really sensitive to both absolute and differential pressure. For that reason the pressure inside the instrument is continuously monitored by the following gauges:

Vacuum monitoring with electronic gauges

- *Pirani gauges* (`S1, S2, S3, S4`): the first couple `S1, S2` is used to monitor the pressure of the two main pumps, to ensure the correct back-pumping of the turbos. The second couple `S3, S4` instead monitors the chamber pressure. The measurement is performed through the variation of resistance of a Pt filament put at the chamber pressure. Collision of the gas molecules with the filament (whose frequency depends on pressure) cause a weak heating of the filament, altering its conductivity, which is precisely measured. This system is limited to work only down to low-vacuum conditions.
- *Inverted Magnetron gauges* (`S5, S6`): These gauges can correctly measure high-vacuum pressures, and are used to monitor instrument chambers when the other gauges are out-of-range. Inside it, the few remaining gas molecules are ionized by a magnetron accelerator [AVT10]. The discharge current measured between the anode and the cathode of the device is dependent on the population of molecules. This device has the unwanted effect to emit light radiation and electrons, and must be switched off during measurements.

Vacuum stability must also be ensured to grant the accuracy of the measurement process.

Hot-cathode discharge lamp

DEUTERIUM LAMP A *Deuterium lamp* (L2D2) is a gas-discharge lamp filled with Deuterium gas (D_2). A heated Tungsten filament is used as hot cathode and is placed together with an anode into a nickel structure. The filament spontaneous emission ionizes the gas and lowers

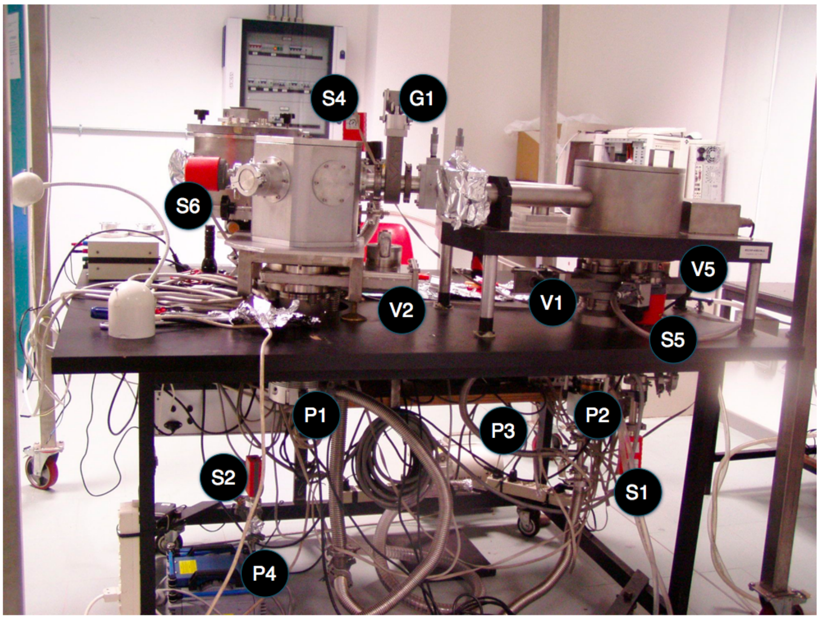

Figure 41: EUV facility photo with highlighted some components of the vacuum system.

the arc ignition voltage to $350 \div 400V$. This voltage is applied to the anode by a custom power supply. When the arc is ignited, the voltage drop across it goes down to $\sim 80V$ and the power supply switches to constant-current mode and sustains the arc with 300mA current.

Electrical characteristics

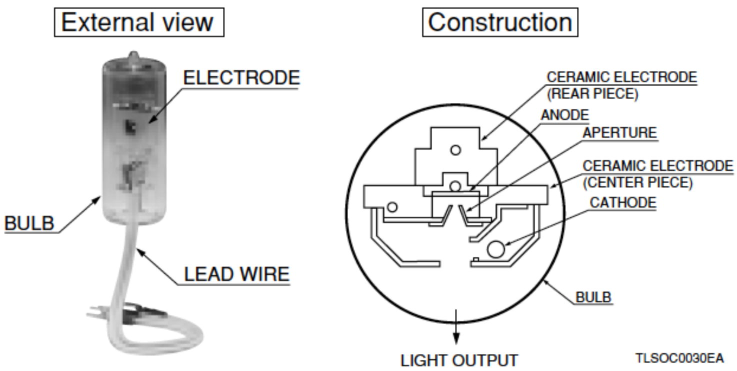

Figure 42: Structure of an L2D2 lamp (source: Hamamatsu Photonics K.K.).

The arc current excites the molecules of deuterium that emits thanks to the energy gaps of their rotational and vibrational excited states, rather than electronic states. This gives a wide spectrum from 112 to 900nm. The metal structure is designed to have a directive light emission. As shown in picture 43, the emission line of interest is at 121.6nm, where the spectrum has a considerable energy fraction (as said before,

Spectral characteristics

if the energy spectral density is not sufficiently high in the band of interest, the monochromator would waste the whole lamp power). The lamp, model L7293 by Hamamatsu Photonics K.K. [Ham05], is sealed in a UV glass bulb, that has the double function of being low absorptive with UV radiation and allowing thermal dissipation.

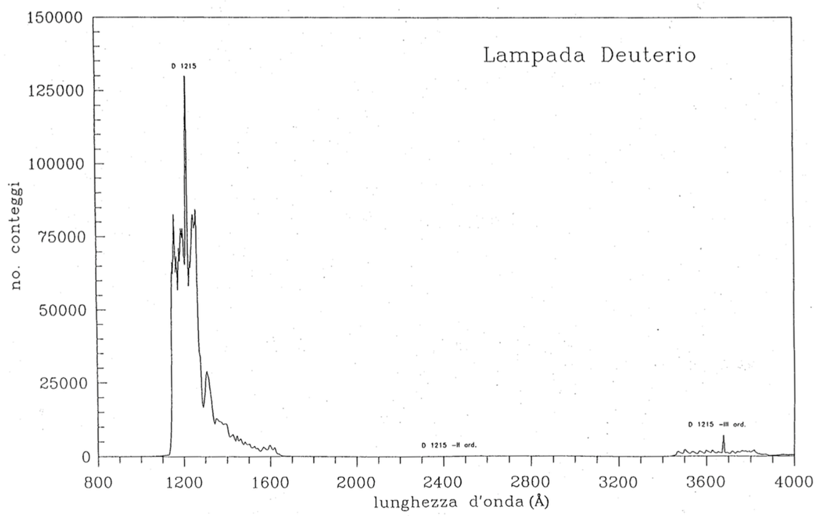

Figure 43: L2D2 lamp emission spectum.

HOLLOW CATHODE LAMP A *hollow cathode lamp* (HCL) is a cold-cathode gas discharge lamp widely used in spectroscopy. It has a more complex structure than a conventional discharge lamp, but the main difference is that the cathode is a conical cavity, which allows to obtain a particular plasma shape, cylindrical and aligned with the optical axis. In this layout the emission is directed towards the aperture without obstructing components. The system is filled with low pressure (~ 0.5mbar) Helium gas (although many other gases can be used as *buffer gas*) and the arc is sustained by a constant $\sim 200 \div 400$V power supply with ballast resistor, and the current is $100 \div 400$mA [Mon09].

Electrical characteristics

The lamp used was designed at Luxor laboratories and is showed in figures 44, 45. As the lamp is designed to reach wavelengths down to SXR range, the output window can not be glass sealed. The injected Helium gas then slowly diffuses towards the monochromator chamber, where it is drained by turbo pumps. The gas flow and pressure are precisely controlled by a *needle valve* and a Pirani gauge.

The emission spectrum, showed in figure 46, is used in its 58.4nm emission line.

CHANNEL ELECTRON MULTIPLIER The *Channel Electron Multiplier* (CEM) MD-501 supplied by Ampek, Inc. [Amp02] is the sensing element of this instrument. The working principle is the same of a PMT tube. A

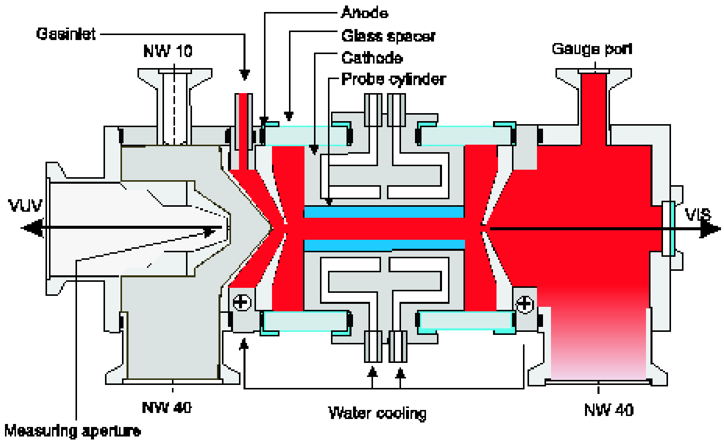

Figure 44: Layout of the hollow cathode lamp (source: [Mon09]).

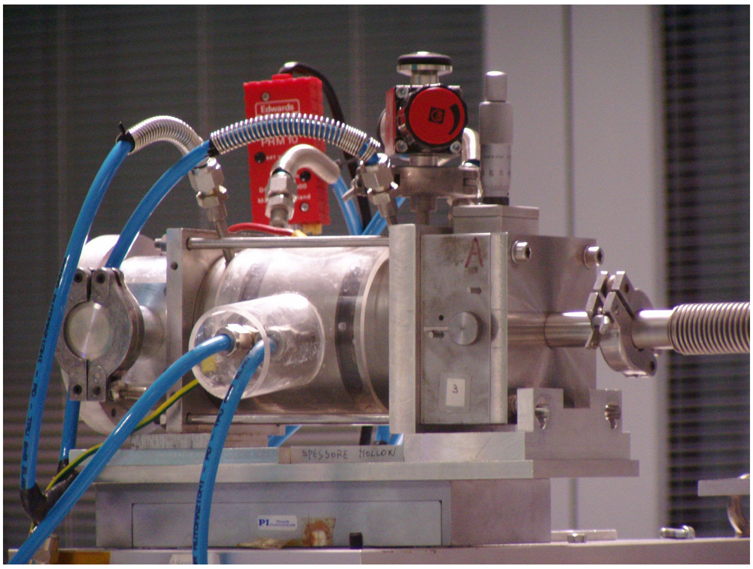

Figure 45: Photo of the hollow cathode lamp.

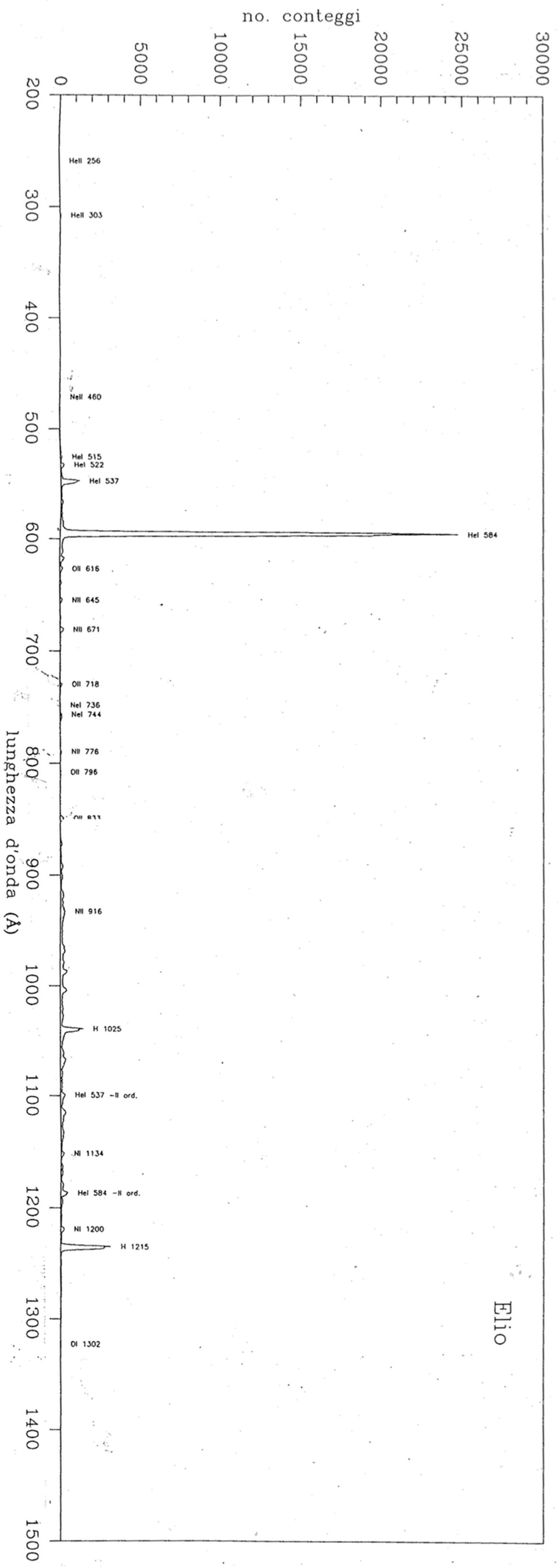

Figure 46: HCL lamp emission spectum.

semiconductive conical surface of 10mm diameter is hit by incoming particles, giving secondary emission. This allows to sense not only electrons (that are directly accelerated) but also ions, VUV light, SXR and many types of nuclear particles. The electron multiplier is constituted by a continuous dynode structure enveloped into a ceramic curved pipe, at the end of which a charge collecting plate is hit by multiplied electrons. Multiplication factor can reach values of 10^7.

Continuous electron multiplier device

As shown on diagram 47, the multiplier is installed in a metal housing together with a powering and signal conditioning system. The dynodes are polarized by a high voltage Cockroft-Walton generator, and the signal is detected by a charge-sensitive preamplifier. A TTL driver outputs a square wave with one low-hi transition for each photon count, up to 10^6 counts per second (cps) with a resolution of 250ns between pulses and a dark count inferior to 0.1cps. The entire device is powered with 12Vdc @ 30mA typ.

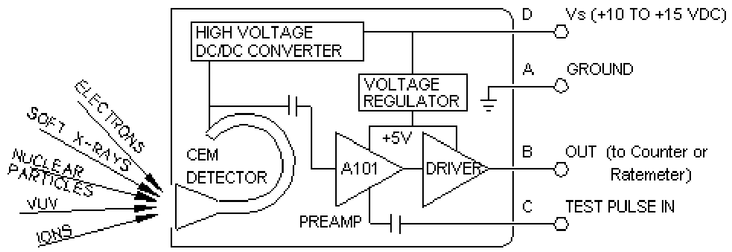

Figure 47: Functional diagram of the CEM detector (source: [Amp02]).

When operating the CEM, care must be taken to ensure that the device is powered on only in high-vacuum conditions, to avoid self-discharge through dynodes, and that the measuring beam hits the cone of the sensing element, to grant maximum and constant quantum efficiency in successive measurements. Efficiency against incoming photons is quantified by graph 48 in function of wavelength (of interest at 1216 and 608Å).

CEM operates in high-vacuum conditions only

INSTRUMENT SPECIFICATIONS The instrument operating performance, obtained from grating and CEM specifications, is here summarized. Table 4 also gives an estimation for many performance parameters calculated[2] here for $\lambda = 121.6\text{nm}$. The grating data are:

$$m = 1 \qquad a = 1.67\mu m \qquad N = 3 \cdot 10^4 \qquad \theta_i + \theta_m = 25° \tag{4.20}$$

The resolving power is then, from (4.15):

$$\mathcal{R} = mN = 3 \cdot 10^4 \qquad \Delta\lambda_{121} = \frac{\lambda}{\mathcal{R}} = 0.004\text{nm} \tag{4.21}$$

2 The formulas used are supposed to be valid approximately for non-plane gratings too; so results must be regarded as qualitative, also because many other contributes should be considered in this complex setup.

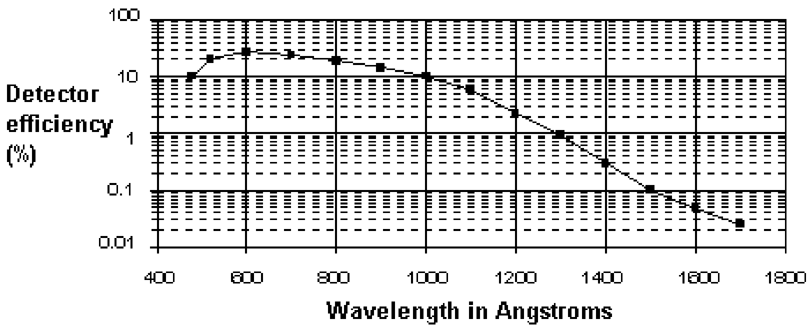

Figure 48: CEM quantum efficiency. (source: [Ampo2]).

the exit angle at the specified wavelength is, from (4.7), $\theta_i = 10.36°$ and $\theta_m = 14.64°$. The angular dispersion is given by (4.12):

$$\mathcal{D}_{121} = \frac{m}{a \cos \theta_m} = 618.9 \cdot 10^3 \tag{4.22}$$

Dispersion and Band at 121.6nm line

so that if the angle subtended by the full-opened exit slit at $d = 48.8cm$ is $\Delta\theta_s = 1.33 \cdot 10^{-3} rad$, the bandpass from (4.18) is:

$$\mathcal{B}_{121} = \frac{\Delta\theta_s}{\mathcal{D}_{121}} = 2.15nm \tag{4.23}$$

So the instrument band is adjustable between 0 and that value, with steps of ±0.0033nm (±1μm an the micrometric screw that opens the slit) and accuracy of ±0.004nm[3].

Wavelength range	$30 - 500nm$ (theoretical)
Light source	UV D_2 lamp, HCL, others available
Monochromator	Fixed deviation Johnson-Onaka, $2\kappa = 25°$
Grating	50x50mm, Toroidal blazed at 100nm, 600 lines/mm
Detector	Amptektron CEM
Resolution (R)	$3 \cdot 10^4$
Photometric accuracy	$1ppm$ on full-scale
Compartment diameter	$350mm$
DRA sample port	$16mm$ diameter
Spectral bandwidth	$0nm$ to 2.15 ± 0.004nm @ $121.6nm$, 0.0033nm steps

Table 4: EUV facility design specifications.

3 Often in case of lamps with line spectrum, the selected line is much narrower than instrument band, limiting the real output band.

4.4 ZYGO LASER INTERFEROMETER

Interferometry is a technique of measuring very short distances using the interference between two light beams. The high accuracy achievable (hundred times inferior to λ) made it the most used technology to perform surface profilometry and flatness measurements without contact.

In an interferometer, two spatially and temporally coherent light beams travel onto two different lightpaths, one of which involves the reflective surface (or the trasmissive medium) being measured. The interference is the result of the superimposition on a projective plane of the two beams after the paths. The interference is said to be constructive if the resulting intensity is higher than the intensity of the single beams, destructive in the opposite case. The intensity of two superimposed beams of planar waves of intensity I_0 is[4]:

Two-beams interference equation

$$I = 2I_0 (1 + \cos\varphi) \tag{4.24}$$

where φ is the phase delay corresponding to the OPD of the two paths:

$$\varphi = 2\pi \frac{nd}{\lambda_0} \tag{4.25}$$

The condition $\varphi = k\pi$ leads to totally constructive interference, whereas the destructive one happens at $\varphi = \frac{\pi}{2} + k\pi$.

FIZEAU INTERFEROMETER The Zygo GPI-XP used in these measurements is a Fizeau interferometer. The Fizeau interferometer exploits the interference laws previously described to measure distances and shapes.

Zygo interferometer working principle

A laser light source is spatially filtered by a microscope objective, that together with a collimating lens form a *beam expander*. In the middle of the expander is placed a beamsplitter. The expanded beam first of all encounters an optical slab which second face, of excellent flatness ($< \lambda/15$), reflects part of the beam backwards. This is called the *reference flat*. The transmitted beam reaches the reflective sample with normal incidence and is reflected too. While coming back into the system, the wavefronts interfere and are dumped by the beamsplitter and detected by a CCD camera.

Being the beam collimated, each single ray travels on an unique path linking each point of the sample with a point on the CCD sensor, thus forming an *interferogram*. The intensity of each point of the image depends on the OPD between the tho paths, that is the sum between the distance d_r between the sample and the reference flat (called the "*cavity*"), and e, the offset of the surface sample from the ideal flatness, both doubled. The phase delay can be obtained from (4.25):

Interferogram image

$$\varphi = 4\pi \frac{n(d_r + e)}{\lambda_0} \tag{4.26}$$

4 Here real quantities are considered because the media (air/vacuum) is known to be non-absorptive.

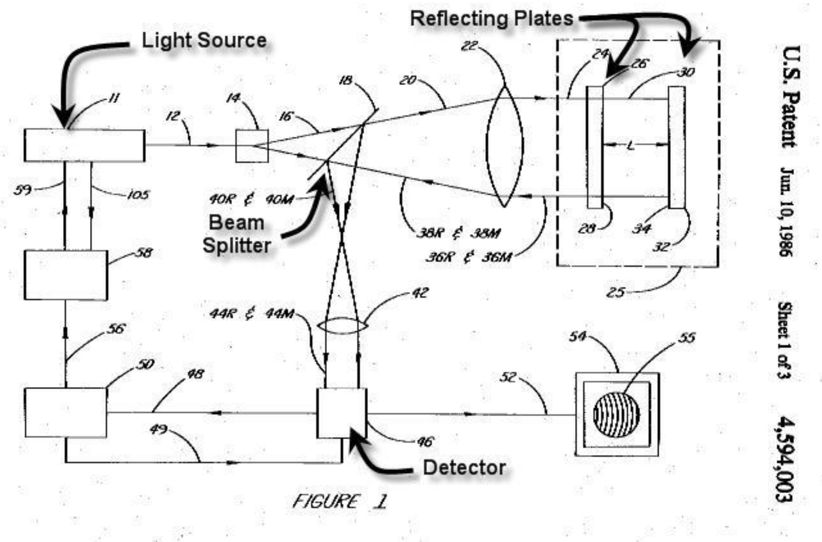

Figure 49: Fizeau interferometer described in an US patent (source: USPTO).

Where it is clear that for the periodicity of (4.24), the term d_s can be neglected if correctly chosen. Substituting the phase conditions for constructive:

$$2\pi\frac{nd}{\lambda_0} = \frac{\pi}{2} + k\pi \ \Rightarrow \ e = \frac{(2k+1)\lambda_0}{2n}, \ k \in \mathbb{Z} \tag{4.27}$$

and destructive interference:

$$2\pi\frac{nd}{\lambda_0} = k\pi \ \Rightarrow \ e = \frac{k\lambda_0}{n}, \ k \in \mathbb{Z} \tag{4.28}$$

This means that each time the surface offset changes of $\lambda/2$, the intensity goes from dark to bright. The interference image will have bright points aligned on the zones when the offset is odd multiple of $\lambda/2$, and bright points on the other case. Let the surface of the sample be continuous, those zones will be shaped like *lines of equal thickness*, called *Fizeau fringes*, along which the offset of the sample surface is equal.

Fizeau fringes

The analysis of the fringe shape and the integration of the fringe count determines the absolute offset of each point on the surface and giving a 2-D image of the surface shape.

PHASE-SHIFTING INTERFEROMETRY However, the precision of such a single measurement is limited inferiorly by $\lambda/2$, that is the minimum offset that can be accounted. Computer analysis can enhance accuracy by accounting even the intensity variation across the fringes and reversing equation (4.24) or performing Fourier analysis. However, digital image analysis is dramatically subject to factors like optical noise and lens aberration (astigmatism, coma, etc.) when precision goes increasing.

Analysis methods

An even better way to reach very high resolution (even $< \lambda/1000$) is using *phase shifting interferometry* (PSI). In this configuration [Wya00], the

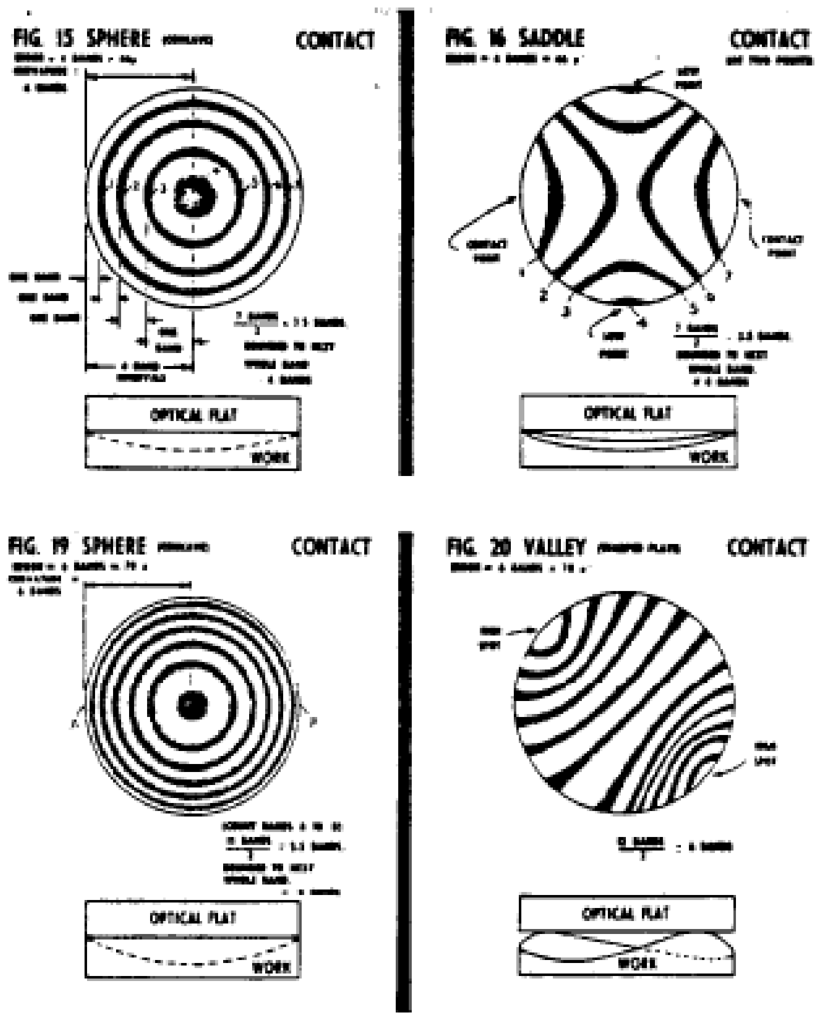

Figure 50: Example of Fizeau fringes caused by different surface deformations (source: [Wya09]).

reference flat is mounted on a piezoelectric transducer and is moved on many pre-defined steps (e.g. distant $\lambda/4$), while a photo of the interferogram is taken at each step. The cavity length d_r is altered and the initial phase too.

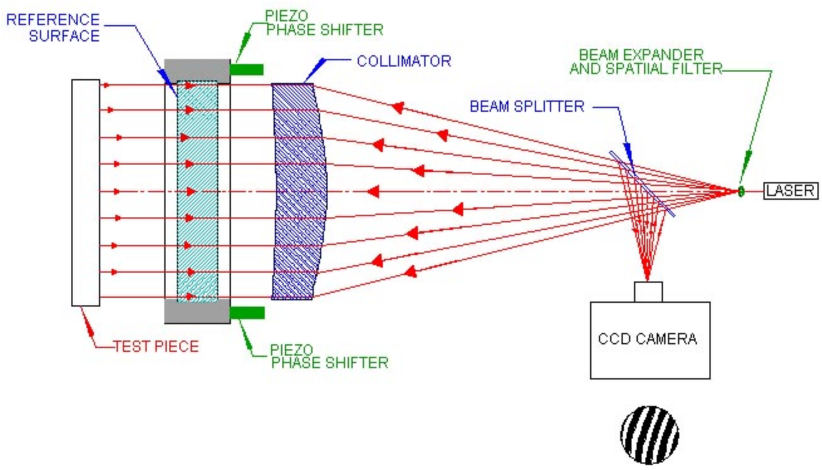

Figure 51: Fizeau phase-shifting interferometer setup (Graham Optical Systems).

To analyze the working principle we can denote the intensity of the interferogram punctually with $I_i(x, y)$, associated with the phase delay at each point $\varphi(x, y)$. Equation (4.24) can be modified to account initial phase φ_0:

$$I_i(x, y) = 2I_0(1 + \cos(\varphi(x, y) + \varphi_0(i)) \tag{4.29}$$

In a four-step measurement [Wya00], the initial phase takes four values $\varphi = 0 \ldots 3/2\pi$ and the intensities become:

$$I_1(x, y) = 2I_0(1 + \cos\varphi(x, y)) \qquad \varphi_0 = 0 \tag{4.30}$$

$$I_2(x, y) = 2I_0(1 - \sin\varphi(x, y)) \qquad \varphi_0 = \frac{\pi}{2} \tag{4.31}$$

$$I_3(x, y) = 2I_0(1 - \cos\varphi(x, y)) \qquad \varphi_0 = \pi \tag{4.32}$$

$$I_4(x, y) = 2I_0(1 + \sin\varphi(x, y)) \qquad \varphi_0 = \frac{3}{2}\pi \tag{4.33}$$

PSI algorithm equation

The combination of these four equations allows to express the phase delay:

$$\varphi(x, y) = \arctan\left(\frac{I_4(x, y) - I_2(x, y)}{I_1(x, y) - I_3(x, y)}\right) \tag{4.34}$$

and recover the offset of each point:

$$e(x, y) = \frac{\lambda_0}{4\pi n}\varphi(x, y) \tag{4.35}$$

Knowing the sign of sin(.) and cos(.), the tan(.) function is inverted modulo 2π, so the sign of offset is also detected (concave or convex deformation). Obviously, the $e(x, y)$ must be added with a 2π phase for each period to obtain absolute offset.

The main advantage of this technique is not only that the needed image processing is quite easy to implement, but also that the processing itself can reject many error sources such as non-uniform intensity or lens aberration.

The Zygo GPI-XP interferometer is available in the LUXOR Clean Room at DEI, Padova. The clean room is class M3.5 and is equipped with a M3.5 Newport optical bench over which the interferometer is mounted.

Zygo GPI-XP technical characteristics

The instrument is housed in a 30x30x70cm metal chassis firmly screwed on the bench top. The structure of the Zygo interferometer is showed in scheme 52. The light source used is a Class II HeNe red laser ($\lambda = 632.8nm$), and the detector is a 640x480px 8-bit b/w CCD camera, which is able to distinguish up to 180 fringes in the image. Two optical channels can be seen, one for the interferometric measures, the other is a viewfinder to precisely align the sample on the optical axis of the instrument (autocollimator). A zooming system is available to enhance resolution on a far sample and a $\lambda/4$ waveplate outputs circular polarization. The viewfinder system is connected to a dedicated display, and the whole instrument is controlled by a Windows® NT4.0 PC. The acquisition process is managed by software, and can be performed with 7 steps (instead of the 4 previously considered) or even 13 steps, giving higher resolution.
Many types of mounts and micrometric guides are available to hold the samples.

Many error sources can affect the measurement, such as incorrect phase shift, detector nonlinearity, intensity fluctuations and quantization error. Vibration is however the only error source not controlled by the instrument implementation. In fact, vibration of the sample holder or of the instrument chassis can alter the phase shift precision. For that reason the optical bench must suppress vibrations with frequencies from 1 to 120Hz (as specified by manufacturer [LOT10]) and must not be touched during data acquisition. Controlled temperature is also fundamental to maintain constant accuracy.

Vibration sensitivity

FILTER ACCESSORY The Zygo GPI-XP can be equipped with accessories [ZYG10], many of which are dedicated to measure curve surfaces or trasmissive media. In these measurements an attenuation filter is used to avoid camera saturation and enhance the fringe contrast. In fact, with high reflective samples (>40%), the intensity of the measuring beam must be attenuated to match the intensity of the reference beam. The filter used is made to grant a wavefront distortion inferior to $\lambda/10$, of the same order of the reference flat, so will weakly affect the instrument accuracy.

Filter used to reduce sample reflectance

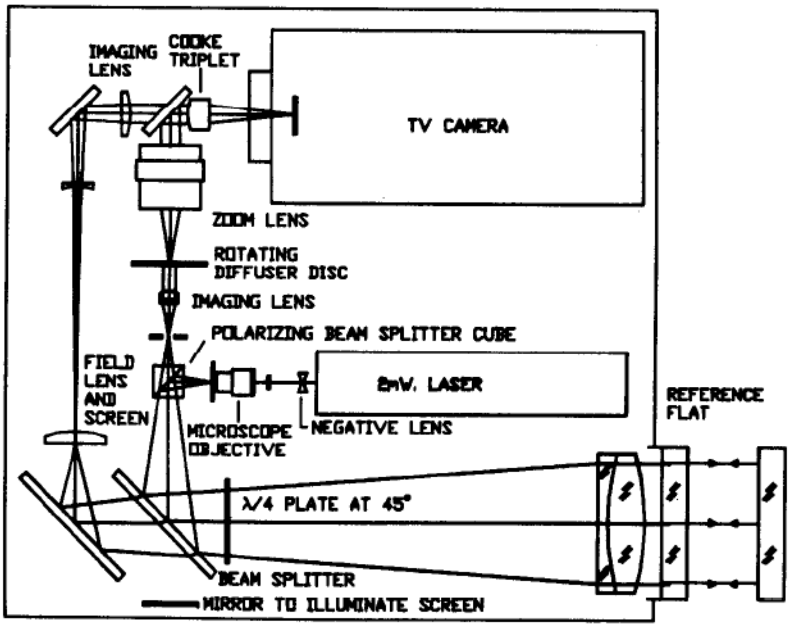

Figure 52: Diagram of the laser interferometer structure adopted by Zygo (source: Zygo Corp.).

Figure 53: Zygo filter accessory (source: [ZYG10]).

INSTRUMENT SPECIFICATIONS The following table 5 summarizes the instrument specifications, we note that the resolution is much higher than $\lambda/2$ obtained by fringe shape analysis.

Resolution is considered as best-case uncertainty

Measurement Technique	Laser-based, three-dimensional, optical phase-shifting interferometry
Test Beam Diameter	4 in (102mm)
Software	ZYGO MetroPro™
Dimensions	308x694x308mm
Spatial Sampling	640x480 pixels
Resolution	Better than $\lambda/8000$ (double pass)
Fringe Resolution	640x480: 180 fringes
Digitization	8 bits
Laser source	Class II < 1mW HeNe 632.8nm, > 100m coherence length

Table 5: Zygo GPI-XP technical specifications (source: [LOT10]).

Figure 54: Zygo GPI-XP installed at Luxor clean room.

5 MEASUREMENT PROCESS

CONTENTS

All the samples were tested both in VIS and UV bands to measure reflectivity performance. The measurement process has been improved during the work in order to minimize the risk of systematic errors (sample misalignment) or random errors due to the variations of the optical properties of the instruments (thermal variations, light source fluctuation, etc.). The flatness of the overall coating has then been tested with the laser interferometer.

Performed measurements in this work

In the following the measurement process will be explained, before exposing the obtained experimental data in next chapter.

5.1 VIS MEASUREMENTS

The VIS reflectance was tested with the Cary 5000 spectrophotometer in the range from 250 to 800nm. The sample was mounted on the DRA accessory with a harmonic steel clip coated with insulating tape, in order to reduce the risk of damaging the sample. For the same reason the samples were clipped on the edges rather than on the centre, to avoid mechanical stresses and induced deformation.

Sample mounting

The sample port of the DRA was 16mm diameter, exactly the size of the square samples. Unfortunately, some of the samples had defects on the border or were damaged, for this reason it was decided to reduce the surface under sampling only to the centre of the target, applying onto the sample port a black window made of insulating tape of 9x8mm size.

REFERENCE SAMPLE The *baseline intensity* for normalization was measured on a standard diffuser SPECTRALON® made by Labsphere, Inc. [Lab08]. The diffuser was certified to have a diffuse reflectance $R^D = 0.99 \pm 1\%$ over the whole visible spectrum.

Both the standard diffuser and the samples were pushed onto the black window externally. In this way the surface of the samples was at the same level of the window, to avoid differences induced during measurement by the reflected light trapped by the windows or sphere wall.

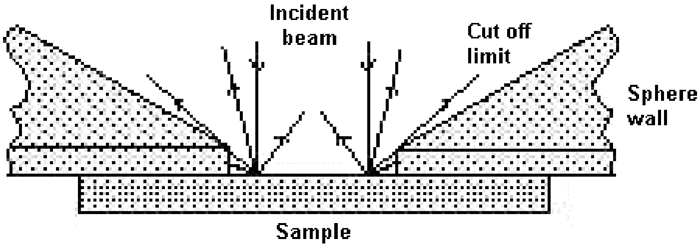

Figure 55: Light trap on the sphere wall (source: [Var10]).

PROCEDURE For each of the two sample batches (Score and Metis), the measurement procedure was the following:

1. Cary 5000 was powered on and let warm up for approx. 2 hours, to reach thermal stability of the optical components.
2. The Cary WinUV software was set up to scan from 400 to 800nm, using baseline correction (reflectance normalized to standard sample) and *reduced* beam size for DRA.
3. P-polarizer was inserted into DRA.
4. Integrating sphere was positioned in total reflectance "S" position.
5. Standard diffuser was fixed on DRA sample window and *BASELINE* data was acquired by software.
6. Samples were fixed on DRA window and for each of them total p-reflectance (R_p^T) data was acquired and normalized to baseline.
7. Integrating sphere was positioned in diffuse reflectance "D" position.
8. Standard diffuser was fixed on DRA sample window and *BASELINE* data was acquired by software.
9. Samples were fixed on DRA window and for each of them diffuse p-reflectance (R_p^D) data was acquired and normalized to baseline.
10. S-polarizer was inserted into DRA.
11. Integrating sphere was positioned in total reflectance "S" position.
12. Standard diffuser was fixed on DRA sample window and *BASELINE* data was acquired by software.

Particular care was taken to avoid altering the reference sample

13. Samples were fixed on DRA window and for each of them total s-reflectance (R_s^T) data was acquired and normalized to baseline.
14. Integrating sphere was positioned in diffuse reflectance "D" position.

15. Standard diffuser was fixed on DRA sample window and *BASELINE* data was acquired by software.

16. Samples were fixed on DRA window and for each of them diffuse s-reflectance (R_s^D) data was acquired and normalized to baseline.

17. All data was exported in CSV format and saved, the sample removed.

Data post-elaboration was done with MATLAB® also to draw the plots.
Specular reflectance was obtained by difference:

$$\mathcal{R}^S_{s/p} = \mathcal{R}^T_{s/p} - \mathcal{R}^D_{s/p} \tag{5.1}$$

then the overall reflectance was calculated from definition (3.18), and normalized to the known reflectance value of the standard reference sample $R_D = 0.99$:

$$\mathcal{R}^S = \frac{\mathcal{R}^S_s + \mathcal{R}^S_p}{2} \cdot \frac{1}{0.99} \tag{5.2}$$

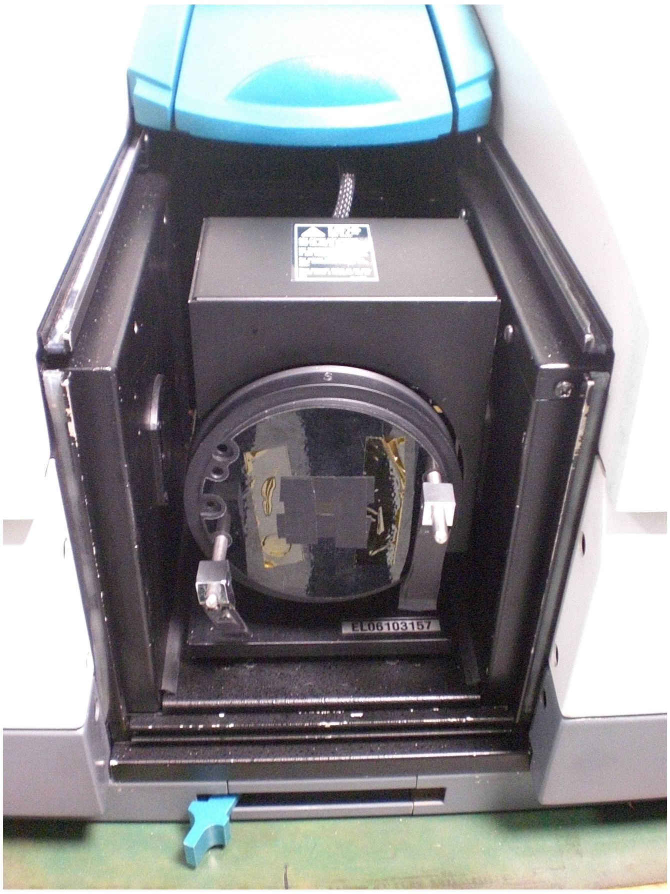

Figure 56: Cary 5000 DRA with tape window.

UNCERTAINTY The instrumental uncertainties are reported in absorbance units (Abs). The instrument, with DRA, measures the ratio between incoming and reflected light, that can be considered as total transmittance ($\mathcal{T}$) of the system. The relations between the two physical quantities are:

$$A_{[Abs]} = -\log_{10}\frac{I}{I_0} = -\log_{10}\mathcal{T} \qquad \mathcal{T} = 10^{-A_{[Abs]}} \tag{5.3}$$

the standard relative uncertainty on the transmittance σ_T depends from the uncertainty on the absorbance σ_A according to the error propagation formula:

$$\frac{\sigma_{\mathcal{T}}}{\mathcal{T}} = \sigma_A \ln 10 \tag{5.4}$$

Worst-case uncertainty was considered

The worst-case absorbance measured corresponds to 10% reflectivity, $A_{[Abs]} = -\log_{10} 0.1 = 1\text{Abs}$. With this value, the standard uncertainties have been extracted [Var02]:

1. *photometric accuracy*: $\sigma_1 = 1 \cdot 10^{-3}\text{Abs}$
2. *photometric reproducibility*: $\sigma_2 = 8 \cdot 10^{-4}\text{Abs}$
3. *photometric noise*: $\sigma_3 = 5 \cdot 10^{-5}\text{Abs}$
4. *baseline flatness*: $\sigma_4 = 1 \cdot 10^{-3}\text{Abs}$

and the overall uncertainty in [Abs] is given by their RMS mean:

$$\sigma_A = \sqrt{\sum_i \sigma_i^2} = 1.63 \cdot 10^{-3}\text{Abs} \tag{5.5}$$

Then relative uncertainty on transmittance can be obtained with equation (5.4):

$$\frac{\sigma_{\mathcal{T}}}{\mathcal{T}} = \sigma_A \ln 10 = 0.38\% \tag{5.6}$$

Reference sample tolerance critically affects uncertainty

which value must be RMS averaged with the 1% uncertainty of the reference sample:

$$\frac{\sigma_{\mathcal{R}}}{\mathcal{R}} = \sqrt{0.38^2 + 1^2} = 1.07\% \tag{5.7}$$

this value is considered for measurement data obtained.

5.2 UV MEASUREMENTS

The VIS reflectance was tested with the EUV normal incidence facility at Luxor. Being the EUV facility non software-operated, some precise manual work was needed to configure the machine and perform the measurement. In particular, care was took to the procedure for creating high-vacuum into the instrument without damaging pumps or mirrors and for aligning correctly the samples and the detector. The facility is designed to perform specular reflectance tests, so the analysis used in the previous section is no longer needed.

As the hollow cathode lamp has its main spectral line at 58.4nm, this wavelength will be used instead of the exact 60.8nm to probe the reflectance for the FEL application, giving nevertheless a good idea of the performance with an error of ~2nm.

POLARIZATION ISSUES Differently from the spectrophotometer, in the EUV facility no polarizer is present. The beam entering in the sample chamber is, although, partially polarized by the multiple reflections on the grating and on the refocusing mirror. The *polarization factor* is defined upon the intensity of p-polarized light I_p and s-polarized light I_s hitting the sample:

$$f = \frac{I_s - I_p}{I_s + I_p} \tag{5.8}$$

This factor is known to be $f = 0.89$ @ 121.6nm in this facility.
However, the sample chamber can be rotated 90° on the optical axis (up-down positions), thus inverting the s and p-polarized components. Taking a measurement in both position allows to calculate the overall reflectance, regardless the polarization factor. Let I_s and I_p the polarized source intensity components and I'_s and I'_p the reflected ones. The average of the two is:

Rejecting polarization issue with up-down measurements

$$\tilde{\mathcal{R}}^S = \frac{1}{2}\left(\frac{(I'_s + I'_p)_{up}}{(I_s + I_p)_{up}} + \frac{(I'_s + I'_p)_{down}}{(I_s + I_p)_{down}}\right) \tag{5.9}$$

Remembering that $I'_{s/p} = R_{s/p} I_{s/p}$ and that in the up position the incoming components are inverted:

$$\tilde{\mathcal{R}}^S = \frac{1}{2}\left(\frac{\mathcal{R}^S_s I_s + \mathcal{R}^S_p I_p}{I_s + I_p} + \frac{\mathcal{R}^S_s I_p + \mathcal{R}^S_p I_s}{I_p + I_s}\right) = \frac{\mathcal{R}^S_s + \mathcal{R}^S_p}{2} = \mathcal{R}^S \tag{5.10}$$

This proofs that the specular reflectivity value can be obtained by the average of the two measures. □

DETECTION A frequency counter was connected to the Amptektron CEM to count the number of detected photons in a given time. As the data elaboration contains only ratios between intensities, no conversion was needed, because photon count expressed in photons/sec (or photons/10sec) is directly proportional to beam power at a fixed wavelength:

Photon count is equivalent to power flux

$$I[W] = C[\text{photons/sec}] \cdot E_p[J] = C \cdot h\nu \tag{5.11}$$

All the measurements were taken in this way. Particular attention was paid to *optimize* the counter reading. In fact the maximum count is read when the beam hits the side of the input cone of the CEM, so that the angular position of the CEM was corrected each time to read the maximum possible value. The baseline for normalization was taken at the beginning and end of each measuring sample, with the beam directly hitting the CEM.

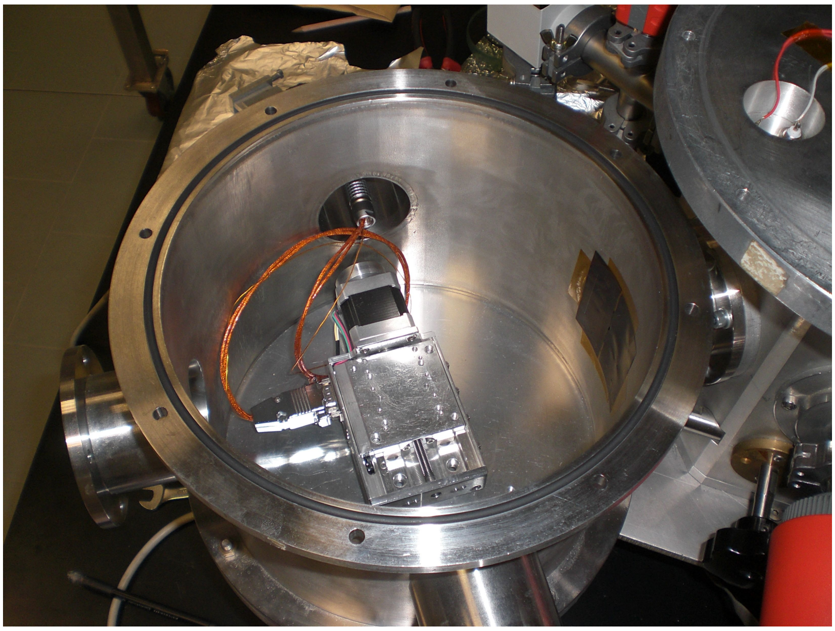

Figure 57: EUV measurement chamber with polar movement mechanism.

PROCEDURE For each sample, the measurement procedure was the following:

1. The lamp (L2D2 for 121.6nm, HCL for 58.4nm) was shut down and removed, then substituted by an Halogen visible lamp. The monochromator was set to zero order.

2. The sample was mounted on the holder and aligned with the beam.

3. A paper strip was taped on the CEM entrance. Then the measuring chamber was closed and tightened with screws to simulate the compression of the sealing rings due to high-vacuum. Then the beam was verified to hit correctly the CEM at whatever angle of incidence.

4. The spectral lamp was remounted.

5. The strip was removed and the entire system was put in low-vacuum (with gate and slide valves closed) with scroll and diaphragm pumps.

6. The system was put in high-vacuum with turbomolecular pumps opening the slide valves. Then also the gate valve was opened.

Turbo pumps started only after low vacuum was reached

7. The lamp was powered up and left idling for about 10 min.

8. The sample was moved away from the light beam, the direct beam intensity was measured and the photon count was reported as I_{d0}.

9. The sample was realigned with the beam and set to $\theta = 15°$ incidence angle. The CEM was aligned with the reflected beam and the count was reported as $I_{up}(\theta)$[1].
10. Other measures were took with 5° increment up to 70°.
11. The direct beam intensity was newly measured and reported as I_{d1}.
12. The system was brought to ambient pressure by N_2 filling.
13. The sample chamber was rotated to the down (vertical) position[2] and the measurement steps repeated until here. Data was reported as $I_{down}(\theta)$.
14. The sample chamber was rotated back to up (horizontal) position.

N_2 avoided chamber contamination

As a difference from the measures taken with Cary 5000, only two wavelengths were used for those samples (which were of major interest), but the test was performed at different incidence angles.

Direct beam intensity I_d was then obtained by averaging the two reads, in order to partially reject lamp fluctuations:

$$I_d = \frac{I_{d0} + I_{d1}}{2} \tag{5.12}$$

The reflectivity values were then calculated using (5.9):

$$\mathcal{R}^S(\theta) = \frac{\mathcal{R}^S_s(\theta) + \mathcal{R}^S_p(\theta)}{2} = \frac{I_{up}(\theta) + I_{down}(\theta)}{2I_d} \tag{5.13}$$

SAMPLE ALIGNMENT The sample beam passes very near the centre of the sample chamber. to ensure that the sample is fully hit by the beam even at high angles, the beam must hit in its exact centre, that must correspond to the centre of rotation of the same. To do this, two conditions must be fulfilled:

Precise alignment assured measurement reliability

- *backreflection*: the mirror's angle is corrected until the beam is returned back to its path. The θ incidence angle is then measured from this position. The beam is ensured to be hitting the centre of the sample.
- *graze*: the mirror is set to $\theta = 90°$. Its distance from chamber centre ρ is then adjusted until the beam is grazing to the surface of the mirror. This value of ρ is used when the sample is reset to the centre after the direct beam has been measured.

UNCERTAINTY The detector has a negligible accuracy with respect to the many other factors that affect the uncertainty of the measure. In fact, the fluctuation of the light source, the error committed in selecting the correct angle and the one in optimizing the count read are much higher and hardly quantifiable. However, an uncertainty of 5% is globally considered for these measures.

1 This measurement is said to be in "$\theta - 2\theta$" (*theta - two theta*) configuration
2 It is clear from the previous discussion that the two position are totally interchangeable, but are distinguished here for clarity.

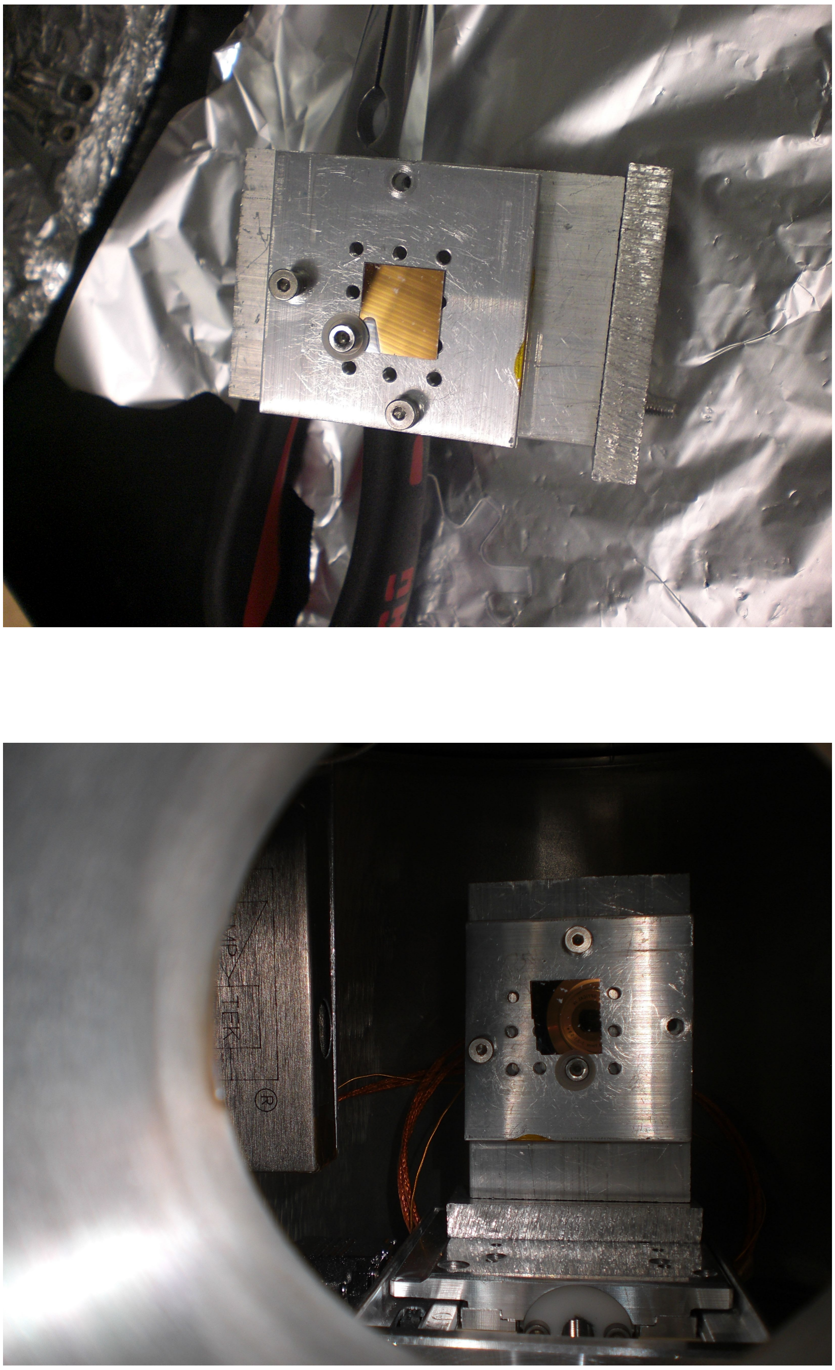

Figure 58: Sample mounted on the holder and into the chamber with the Amptektron CEM.

5.3 INTERFEROMETRIC ANALISYS

The analysis with the Zygo GPI-XP interferometer was performed only on one sample.
The sample was fixed on a post holder that allowed tip-tilt adjustment. Through the camera view, the sample was located in the centre of the field of view and then aligned with the viewfinder mode, to be exactly normal to the instrumental axis. The zoom value was then adjusted to enlarge the image of the sample as much as possible (to use the full available resolution).
At this point the interference fringes were visible on the instrument monitor. The alignment was adjusted to have the fringe centroid as close as possible to the centre of the sample (that minimized the number of fringes on the sides and improved precision).
Finally, with the PC application data acquisition was started and, at its end, data was exported[3].

Zoom until sample occupied the full camera field

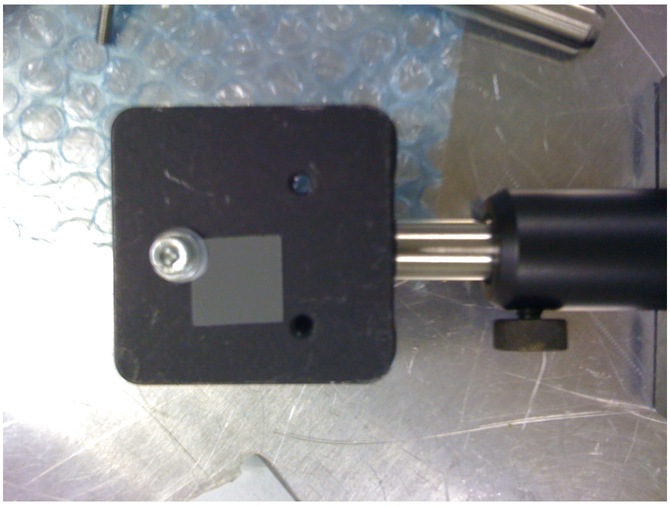

Figure 59: Sample mounted on the holder for the interferometric analysis.

UNCERTAINTY The instrumental uncertainty is considered equal to the reported resolution of $\lambda/8000$.

3 Software algorithm was set to automatically remove tip-tilt from data, so that the sample appeared aligned with its ideal plane

6 MEASUREMENT DATA

CONTENTS

The postprocessed data is contained in this chapter.
Where preceding data was available, actual values were compared with them. Measurements not performed in this work, but useful to the evaluation of the samples, are also included. These are Atomic Force Microscope (AFM) measurements and reflectance data obtained at 30.4 nm wavelength using the Synchrotron Light Source Facility at ELETTRA (Trieste).

WORK STATUS Unfortunately, as the measurement work is still in progress, not all data is available by now. Not all samples have been tested yet, and some of the samples tested in the EUV facility have been tested only in up-chamber position at 121nm wavelength.

PLOTS In every plot, solid lines represent interpolated measured data, whereas dashed lines represent uncertainty interval.

Brief plot legend

6.1 VIS MEASUREMENTS

The VIS measurements are plotted in the following, divided in the two sample batches.

SAMPLES FOR SCORE The first VIS measurement are on samples designed for Score. For these sample preceding data was available, taken on july 2006 on two spectral lines. The first reflectivity value is at 543nm (10° incidence) and the second at 632.8nm (6° incidence), both measured with HeNe laser sources[1].
The purpose of this data (showed as a black dash on the plots with error lines) is firstly to evaluate the performance loss of the samples

Preceding laser measurements

1 The incidence angle, although being different from that in the Cary 5000, can be neglected in the analysis, as for near and low incidence angles, the reflectivity values can be shown from Fresnel's equations not to vary significantly.

due to aging in storage conditions; and secondly to reveal any evident incoherence in the new data.

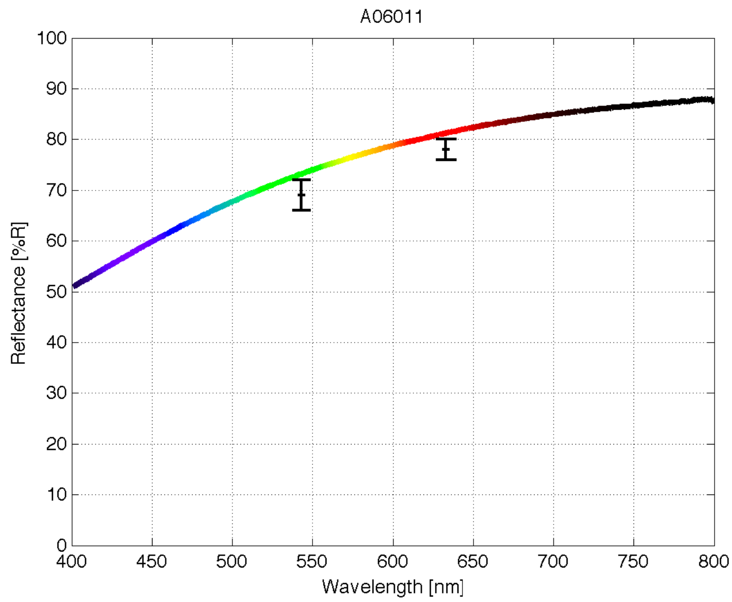

Figure 60: Sample A06011.

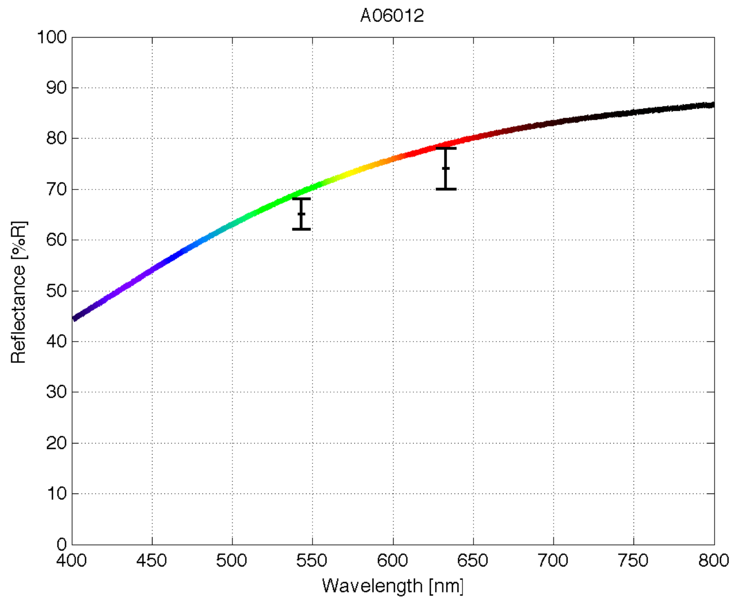

Figure 61: Sample A06012

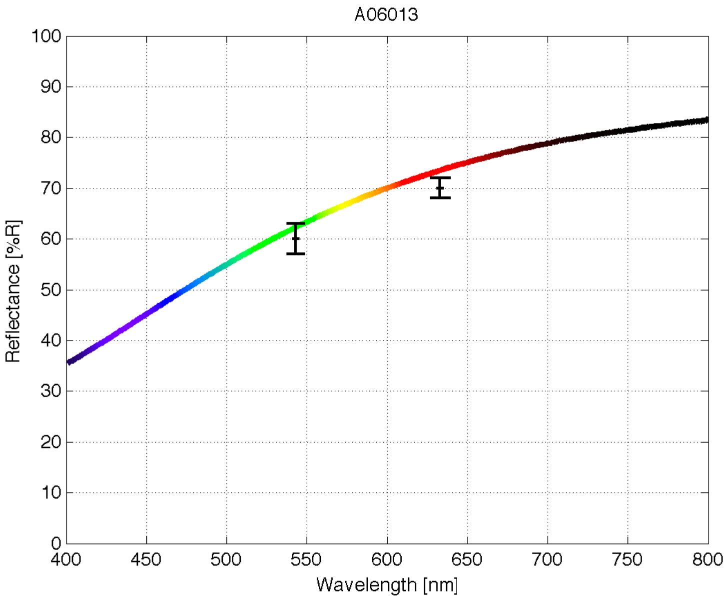

Figure 62: Sample A06013

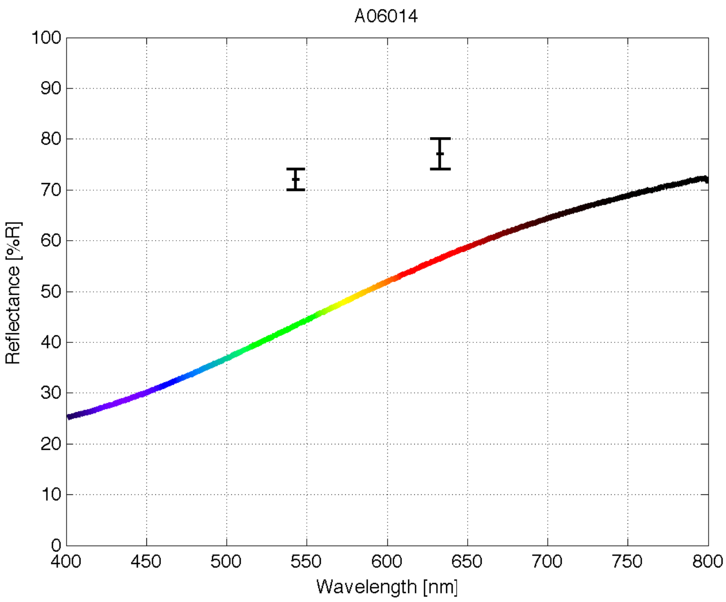

Figure 63: Sample A06014

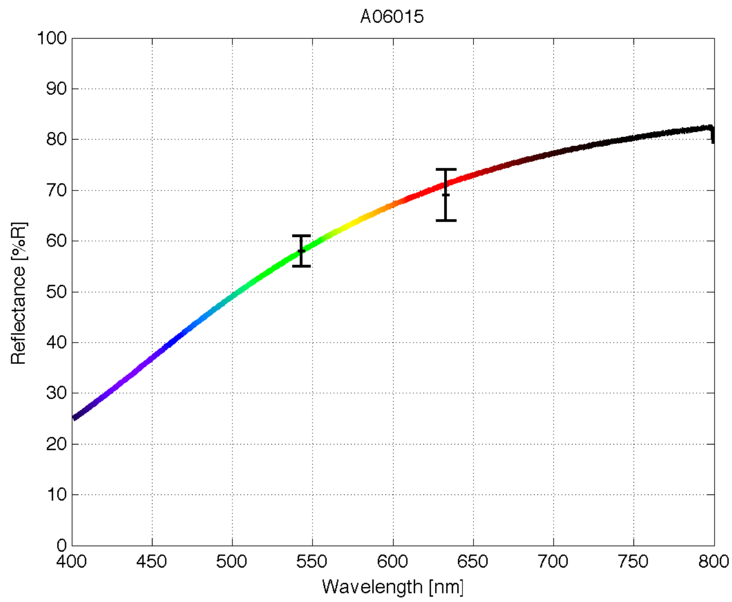

Figure 64: Sample A06015

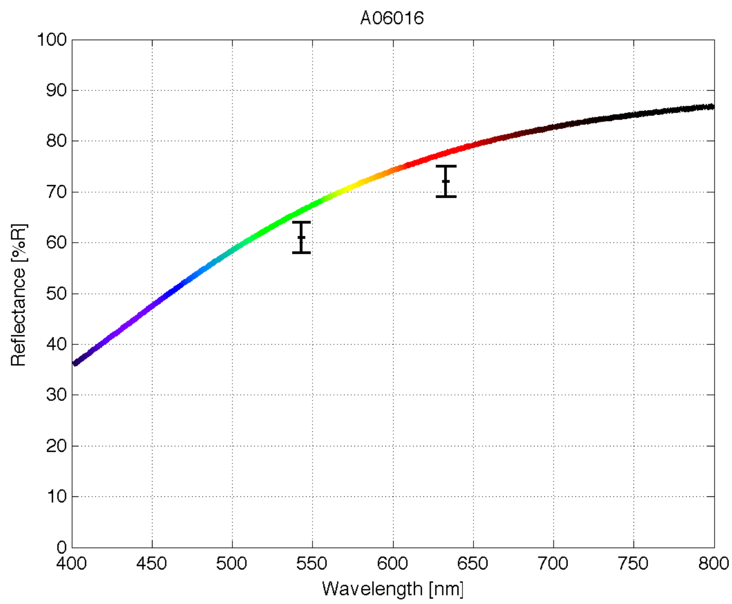

Figure 65: Sample A06016

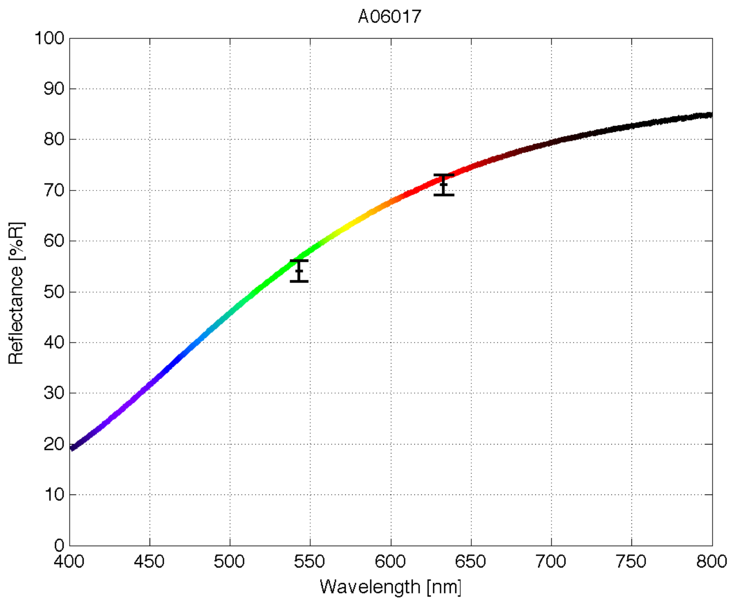

Figure 66: Sample A06017

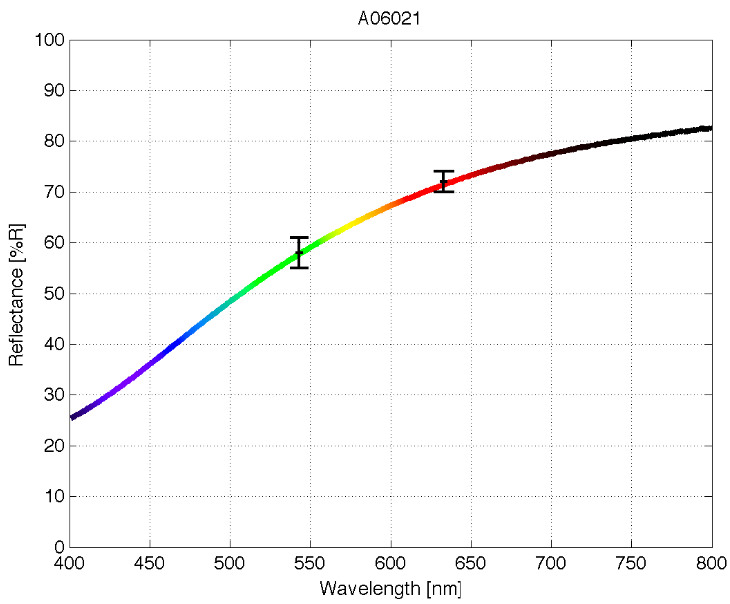

Figure 67: Sample A06021

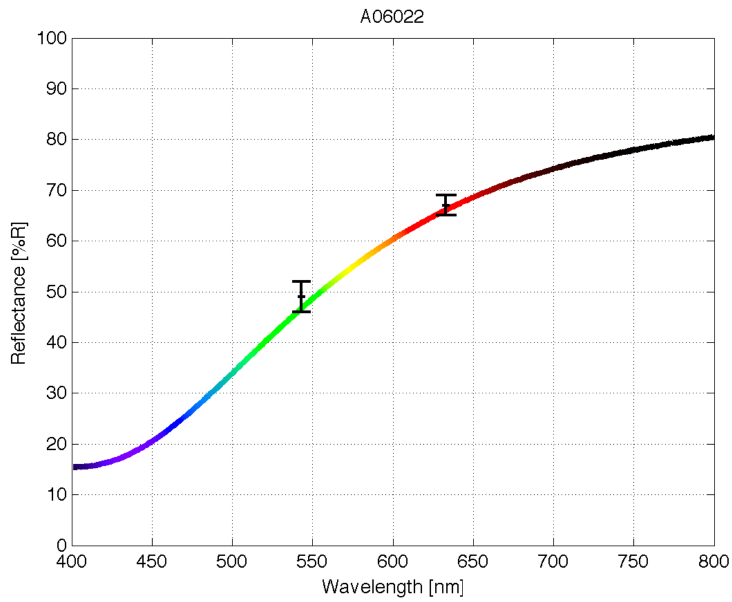

Figure 68: Sample A06022

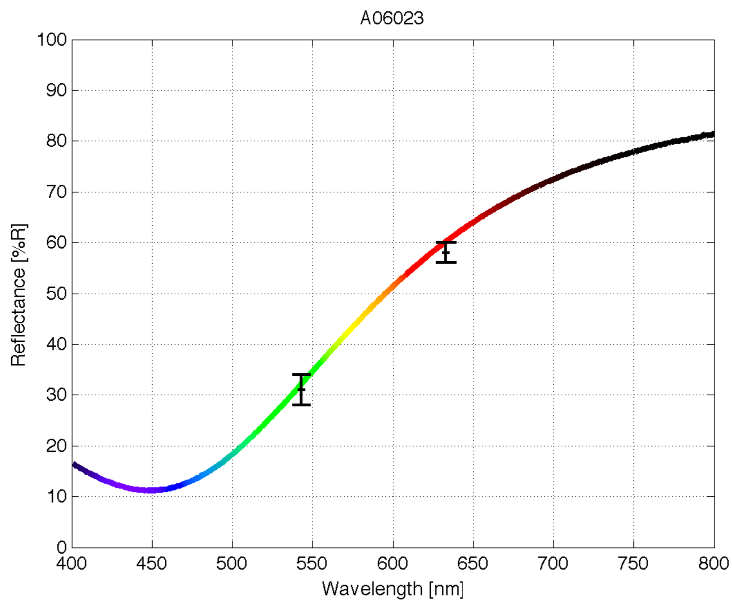

Figure 69: Sample A06023

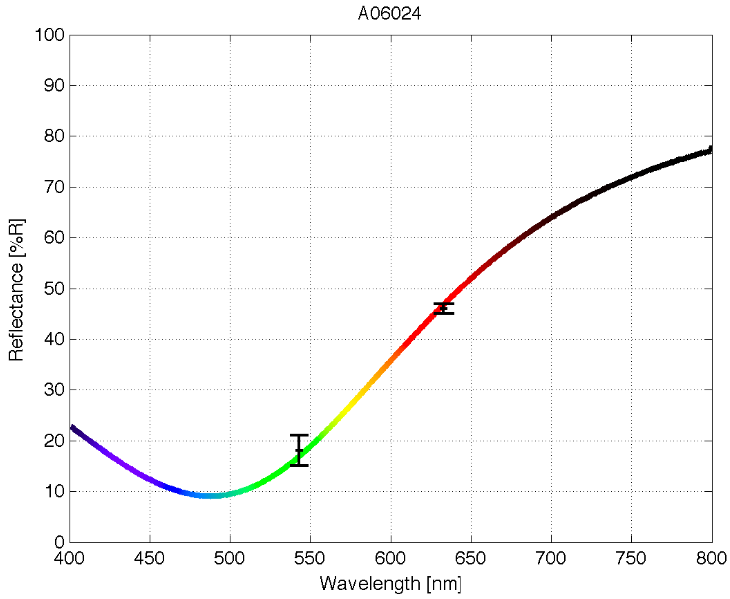

Figure 70: Sample A06024

Almost the whole A06011...A06017 series exhibits reflectance values compatible with preceding data, even if weakly exceeding. Among them are excepted A06014 and A06016 having, respectively, strongly lower and weakly higher values.
Data from samples A06021...A06024 is pratically unchanged from old measurements.

SAMPLES FOR METIS/FEL The main VIS measurements of this work were performed on new samples designed for Metis application. Obviously VIS band is used for space imaging applications, and is not relevant for FEL radiation filtering. Being the samples brand new, no preceding data is available.

First measurements on these samples

All films have a good reflectance. The highest optical performances are those of the Aluminum/Zirconium coating as of the high reflectivity of the former. Iridium capping-layers and Iridium multilayer film increase the reflectance respect on classical Mo/Si film while the Tungsten capping-layer doesn't bring substantial enhancements.

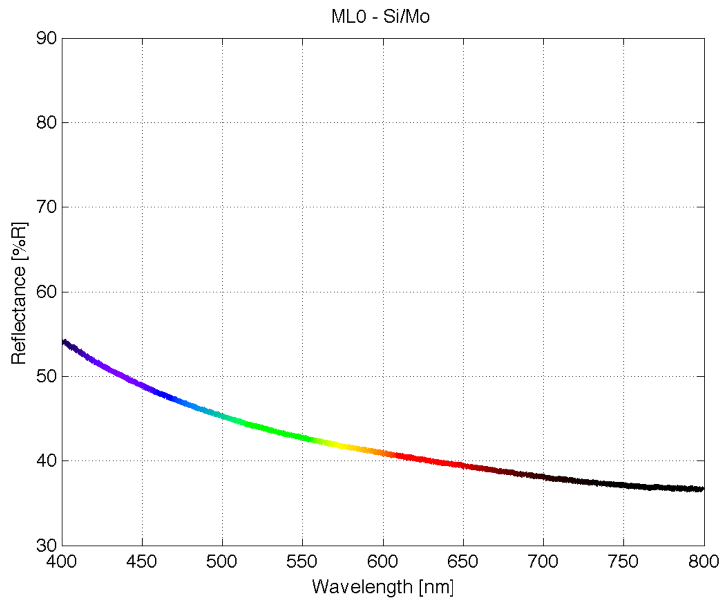

Figure 71: Sample ML0 - Si/Mo.

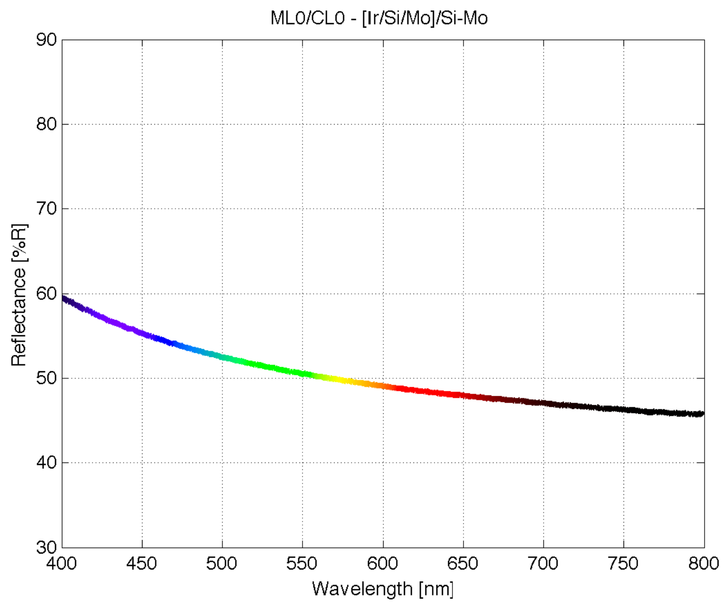

Figure 72: Sample ML0/CL0 - [Ir/Si/Mo]/Si-Mo.

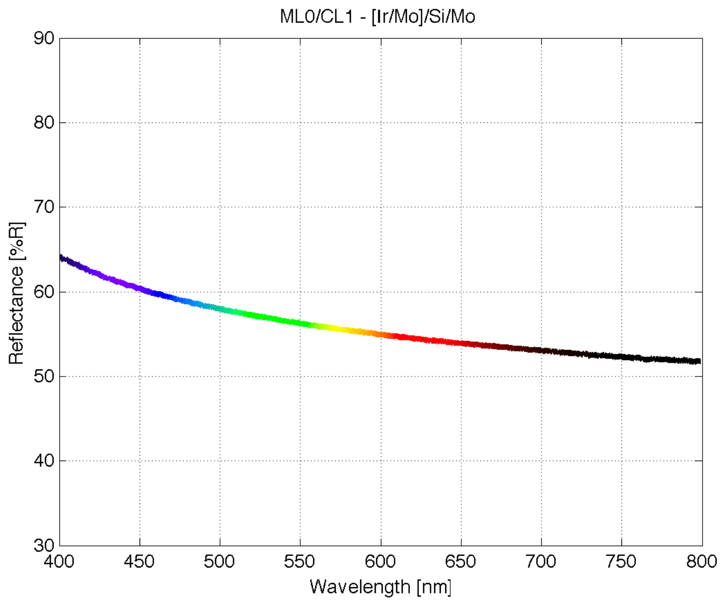

Figure 73: Sample ML0/CL1 - [Ir/Mo]/Si/Mo.

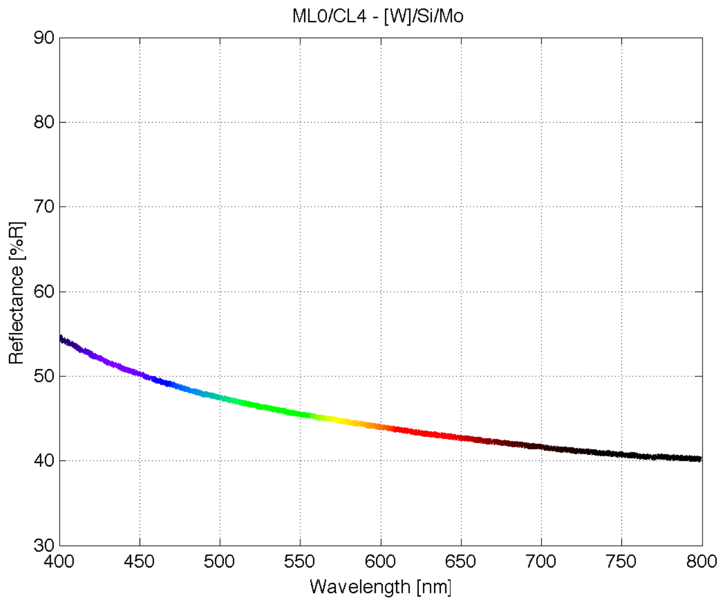

Figure 74: Sample ML0/CL4 - [W]/Si/Mo.

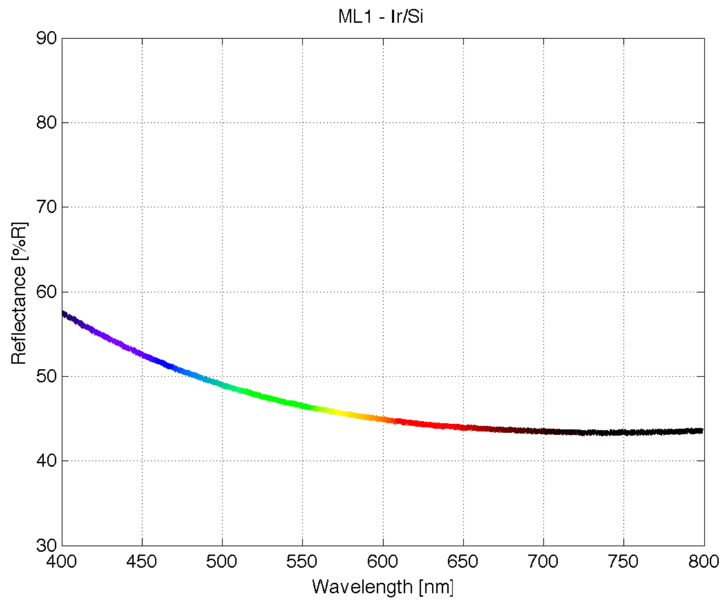

Figure 75: Sample ML1 - Ir/Si.

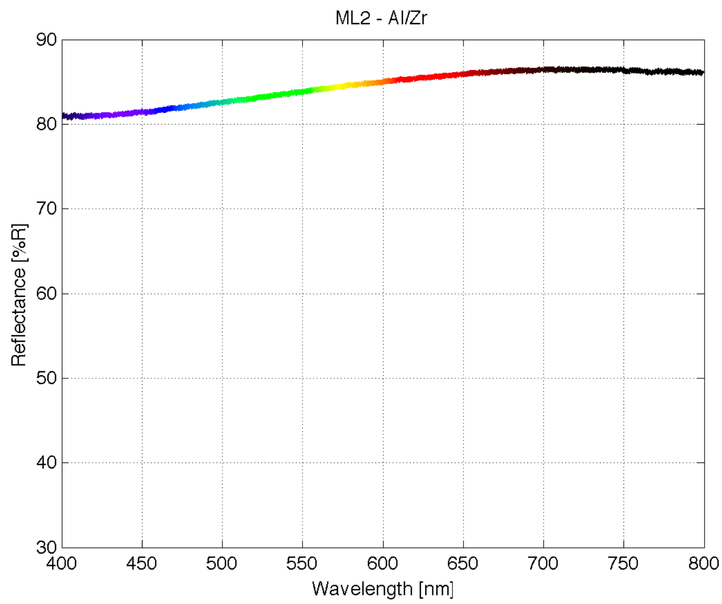

Figure 76: Sample ML2 - Al/Zr.

6.2 UV MEASUREMENTS @ 121.6NM

The first VIS measurement are on samples designed for Score. For these sample preceding data was available, taken on july 2006 with the same EUV facility, and reported with a thinner line on each plot. These measurements were taken with chamber-up configuration only, so the error from unpolarized reflectivity can be retained sistematic (although it is negligible for small angles). Nevertheless, also preceding data was taken in the same way, so data is clearly comparable.

SAMPLES FOR SCORE The measured data has the same trend of the preceding data, although presents a pseudo-constant difference of about $10 \div 20\%$. This error was firstly thought to be sistematic, such as a loss of part of direct beam caused by sample or CEM misalignment. To investigate this, a polished standard Silicon substrate has been tested, measuring a correct reflectance value of 43.2% @ $\theta = 10°$. This proved that the measured data is correct and all the samples incurred a reflectivity loss due to aging between $10 \div 20\%$ at every incidence angle.

Possible sistematic error investigated

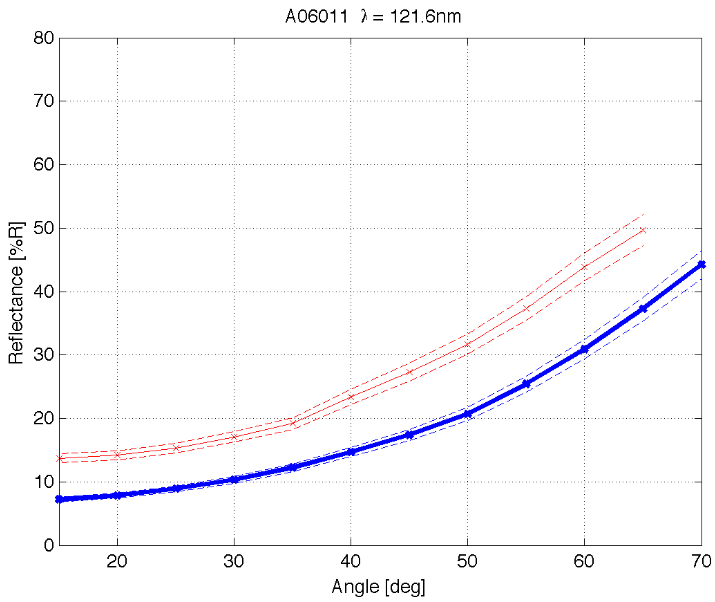

Figure 77: Sample A06011.

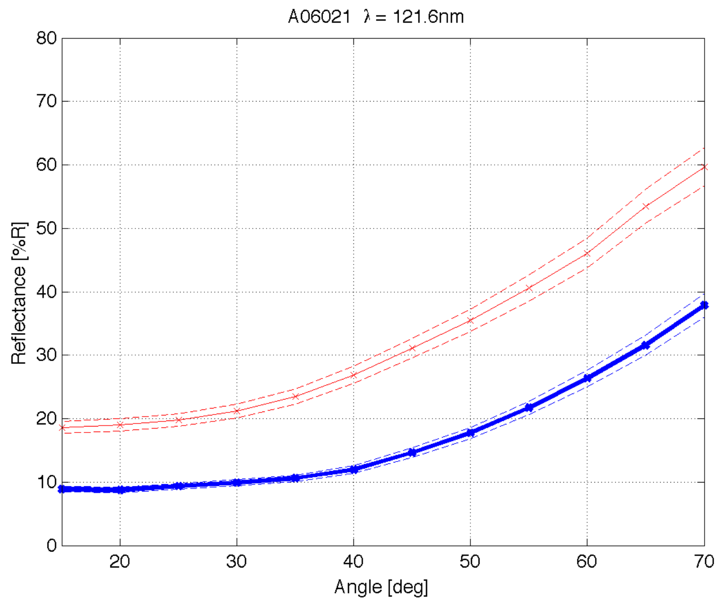

Figure 78: Sample A06021

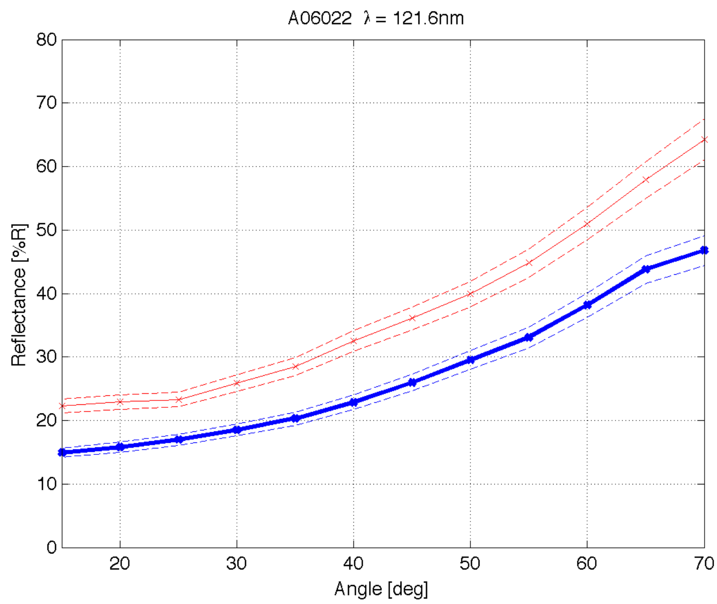

Figure 79: Sample A06022

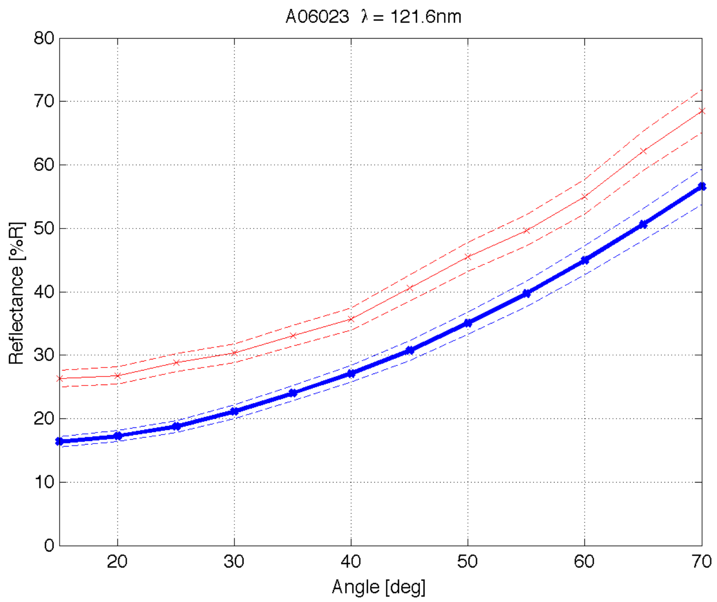

Figure 80: Sample A06023

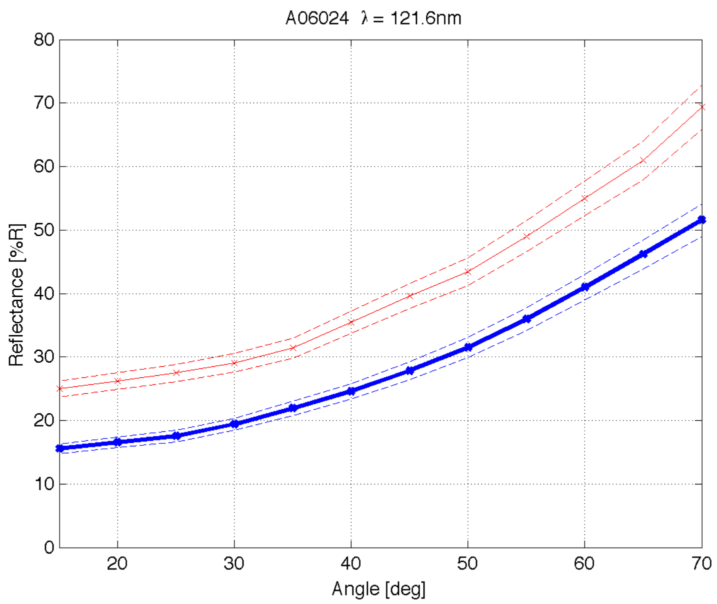

Figure 81: Sample A06024

SAMPLES FOR METIS/FEL The main UV measurements of this work were performed on new samples designed for Metis application. The only data obtained with chamber up-down position by now is about sample ML0. This can be considered absent from polarization issues, whereas the other data, acquired with up-position only, will be refined with further measurements.

The reflectivity performance is generally less than the one predicted with simulations, and after polarization correction are expected to be even lower. Probably this is caused by the formation of metal oxide even after such a short time after deposition, especially for Aluminium and Tungsten. More measurements are necessary to investigate this issue, and optical constants of oxidized metals must be collected to estimate the progress of oxidation.

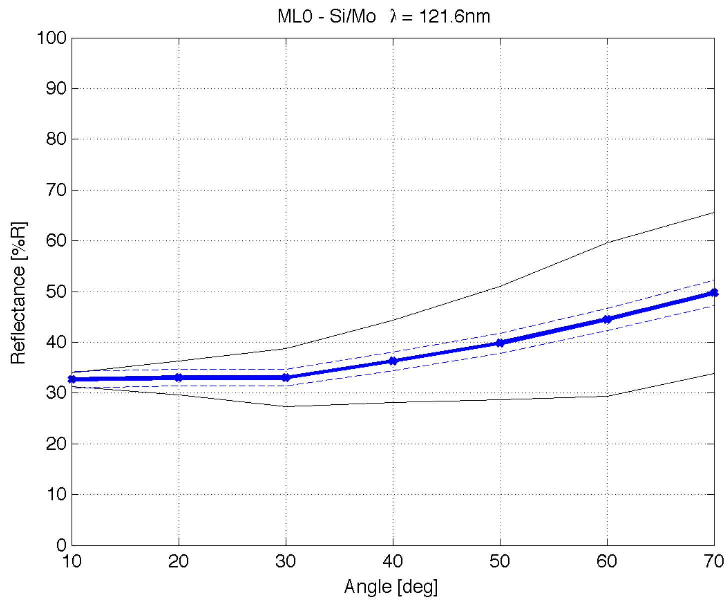

Figure 82: Sample ML0 - Si/Mo (corrected with up/down measurement technique). Polarized light measurements are represented with black lines: camera up (higher values) and camera down (lower values).

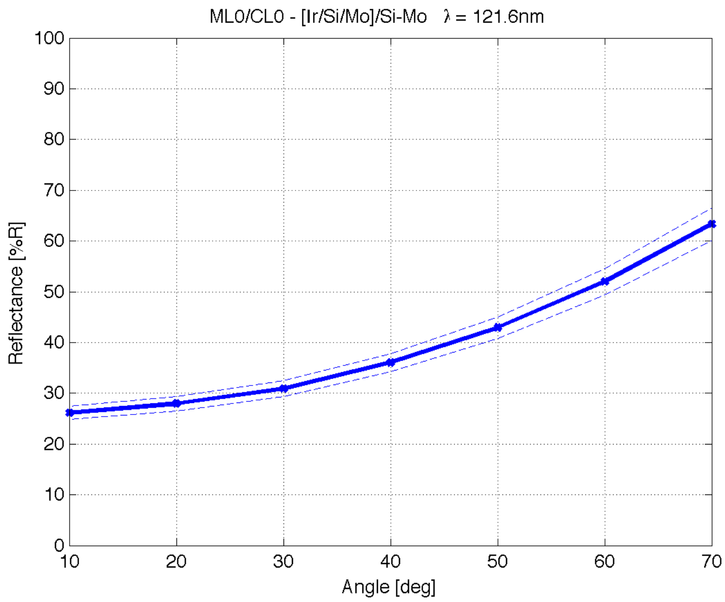

Figure 83: Sample ML0/CL0 - [Ir/Si/Mo]/Si-Mo.

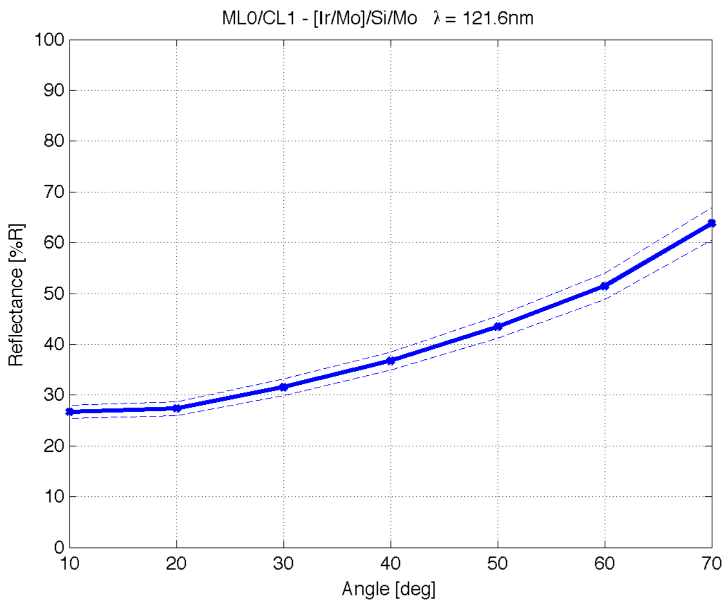

Figure 84: Sample ML0/CL1 - [Ir/Mo]/Si/Mo.

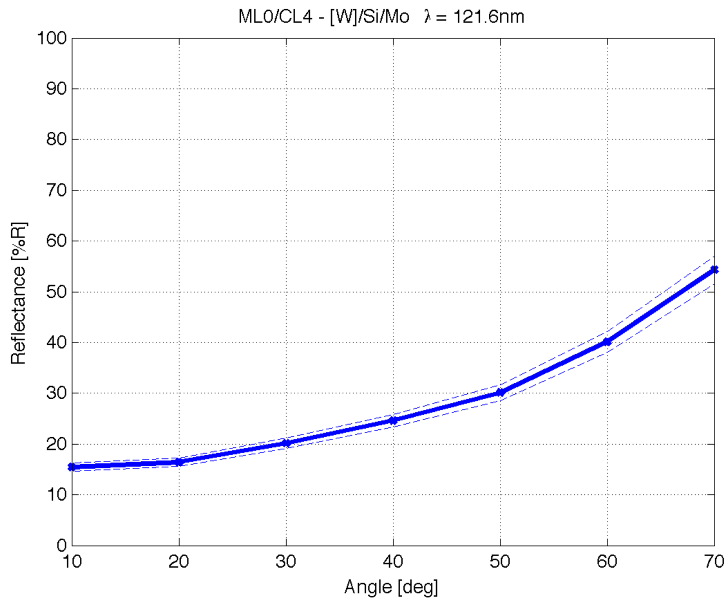

Figure 85: Sample ML0/CL4 - [W]/Si/Mo.

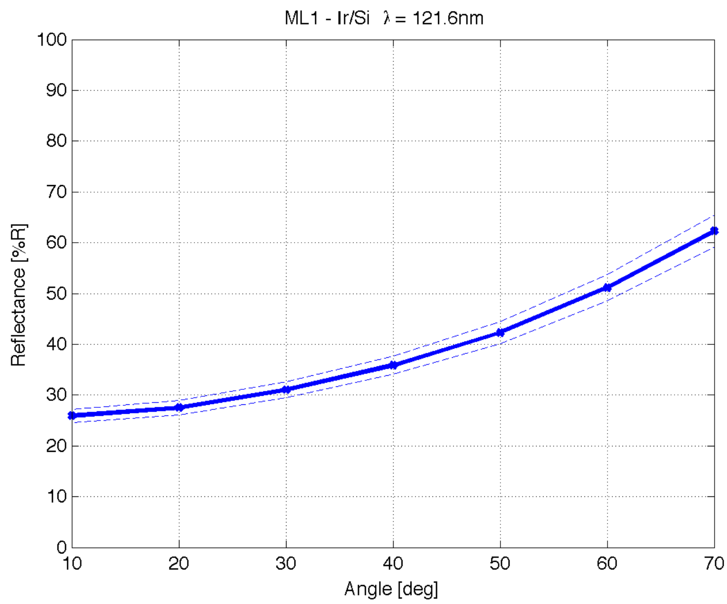

Figure 86: Sample ML1 - Ir/Si.

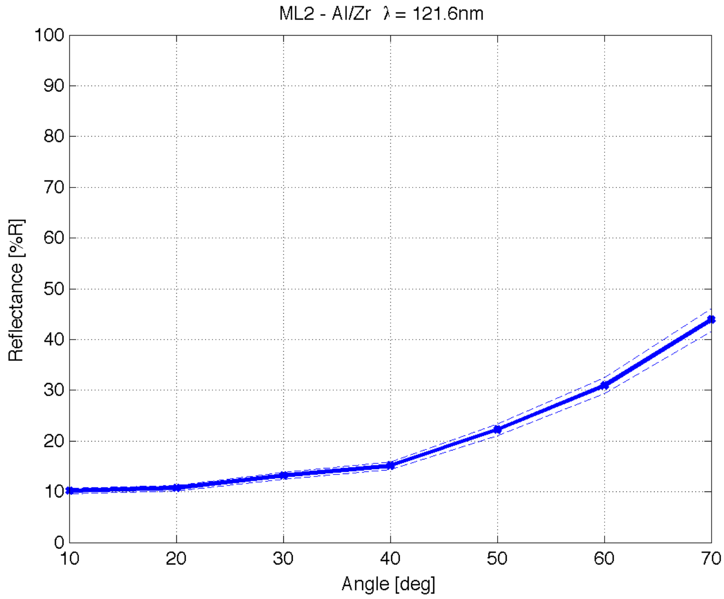

Figure 87: Sample ML2 - Al/Zr.

aaa

6.3 UV MEASUREMENTS @ 58.4NM

SAMPLE FOR FEL Only the ML0 sample has been tested by now on the 58.4nm line.

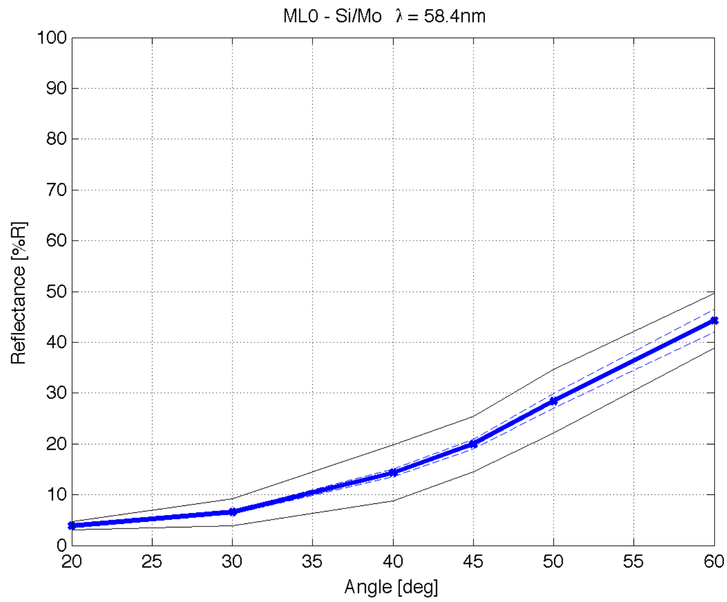

Figure 88: Sample ML0 - Si/Mo (corrected with up/down measurement technique). Polarized light measurements are represented with black lines: camera up (higher values) and camera down (lower values).

Attenuation not high enough for filtering

Here, reflectivity is around 5% at low incidence angles, rising to 20% at 45°. This angle is the one that will probably be used to implement a delay line, so its reflectance value is the most relevant. Unfortunately, 20% is quite high for the application. In fact, even referring to a line transmitting the full (100%) first harmonic, a relative attenuation factor of 1000 could be reached with at least $\lceil \log_5 1000 \rceil = 5$ cascaded elements.

6.4 INTERFEROMETRIC ANALYSIS

The output data shows a PV offset difference of 6.7µm, unacceptable for the FEL application. Anyway, these samples were not deposited with a so strict flatness requirement in mind, so the flatness may surely be improved. Having tested the feasibility of this type of measurement is a result itself, and will be applied to upcoming samples.

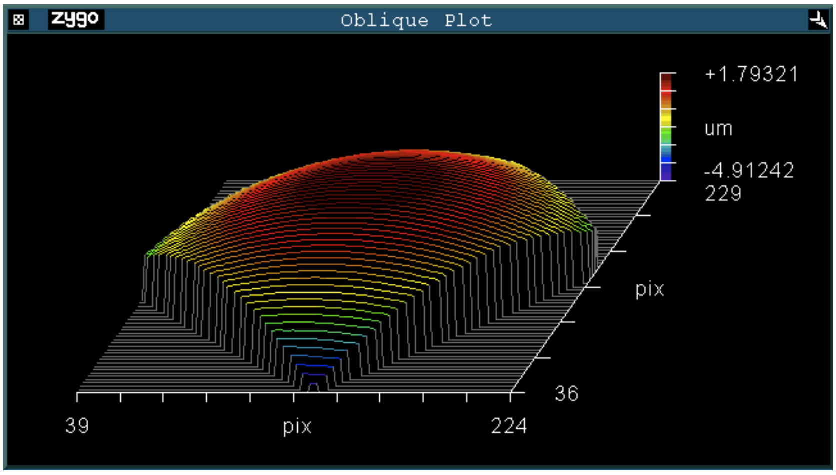

Figure 89: Interferometric 3D profile graph.

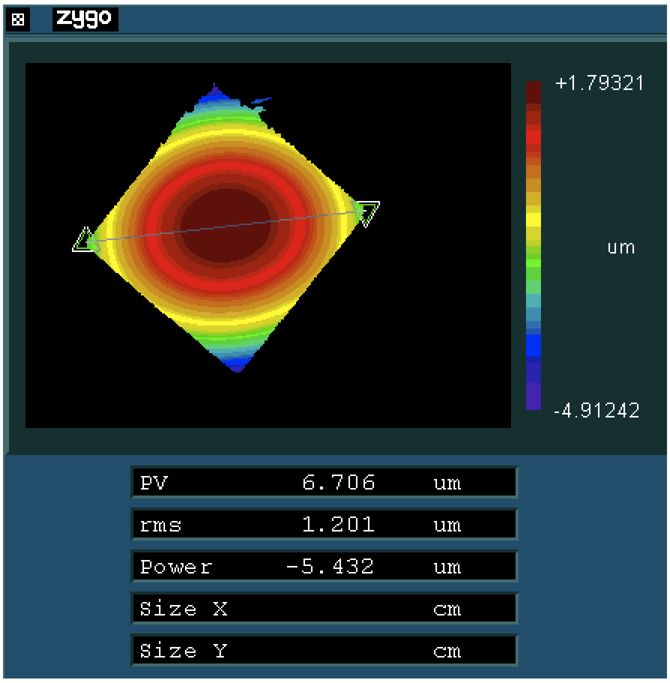

Figure 90: Interferometric offset graph.

6.5 AFM MEASUREMENTS AT LUXOR

Measured roughness

The AFM analysis gives as main information the roughness of the coating surface. The RMS value obtained is $\sigma_r = 2.8\text{Å}$. This value is useful to evaluate the boundary quality and adapt the simulations accounting the best achievable roughness.

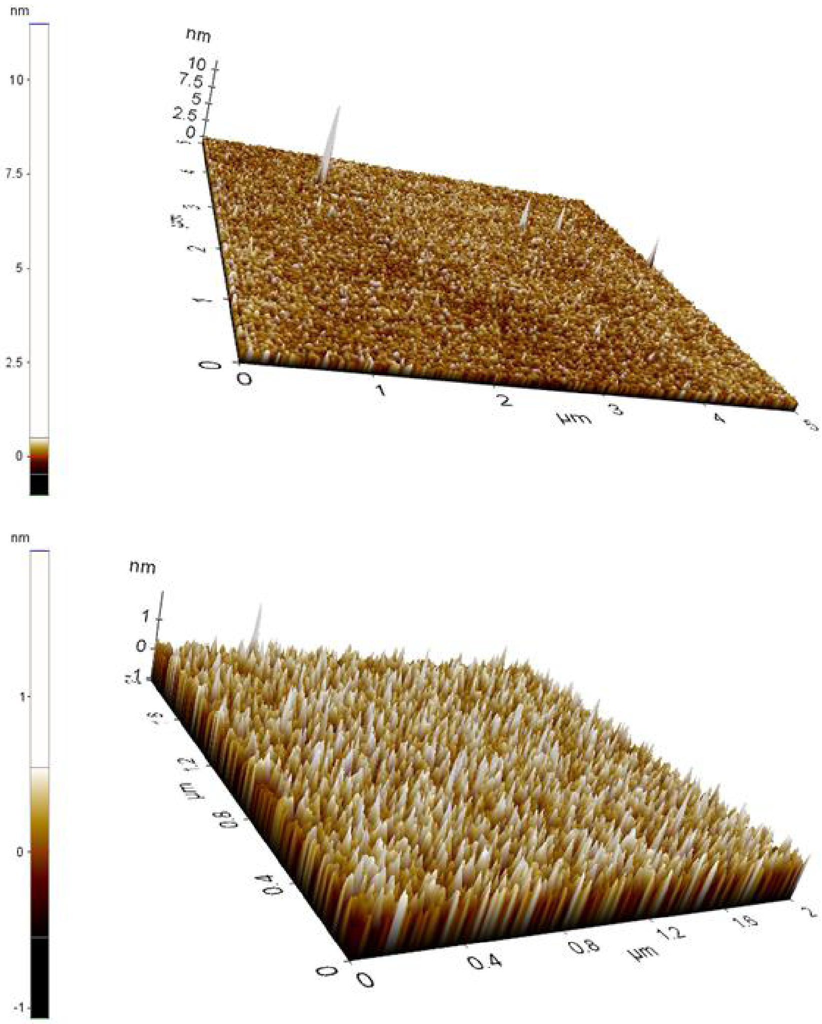

Figure 91: AFM measurements represented in two different scale values.

6.6 EUV MEASUREMENTS @ 30.4NM, ELETTRA

SAMPLES FOR METIS/FEL These measurements have been taken by LUXOR team at BEAR beamline at ELETTRA Synchrotron facility. The samples were tested with $\theta = 5°$ incidence angle and a wavelength scan from 24.6 to 34.3nm.

Many inconsistencies from simulations have been found. From those, implementation differences like period error or better roughness have been hypothesized. Among the samples, the best reflectance values were achieved by Iridium MLs and Iridium-based CLs.

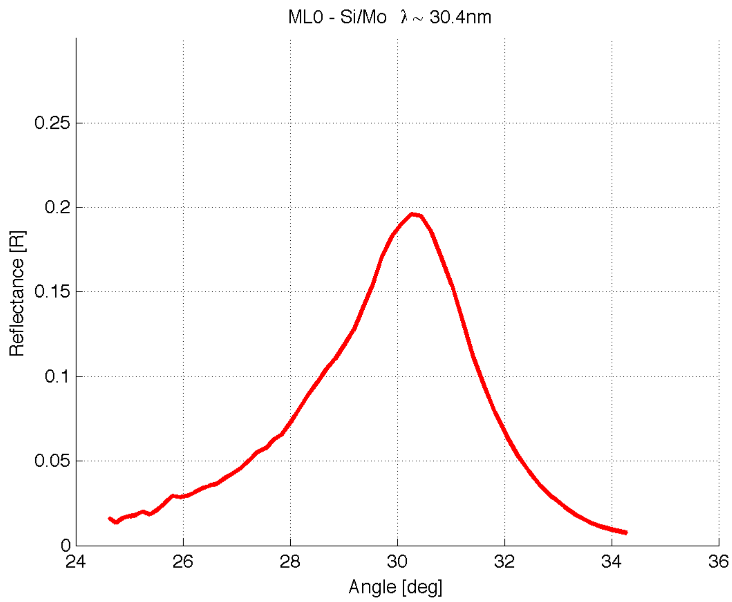

Figure 92: Sample MLo - Si/Mo.

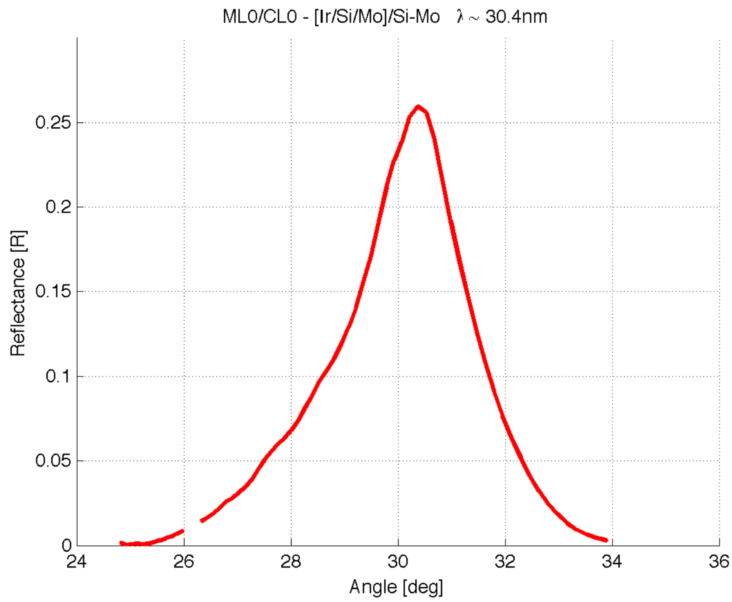

Figure 93: Sample ML0/CL0 - [Ir/Si/Mo]/Si-Mo.

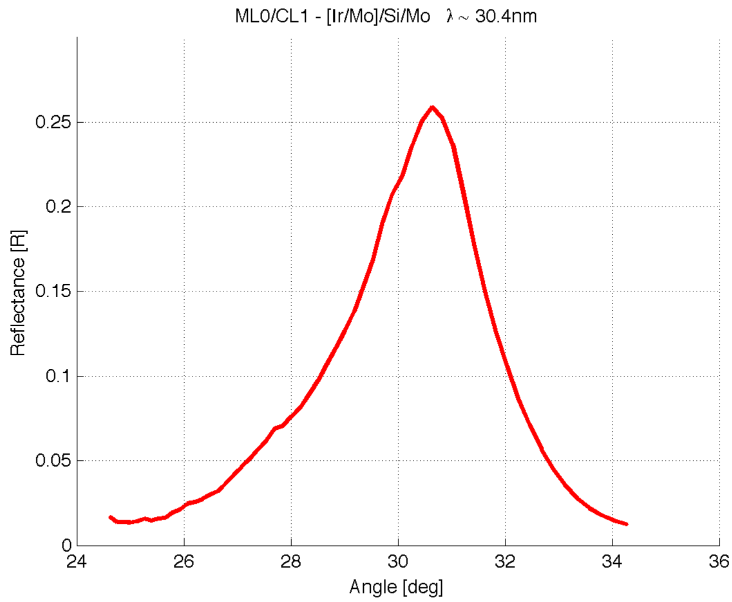

Figure 94: Sample ML0/CL1 - [Ir/Mo]/Si/Mo.

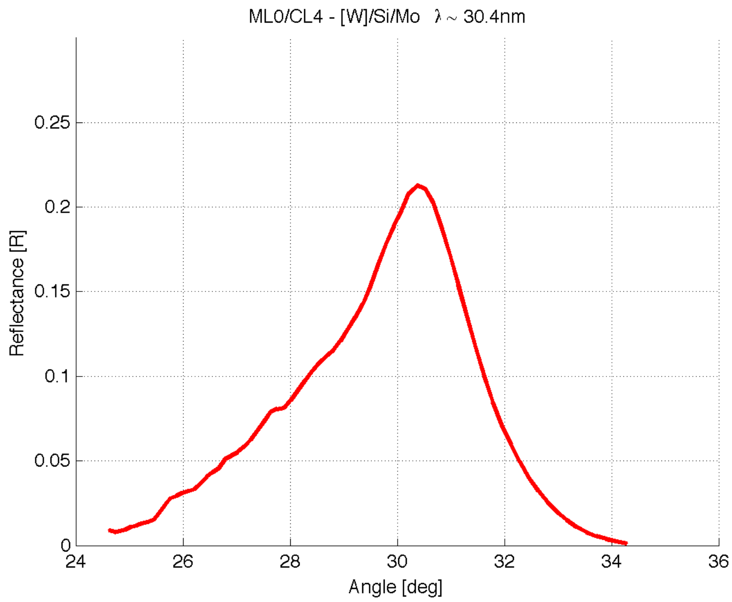

Figure 95: Sample ML0/CL4 - [W]/Si/Mo.

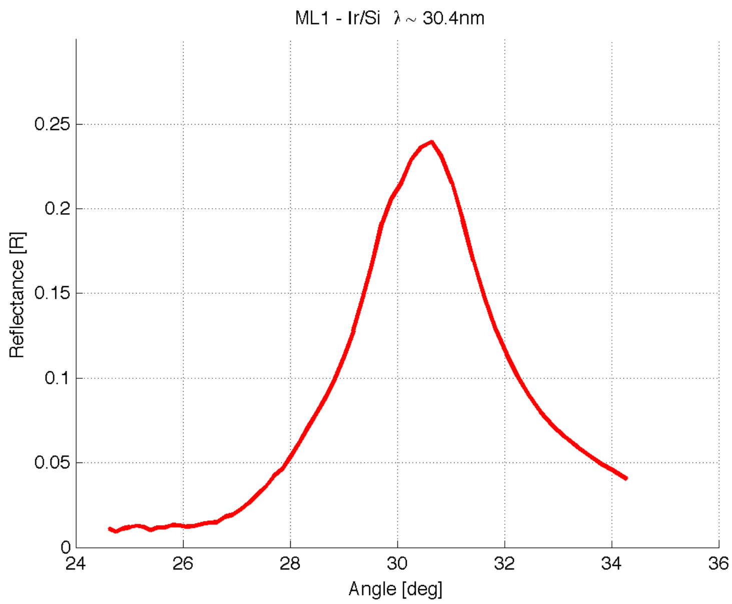

Figure 96: Sample ML1 - Ir/Si.

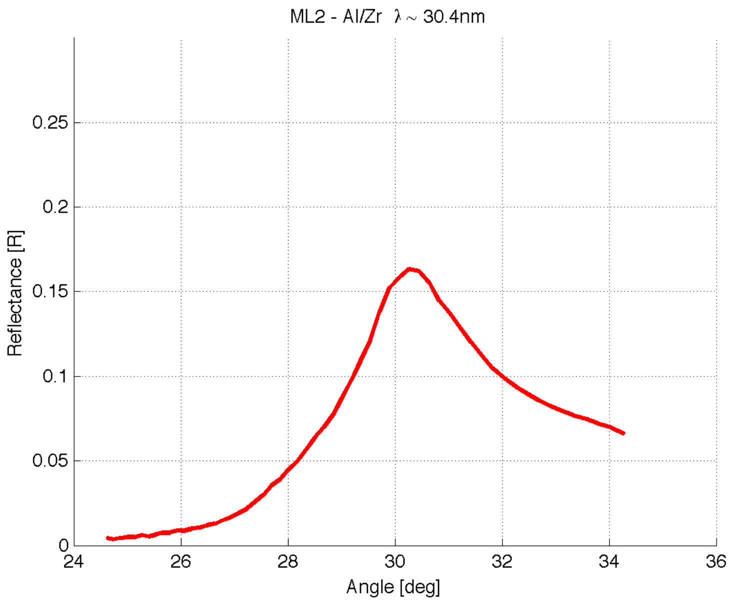

Figure 97: Sample ML2 - Al/Zr.

SAMPLES FOR SCORE The measurement data of these samples is compared with a single-line reflectance values taken on july 2006 contextually with the 121.6nm measurements, but using the SXR grazing incidence facility at LUXOR laboratories with $\theta = 6°$ incidence angle.

Slight angle difference

The comparison indicates a general loss of performance around 10%, and the low difference of 1° between incidence angles should not affect the comparability of data.

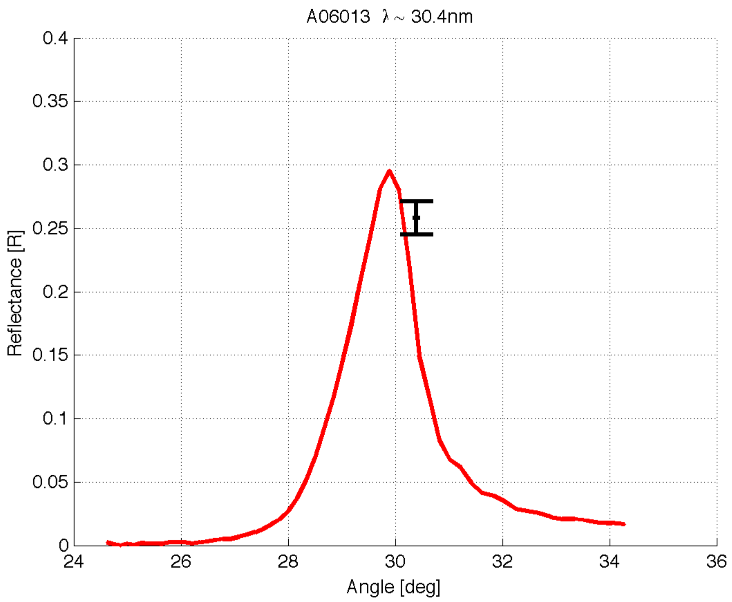

Figure 98: Sample A06013.

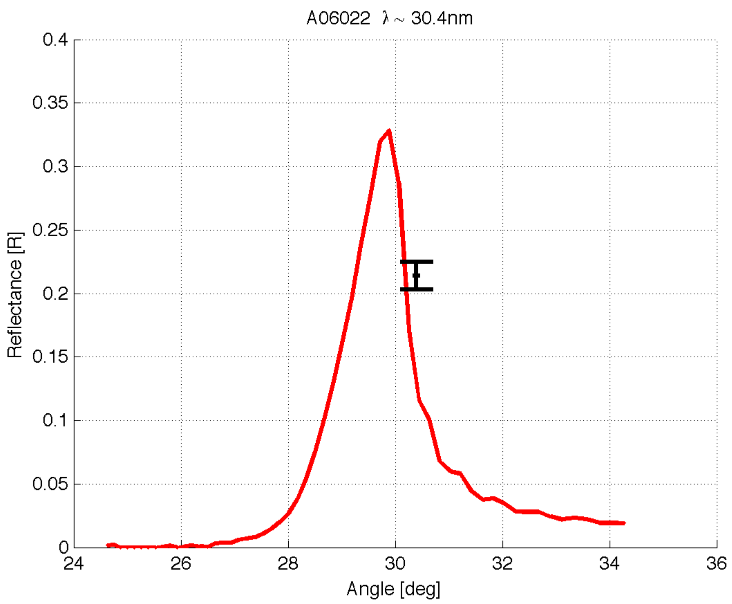

Figure 99: Sample A06022

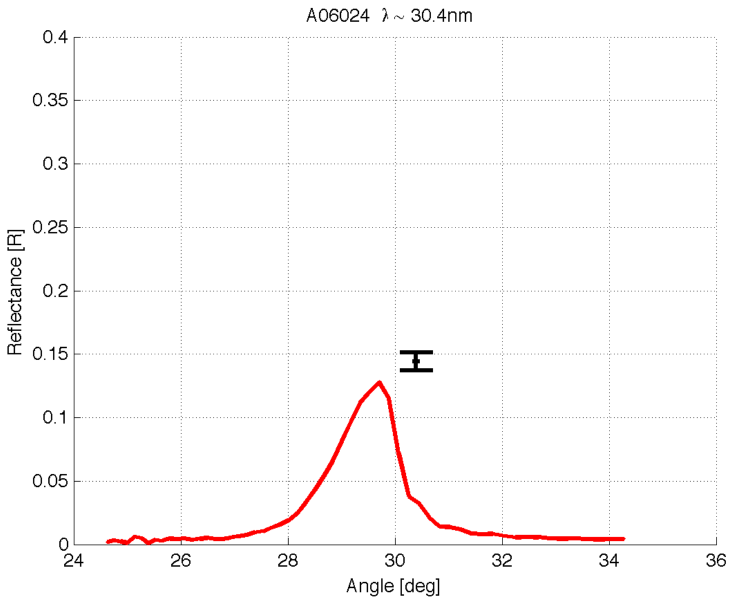

Figure 100: Sample A06024

7 COMMENTS AND REMARKS

METIS Although the measurement campaign can not be considered finished, the work allowed to understand many aspects of the behaviour of such multilayer optical devices in those not widely known spectral regions that are far- and extreme-UV.
The behaviour of almost every sample in the VIS range can be quite satisfactory (with Aluminium above all); actually that result was expected because thanks to low penetration, the multilayer structure itself can not influence the already good VIS performance of metals. Moreover, the aging issue is no more a concern in this region as it affected only a few part of the old samples.

Good VIS performance

More annoying was the effect of aging on performance at 121.6nm and 30.4nm, where a mean loss of 10% on old data has been determined. Apart from that, the most promising technology on new samples is the Iridium capping-layer. According to simulations, it behaved with optimum performance at 30.4nm, keeping good reflectance also in the 121.6nm UV line. The good reflectance of Iridium brought optimum contribute to the innovative Iridium/Silicon couple for capping layers, showing the best performance among all the samples tested, above 25% over all the span of interest.

Strong aging effects on Mg/SiC

Good UV/EUV performance of Iridium

On the converse, many samples had unexpected behaviour, like Tungsten and Aluminium/Zirconium capping layers that showed only moderate or even low reflectance values disaccording with the simulations that lead to their design. That one more time suggests a deeper investigation of optical constants.

The expectation for the best performing samples is above all a low aging effect, to preserve their good reflectivity during the deal with the harsh conditions of the mission. The measurement data obtained will in fact be the baseline for the successive tests upon those samples, that will include solar wind particles impact, radiation and thermal effects [CSM+10]; that will determine what technology is going produce the film that will give the sight to the bravest investigation of the heliospheric mechanisms.

Next performance tests

FEL The early measurement performed for this application showed that a device reflecting less that 20% at 60.8nm is available, although its suppressive power is not enough by now. But its reflectivity can surely be lowered, being the sample not actually designed for that aim only.
The interferometric analysis showed that particular attention must be paid in order to produce a flat coating, as the flatness resulting naturally from the process used is absolutely not satisfactory.

Not enough suppression by now

Useful metrology considerations for future campaigns

METROLOGY The metrology analysis of the measurement process play an important part of the results, together with the bare obtained data. In fact the accuracy of the measurement process was proved to be discriminant for evaluating the performance, and even if obtained results are not satisfactory in every direction, the process described has been shown useful to develop the present and possibly future multilayer technologies.

BIBLIOGRAPHY

[Abd06] Abdullahi, Musa D.: *BORH'S DERIVATION OF BALMER-RYDBERG FORMULA THROUGH QUANTUM MECHANICS*, 2006. http://www.musada.net/Papers/Appendix2.pdf.

[Abt06] Abteilung Extraterrestrische Physik: *The Solar Orbiter mission*, 2006. http://www.ieap.uni-kiel.de/et/en/missionen/solorb.php. (Cited on pages x and 5.)

[ACC+10] Allaria, E., C. Callegari, D. Cocco, W. M. Fawley, M. Kiskinova, C. Masciovecchio, and F. Parmigiani: *The fermi@elettra free-electron-laser source for coherent x-ray physics: photon properties, beam transport system and applications*. New J. Physics, 2010. (Cited on page 18.)

[Age10] Agenzia Spaziale Italiana: *SCORE sotto il Sole*, 2010. http://www.asi.it/it/news/score_sotto_il_sole_0. (Cited on page 34.)

[Amp02] Amptek, Inc.: *Amptektron MD-501 Electron and Ion Detector*, 2002. http://www.amptek.com/md501.html. (Cited on pages xi, 56, 59, and 60.)

[Att99] Attwood, David T.: *Soft x-rays and extreme ultraviolet radiation: principles and applications*. Cambridge University Press, 1999, ISBN 0-521-65214-6. (Cited on page 14.)

[AVT10] AVT Services Pty. Australia: *How it works – The AIM Gauge*, 2010. http://www.avtservices.com.au/avt/aim-gauge-how-it-works. (Cited on page 54.)

[BBC+10] Bocchetta, C., D. Bulfone, P. Craievich, M. B. Danailov, G. D'Auria, G. DeNinno, S. Di Mitri, B. Diviacco, M. Ferianis, A. Gomezel, F. Iazzourene, E. Karantzoulis, F. Parmigiani, G. Penco, M. Trovo, J. Corlett, W. Fawley, S. Lidia, G. Penn, A. Ratti, J. Staples, R. Wilcox, A. Zholents, W. Graves, F. O. Ilday, F. Kaertner, T. Zwart D. Wang, M. Cornacchia, P. Emma, Z. Huang, and J. Wu: *Fermi @ elettra – a seeded harmonic cascade fel for euv and soft x-rays*. SLAC-PUB-11488, 2010. (Cited on pages x, 15, and 16.)

[BJ03] Brandsen, B. H. and C. J. Joachain: *Physics of Atoms and Molecules, 2nd edition*. Pearson education, 2003, ISBN 978-0-582-35692-4. (Cited on page 3.)

[CAB+09] Cocco, D., A. Abrami, A. Bianco, I. Cudin, C. Fava, D. Giuressi, R. Godnig, F. Parmigiani, L. Rumiz, R. Sergo, C. Svetina, and M. Zangrando: *The fermi@elettra fel photon transport sytem*. In *Proc. of SPIE Vol. 7361*, 2009. (Cited on pages x, 16, 17, and 19.)

[Cen88] The Center for Occupational Research and Development: *GRATINGS*, 1988. http://cord.org/cm/leot/course06_mod09/mod06_09.htm. (Cited on pages xi, 40, 41, and 42.)

[Cor10] Corso, Alain J.: *Nanostructured optical coatings for solar physics observations from space*. Master's thesis, University of Padova, 2010. (Cited on page 32.)

[CSM+10] Corso, A.J., M. Suman, G. Monaco, P. Zuppella, P. Nicolosi, and M.G.Pelizzo: *Multilayer coatings for metis instrument*. In *ICSO 2010 - International Conference on Space Optics*, Rhodes, 4-8 October 2010. (Cited on pages 32 and 105.)

[Deu10] Deutsches Elektronen-Synchrotron DESY: *Pump-and-Probe Experiments*. Hamburger Synchrotronstrahlungslabor HASYLAB, 2010. http://hasylab.desy.de/facilities/flash/facility_information/pump_and_probe/index_eng.html. (Cited on page 18.)

[DR01] Dattoli, Giuseppe and Alberto Renieri: *FREE ELECTRON LASERS*. ENEA - Frascati, 2001. http://cas.web.cern.ch/cas/Pruhonice/PDF/Renieri.pdf. (Cited on page 14.)

[FAG+01] Fineschi, S., E. Antonucci, D. Garoli, V. de Deppo, G. Naletto, M. Romoli, A. Cacciani, and M. Malvezzi: *Extended uv corona imaging from the solar orbiter: tha metis ultraviolet and visible-light coronagraph (uvc)*. In *Solar Encounter: The First Solar Orbiter Workshop*, 2001. (Cited on pages 3 and 4.)

[FMS+03] Feldhaus, J., T. Möller, E. L. Saldin, E. A. Schneidmillera, and M. V. Yurkovb: *Pump–probe experiments in the femtosecond regime, combining first and third harmonics of sase fel radiation*. Nuclear Instruments and Methods in Physics Research, 2003. (Cited on pages x, 18, and 19.)

[Gio02] Giovenale, Emilio: *FREE ELECTRON LASER: OPERATING PRINCIPLES*. ENEA - Frascati, 2002. http://www.frascati.enea.it/fis/docs/fel.pdf. (Cited on pages 11 and 13.)

[Gul10] Gullikson, Eric: *X-Ray Interactions With Matter*. CXRO: the center for x-ray optics, 2010. http://henke.lbl.gov/optical_constants. (Cited on pages x, 23, 24, and 31.)

[Ham05] Hamamatsu Photonics K.K.: *L2D2 Deuterium Lamps*, 2005. http://sales.hamamatsu.com/assets/pdf/catsandguides/Lmps_L2D2.pdf. (Cited on page 56.)

[Ham06] Hamamatsu Photonics K.K.: *Photomultiplier Tubes R928, R955*, 2006. http://sales.hamamatsu.com/assets/pdf/parts_R/R928_R955_TPMS1001E07.pdf. (Cited on page 47.)

[HZ03] Hecht, E. and A. Zajac: *Optics*. Addison Wesley, 2003, ISBN 978-0805385663. (Cited on pages xi, 39, and 40.)

[Lab08] Labsphere, Inc.: *Spectralon® Diffuse Reflectance Standards*, 2008. http://www.labsphere.com/data/userFiles/Diffuse%20Reflectance%20Standards%20Product%20Sheet_8.pdf. (Cited on page 69.)

[LOT10] LOT Oriel Italia s.r.l.: *GPI XP/D Specifications*, 2010. http://www.lot-oriel.com/site/site_down/zy_gpixp_iten01.pdf. (Cited on pages xiii, 65, and 67.)

[Mil08] Milton, Stephen V.: *The FERMI@Elettra project*. John Adams Institute for Accelerator Science, 2008. http://www.adams-institute.ac.uk/resources/lectures/2008_06_12_JAI-MILTON.pdf. (Cited on page 15.)

[Mon09] Monaco, Gianni: *High reflective optics for different spectral region*. PhD thesis, University of Padova, 2009. (Cited on pages xi, 51, 52, 56, and 57.)

[NAA+10] Naletto, G., E. Antonucci, V. Andretta, E. Battistelli, S. Cesare, V. Da Deppo, F. dAngelo, S. Fineschi, M. Focardi, P. Lamy, F. Landini, D. Moses, G. Nicolini, P. Nicolosi, M. Pancrazzi, M G. Pelizzo, L. Poletto, M. Romoli, S. Solanki, D. Spadaro, L. Teriaca, M. Uslenghi, and L. Zangrilli: *Metis, the multielement telescope for imaging and spectroscopy for the solar orbiter mission*. In *ICSO 2010 - International Conference on Space Optics*, Rhodes, 4-8 October 2010. (Cited on page 6.)

[Pal05] Palmer, Christopher: *DIFFRACTION GRATING HANDBOOK*. NEWPORT CORPORATION, 2005. (Cited on pages 51 and 52.)

[Pol10] Polyanskiy, Mikhail: *Refractive index database*, 2010. http://refractiveindex.info. (Cited on page 31.)

[PVD10] PVD coatings: *The theory of PVD coatings: magnetron sputtering*, 2010. http://www.pvd-coatings.co.uk/theory-of-pvd-coatings-magnetron-sputtering.htm. (Cited on pages xi, 34, and 36.)

[Ren07] Renton, D.: *Solar orbiter payload definition document*. Technical report, European Space Agency, 2007. http://sci.esa.int/science-e/www/object/doc.cfm?fobjectid=41440. (Cited on page 5.)

[Sin01] Sincrotrone Trieste: *European FEL project at ELETTRA*, 2001. http://www.elettra.trieste.it/projects/euprog/fel. (Cited on page 15.)

[Sin06] Sincrotrone Trieste: *FEL in Italy: FERMI@Elettra*, 2006. http://www.presid.infn.it/er/er06bocchetta.pdf.

[Spi94] Spiller, Eberhard: *Soft X-Ray Optics*. SPIE press, 1994, ISBN 0-8194-1655-X. (Cited on pages 27, 29, and 30.)

[ST07] Saleh, B.E.A and M.C. Teich: *Fundamentals of Photonics*. Wiley, 2007, ISBN 978-0-471-35832-9. (Cited on page 39.)

[Sum09] Suman, Michele: *STUDY OF THE ELECTROMAGNETIC RADIATION INTERACTIONS WITH NANOMETRIC STRUCTURES FOR OPTICS DEVELOPMENT*. PhD thesis, University of Padova, 2009. (Cited on pages x, 25, 32, and 35.)

[Tec10] Technische Universitat Darmstadt: *Principle of Free Electron Lasers*. INSTITUTE OF NUCLEAR PHYSICS, 2010. http://www.ikp.physik.tu-darmstadt.de/richter/fel/overview.html. (Cited on pages x and 13.)

[Uni10] Univesità degli Studi della Tuscia: *Pump-probe Spectroscopy*, 2010. http://www.unitus.it/biophysics/RicercaEn_file/Spectroscopy_file/Pump-probe.htm. (Cited on page 18.)

[Var02] Varian, Inc.: *UV-VIS-NIR Cary 4000, 5000, 6000i Spectrophotometers: Preliminary Performance Data*, 2002. http://www.science.unitn.it/~semicon/members/pavesi/Technical-1942.pdf. (Cited on pages xiii, 50, and 72.)

[Var04] Varian, Inc.: *Cary 4000, 5000 and 6000i Spectrophotometers*, 2004. http://www.varianinc.com/image/vimage/docs/products/spectr/uv/brochure/1942.pdf. (Cited on pages xi, 44, 45, and 46.)

[Var10] Varian, Inc.: *Diffuse Reflectance Accessory (Internal)*, 2010. (Cited on pages xi, 48, 49, and 70.)

[WBHH81] Winick, Herman, George Brown, Klaus Halbach, and John Harris: *Wiggler and undulator magnets*. Physics Today, Volume 34, Issue 5, 1981. (Cited on pages x and 14.)

[Win98] Windt, David L.: *Imd - software for modeling the optical properties of multilayer films*. Computers in Physics, vol. 12, no. 4, 1998. (Cited on pages x, 27, 29, and 30.)

[WJS+88] Windt, David L., Webster C. Cash Jr., M. Scott, P. Arendt, Brian Newman, R.F. Fisher, A. B. Swartzlander, P.Z. Takacs, and J. M. Pinneo: *Optical constants for thin films of c, diamond, al, si and cvd sic from 24 å to 1216 å*. Applied Optics, vol. 27, no. 2, 1988.

[Wya00] Wyant, James C.: *Phase Shifting Interferometry*. University of Arizona - College of Optical Sciences, 2000. http://www.optics.arizona.edu/jcwyant/Optics505(2000)/ChapterNotes/Chapter09/phaseshiftinginterferometry.pdf. (Cited on pages 62 and 64.)

[Wya09] Wyant, James C.: *Testing Flat Surface Optical Components*. University of Arizona - College of Optical Sciences, 2009. http://www.optics.arizona.edu/jcwyant/Short_Courses/SIRA/5-TestingFlatSurfaceOpticalComponents.pdf. (Cited on pages xi and 63.)

[YZ08] Yang, Q. and L.R. Zhao: *Characterization of nano-layered multilayer coatings using modified bragg law*. MATERIALS CHARACTERIZATION 59, 2008. (Cited on pages x, 30, and 31.)

[ZGP+06] Zuccon, S., D. Garoli, M.G. Pelizzo, P. Nicolosi, S. Fineschi, and D. Windt: *Multilayer coatings for multiband spectral observations*. In *6th Internat. Conf. on Space Optics*, ESTEC, Noordwijk, The Netherlands, 2006. ESA SP-621. (Cited on pages 5 and 7.)

[ZYG10] ZYGO CORPORATION: *GPI and VeriFire Accessory Guide*, 2010. http://www.zygo.com/met/interferometers/verifire/verifire_accys.pdf. (Cited on pages xi, 65, and 66.)